

NANOSCIENCE FOR SUSTAINABLE ENERGY PRODUCTION

A DISSERTATION SUBMITTED TO
THE DEPARTMENT OF PHYSICS
AND THE GRADUATE SCHOOL OF ENGINEERING AND SCIENCE
OF BILKENT UNIVERSITY
IN PARTIAL FULFILLMENT OF THE REQUIREMENTS
FOR THE DEGREE OF
DOCTOR OF PHILOSOPHY

By
CAN ATACA
December, 2011

I certify that I have read this thesis and that in my opinion it is fully adequate, in scope and in quality, as a dissertation for the degree of doctor of philosophy.

Prof. Dr. Salim ıracı(Advisor)

I certify that I have read this thesis and that in my opinion it is fully adequate, in scope and in quality, as a dissertation for the degree of doctor of philosophy.

Prof. Dr. Ergin Atalar

I certify that I have read this thesis and that in my opinion it is fully adequate, in scope and in quality, as a dissertation for the degree of doctor of philosophy.

Prof. Dr. Taner Yıldırım

I certify that I have read this thesis and that in my opinion it is fully adequate, in scope and in quality, as a dissertation for the degree of doctor of philosophy.

Prof. Dr. Şakir Erkoç

I certify that I have read this thesis and that in my opinion it is fully adequate, in scope and in quality, as a dissertation for the degree of doctor of philosophy.

Assoc. Prof. M. Özgür Oktel

Approved for the Graduate School of Engineering and
Science:

Prof. Dr. Levent Onural
Director of the Graduate School

ABSTRACT

NANOSCIENCE FOR SUSTAINABLE ENERGY PRODUCTION

CAN ATACA

Ph.D.in Physics

Supervisor: Prof. Dr. Salim Çıracı

December, 2011

Hydrogen economy towards the utilization of hydrogen as a clean and sustainable energy source has three ingredients. These are (i) hydrogen production; (ii) hydrogen storage; and (iii) fuel cells. Optimization of fuel cells for desired applications is a challenging engineering problem. The subject matter of my thesis is to develop nanostructures and to reveal physical and chemical mechanisms for the production of free hydrogen and its high capacity storage. The predictions of this study are obtained from first-principles density functional theory and finite temperature molecular dynamics calculations, phonon calculations and transition state analyses.

Recent studies have revealed that single layer transition metal oxides and dichalcogenides (MX_2 ; M:Transition metal, X:Chalcogen atom) may offer properties, which can be superior to those of graphene. Synthesis of single layer free standing MoS_2 and its nanoribbons, fabrication of transistor using this nanostructure, active edges of flakes of MoS_2 taking a part in hydrogen evolution reaction (HER) boost the interest in these materials. The electronic, magnetic, mechanical, elastic and vibrational properties of three-, two- and quasi one-dimensional MoS_2 are investigated. Dimensionality effects such as indirect to direct band gap transition, shift of phonon modes upon three- to two- dimensional transition, half metallic nanoribbons are revealed. Functionalization of single layer MoS_2 and its nanoribbons are achieved by creating vacancy defects and adatom adsorption. Moreover, out of 88 different combinations of MX_2 compounds (transition metal dichalcogenides) it is also predicted that more than 50 single layer, free standing MX_2 can be stable in honeycomb like structures and offer novel physical and chemical properties relevant for hydrogen economy.

It is predicted that H_2O can be split spontaneously into its constituents O and

H at specific vacancy defects of single layer MoS₂ honeycomb structure. Interacting with the photons of visible light, H atoms adsorbed to two folded S atoms surrounding the vacancy start to migrate and eventually form free H₂ molecules, which in turn, are released from the surface. Not only taking a part in HER, but also it is shown that MoS₂ as a catalyst can release H₂ molecule from water. Also other possible candidates among the manifold of stable MX₂ compounds, which are capable of presenting similar catalytic activities are deduced.

In an effort to obtain a high capacity hydrogen storage medium, the functionalization of graphene with adatoms is investigated. It is found that Li-graphene complex can serve as a high capacity hydrogen storage medium. A gravimetric storage capacity of 12.8 wt % is attained, whereby each Li atom donates the significant part of its charge to graphene and eventually attracts up to four H₂ through a weak interaction. Similarly Ca adatoms can hold H₂ molecule on graphene up to 8.4 wt % through an interesting mechanism involving charge exchange among Ca, graphene and H₂.

Present results are critical for acquiring clean and sustainable energy from hydrogen.

Keywords: MoS₂, MX₂, H₂ production, Water Splitting, H₂ storage, Graphene.

ÖZET

SÜRDÜRÜLEBİLİR ENERJİ ÜRETİMİ İÇİN
NANOBİLİM

CAN ATACA

Fizik, Doktora

Tez Yöneticisi: Prof. Dr. Salim Çıracı

Aralık, 2011

Hidrojenin temiz ve sürdürülebilir bir enerji kaynağı olarak kullanılmasına olanak sağlayan hidrojen ekonomisi üç içeriğe sahiptir. Bunlar: (i) hidrojen üretimi; (ii) hidrojen depolama; ve (iii) yakıt hücreleridir. Yakıt hücrelerinin arzu edilen uygulamalara göre optimize edilmesi mühendislik açısından efor gerektiren bir problemdir. Tezimin konusu serbest hidrojen üretimini ve hidrojeni yüksek kapasitede depolanmasını mümkün kılacak nano yapılar tasarlamak ve bunların fiziksel ve kimyasal mekanizmalarını açıklamaktır. Bu çalışmadaki öngörüler temel prensipler yoğunluk fonksiyoneli kuramı, sonlu sıcaklıkta moleküler dinamik hesapları, fonon hesapları ve geçiş durumu analizleri çerçevesinde elde edilmiştir.

Yakın zamanlarda tek-tabakalı metal oksitler ve dikalkojen malzemeler (MX_2 ; M:Geçiş metali, X:Kalkojen atomu) üzerinde yapılan çalışmalar bunların grafene kıyasla daha üstün özelliklerinin olabileceğini ortaya koymuştur. Tek tabaka MoS_2 ve bunun nanoşeritlerinin sentezlenmesi, bu malzeme tabanlı nano transistörlerin üretimi ve hidrojen evrimi reaksiyonu sürecinde (HER) etkin olan aktif MoS_2 kenarların varlığı bu malzemeler üzerindeki ilgiyi arttırmaktadır. Burada üç, iki ve bir boyutlu MoS_2 'nin elektronik, manyetik, mekanik, elastik ve titreşimsel özellikleri araştırılmaktadır. Direkt-endirekt yasak band aralığı dönüşümü gibi boyut etkisi, iki boyuttan üç boyuta geçerken fonon modlarının kayması ve yarı-metalik nanoşeritler vurgulanmıştır. Tek tabakalı MoS_2 ve bunların nanoşeritlerinin fonksiyonelleştirilmesi atom boşlukları ve yabancı atomların eklenmesi ile başarılmıştır. 88 tane olası MX_2 bileşiğinin 50den fazlasının balpeteği biçimli tek tabakalı yapılarının var olabileceğini ve bunların yeni fiziksel ve kimyasal özelliklere sahip olacakları öngörülmüştür.

H_2O nun tek tabakalı MoS_2 ye ait atom boşlukları civarında kendini oluşturan

O ve H atomlarına kendiliğinden ayrışabileceği gösterilmiştir. Atom boşluklarının olduğu bölgeyi çevreleyen çift bağlı S atomları tarafından absorbe olmuş olan H atomları görünür ışığın fotonları ile etkileşerek buldukları konumdan ilerleyerek H₂ molekülleri oluşturup yüzeyden ayrılırlar. Sadece HER in bir parçası olarak değil ayrıca su moleküllerinden de H₂ üretimi için de MoS₂'nin bir katalizör olabileceği gösterilmiştir. Bunlara ek olarak benzer katalitik özellikleri gösterecek olası diğer MX₂ malzemeleri tartışılmaktadır.

Yüksek kapasitede hidrojen depolanması amacıyla grafinin yabancı atomlar ile fonksiyonelleştirilmesi de araştırılmıştır. Li-grafin kompleksinin yüksek kapasiteli hidrojen depolama amacı ile kullanılabileceği gösterilmiştir. Herbir Li atomun kendine ait yükün büyük bir kısmını grafine aktararak 4 tane H₂ molekülünü zayıf bir bağ ile kendine bağladığı ve gravimetrik olarak 12.8 % oranında depolama kapasitesine sahip olduğu gösterilmiştir. Benzer olarak grafin üzerinde yer alan Ca atomları, grafin ile ilginç bir yük alışverişi gerçekleştirerek, gravimetrik olarak 8.4 % oranında H₂ molekülünü depolayabilmektedirler.

Sunulan sonuçlar hidrojenden temiz ve sürdürülebilir enerji elde edilmesi açısından kritik öneme sahiptirler.

Anahtar sözcükler: MoS₂, MX₂, H₂ üretimi, Suyun Ayrışması, H₂ depolama, Grafin.

Acknowledgement

This thesis would not appear in its present form without the kind support of my supervisor Prof. Dr. Salim ıracı. I would like to thank him for his commitment to helping see this thesis through to its final copy and his equally generous and wise guidance during its development. I am also grateful to him for giving me a chance to complete my Ph. D. in three years. I am and will be proud of working in his group all through my life.

I would like to thank to Ethem Aktürk, Engin Durgun, Hasan Şahin, Ogun Özçelik, Mehmet Topsakal, and Seymur Cahangirov for their friendship and advises.

Finally, I want to express my gratitude to my family and Sıla Toksöz for their love, support, and understanding. I owe them a lot.

Contents

1	Introduction	1
2	Methodology - Density Functional Theory	6
2.1	Overview of Approximations	7
2.2	Electron-Electron Interaction	7
2.2.1	Method of Grimme: Introduction of van der Waals interaction	11
2.2.2	LDA+U: Correction in transition-metals	12
2.3	Periodic Supercells	13
2.4	Electron-Ion Interactions	14
2.5	Ion-Ion Interaction	16
2.6	Parameters of DFT Calculations	17
2.6.1	Pseudopotential Choice	17
2.6.2	Exchange Correlation Functional Choice	18
2.6.3	Convergence Criteria and Stability Analysis	18
3	Properties of MoS₂ Structure	23

3.1	Preliminary Information	23
3.2	Optimized Structures of MoS ₂	26
3.3	Stability of MoS ₂	28
3.4	Mechanical Properties of MoS ₂	36
3.5	Electronic and Magnetic Properties	38
3.5.1	2H-MoS ₂ and 1H-MoS ₂	38
3.5.2	Armchair and Zigzag Nanoribbons of MoS ₂	42
3.6	Functionalization of MoS ₂	44
3.6.1	Functionalization by Adatom Adsorption	46
3.6.2	Functionalization by Vacancy Defects	56
4	Beyond MoS₂: Stable, single layer MX₂ transition ...	61
4.1	Preliminary Information	61
4.2	Stability analysis	66
4.2.1	Structure optimization	66
4.2.2	Lattice Dynamics	67
4.2.3	Mechanical Properties	72
4.3	Electronic and magnetic properties	73
4.4	LDA+U calculations	77
4.5	MX ₂ as a hydrogen evolution reaction (HER) candidate	81
4.6	Discussions	84

5	Splitting of H₂O at the Vacancies of Single Layer MoS₂	86
5.1	Preliminary Information	86
5.2	Properties of vacancy defects on 1H-MoS ₂	89
5.3	Interaction of H ₂ O with perfect 1H-MoS ₂ surface	89
5.4	Interaction of H ₂ O at vacancy defects of 1H-MoS ₂	91
5.4.1	S-, Mo- vacancy and S ₂ - divacancy defects	91
5.4.2	MoS- di and MoS ₂ triple vacancy defects	92
5.4.3	Splitting of second H ₂ O in MoS ₂ triple-vacancy	94
5.5	Diffusion of H atoms on 1H-MoS ₂	97
5.5.1	Binding of H, O, and OH	97
5.5.2	Single H diffusion	100
5.5.3	Interaction of two hydrogen on 1H-MoS ₂ surface	102
5.5.4	Can Hydrogen Tunnel between neighboring hexagons of 1H-MoS ₂	104
5.6	H ₂ O splitting on MoS ₂ Nanoribbons and Other Transition Metal Dichalcogenides	106
5.7	Discussions	109
6	High Capacity H₂ Storage	113
6.1	Preliminary Information	113
6.2	High-capacity hydrogen storage by metallized graphene	114
6.3	Hydrogen storage of calcium atoms adsorbed on graphene	119

7 Conclusions

List of Figures

- 3.1 (a) Side and top views of atomic structure of 2H-MoS₂ with hexagonal lattice. The unit cell is delineated, lattice constants $|a| = |b|$, c and internal structure parameters are indicated. Honeycomb structure consisting of Mo (red ball) and S₂ (grey balls) located at the corners of hexagons is seen in the top view. (b) Corresponding Brillouin zone with symmetry directions. Taken from Ataca *et al.*[1] 25
- 3.2 (a) Calculated phonon dispersion curves of 2H-MoS₂, $\Omega(\mathbf{k})$ versus \mathbf{k} along symmetry directions of BZ and corresponding density of states (b). (c) and (d) are the same as (a) and (b) for 1H-MoS₂. (e) Difference of the densities of states of 2H-MoS₂ and 1H-MoS₂ (see text). Phonon branches derived from neutron scattering data[2] and branches calculated by using a local basis set[3, 4] are indicated in (a) and (c) by green (light) squares, respectively. Infrared (IR) and Raman (R) active modes with symmetry representations and frequencies (cm⁻¹) at the Γ -point are indicated. Taken from Ataca *et al.*[1] 31
- 3.3 Calculated phonon frequencies, $\Omega(\mathbf{k})$ of the bare armchair MoS₂ nanoribbon with $w= 17.75 \text{ \AA}$ or $n=12$ (there are 36 atoms in the primitive cell) are presented along symmetry directions of the Brillouin zone using Small Displacement Method (SDM), and corresponding densities of states (DOS). Taken from Ataca *et al.*[5] . . 35

- 3.4 (a) Top and side views of atomic structure of 2D 1H-MoS₂ with hexagonal lattice. The hexagonal unit cell with lattice constants $|a| = |b|$ is delineated by thin solid lines. Honeycomb structure consisting of Mo and S₂ atoms located at the corners is highlighted by dotted hexagons. (b) Contour plots of charge density, ρ (see text for definition) in a vertical plane passing through Mo-S bonds. Arrows indicate the increasing value of charge density. (c) Isosurface plot of difference charge density, $\Delta\rho$ (see text for definition). Isosurface value is taken as 0.006 electrons/Å³. (d) Energy band structure of 1H-MoS₂ calculated by GGA+PAW using optimized structure. Zero of energy is set to the Fermi level indicated by dash-dotted line. The gap between valence and conduction band is shaded; GW₀ corrected valence and conduction bands are shown by filled circles. (e) Total density of states (TDOS) and orbital projected density of states (PDOS) for Mo and S. Taken from Ataca *et al.*[6] 40
- 3.5 (a) Energy band structure of bare A-MoS₂NR having $n=12$ and the width $w=17.75$ Å. The band gap is shaded and the zero of energy is set at the Fermi level. At the right-hand side, charge density isosurfaces of specific states at the conduction and valence band edges are shown. (b) Same as (a), but the edge atoms are saturated by H atoms as described in the text. Large (purple), medium (yellow) and small (blue) balls are Mo, S, and H atoms, respectively. Short and dark arrows indicate the direction of the axes of nanoribbons. Total number of atoms in the unit cells are indicated. Taken from Ataca *et al.*[5] 43

- 3.6 Atomic and energy band structure of bare and hydrogen saturated zigzag nanoribbon Z-MoS₂NR having $n=6$ Mo-S₂ basis in the primitive unit cell. The top and side views of the atomic structure together with the difference of spin-up and spin-down charges, $\Delta\rho = \rho^\uparrow - \rho^\downarrow$, are shown by yellow/light and turquoise/dark isosurfaces, respectively. The isosurface value is taken to be 10^{-3} electrons per \AA^3 . The (2x1) unit cell with the lattice constant $2a$ is delineated. Large (purple), medium (yellow) and small (blue) balls are Mo, S, and H atoms, respectively. The zero of energy is set at the Fermi level shown by dash-dotted green/dark lines. Energy bands with solid (blue) and dashed (red) lines show spin-up and spin-down states, respectively. (a) The bare Z-MoS₂NR having $\mu=2 \mu_B$ per cell displays half-metallic properties. (b) Spin-polarized ground state of Z-MoS₂NR with Mo atoms at one edge and bottom S atoms at the other are passivated by single hydrogen. (c) Similar to (b), but Mo atoms are passivated by two hydrogen atoms. (d) Similar to (c), but top S atoms at the other edge are also passivated by single hydrogen atoms. The net magnetic moment of each case is indicated below the corresponding band panels. Bands are calculated using double cells. Small arrows along z -axis indicate the direction of the nanoribbon. The total number of atoms in supercell calculations are indicated for each case. Taken from Ataca *et al.*[5]

- 3.7 Top and side views are the schematic representation of possible adsorption geometries of adatoms obtained after the structure optimization. Adatoms, host Mo and S atoms are represented by red (large-dark), purple (medium-gray) and yellow (small-light) balls, respectively. Side views clarify the heights of adatoms from Mo and S atomic planes. Different adsorption sites are specified below each entry as 'Mo(S)-#', where Mo(S) indicates that adatoms are placed initially (before structure optimization) to Mo(S) plane. In Mo-1 and Mo-2 geometries the adatoms are in and slightly above the Mo-layer. S-1, S-2,.. S-4 positions are associated with the S-layer. The adatoms adsorbed at each site are given at the lower right hand side of each entry. Taken from Ataca *et al.*[6] 46
- 3.8 Schematic diagram of the relevant energy levels (or bands) of single adatom (O, Ti, Cr and Ge) adsorbed to each (4×4) supercell of 1H-MoS₂. The grey (light) shaded region in the background is the valence and conduction band continua. For nonmagnetic case, red (dark) bands are contributed more than 50% by adatoms orbitals, For magnetic case, spin-up and spin-down bands are shown by red (dark) and brown (light) lines, respectively. Solid bands indicate that the contribution of adatom to the band is more than 50%. In the lower part of each panel the adsorption site is indicated by the labeling of Fig. 3.7. Charge density isosurfaces of adatom states specified by numerals are shown below. The isosurface value is taken as 2×10^{-5} electrons/Å³. Taken from Ataca *et al.*[6] 50

- 3.9 Analysis of bonding configuration of C adatoms on 1H-MoS₂. (a) Geometries of single C adatom adsorbed in the Mo-plane (left) and in the S-plane (right). Adatoms, host Mo and S atoms are represented by red (medium-dark), purple (large-gray) and yellow (small-light) balls, respectively. (b) Contour plots of total charge density of plane passing through atoms and bonds highlighted (not shaded) in (a). (c) Contour plots of total charge density on the horizontal plane passing through Mo-C and S-C bonds parallel to 1H-MoS₂. (d) Adsorption geometry and energetics of C₂ and C₃ on 1H-MoS₂. (e) Contour plots of total charge density on the vertical plane passing through atoms and bonds emphasized (not shaded) in (d). The direction of the arrows indicate the increasing charge density. Taken from Ataca *et al.*[6] 53
- 3.10 Top and side views for the schematic representation of possible adsorption geometries of adatoms obtained after the structure optimization. Adatoms, Mo and S are represented by red (large-dark), purple (medium-gray) and yellow (small-light) balls, respectively. Side view clarifies the height of adatoms from Mo and S atomic planes. In each possible adsorption geometry, the entry on the lower-left part indicates where the adatom is initially placed. All sites show geometries associated with the adsorption to a bare armchair (n=12) nanoribbon (NR). The calculations are carried out in the supercell geometry where a single adatom is adsorbed at every three unit cells. The total number of atoms in the supercell is 109. Possible adsorption geometries in NR_{IE} (adatom is initially placed at the inner edge of bare armchair NR) and NR_{OE} (adatom is initially placed at the outer edge of bare armchair NR). Adatoms indicated at lower right part of every possible adsorption geometry correspond to those, which are relaxed to this particular geometry upon structure optimization. Taken from Ataca *et al.*[5] 54

- 3.11 Isosurfaces of difference charge density of MoS₂ vacancy defect in the (7x7) supercell of 1H-MoS₂. Dashed atoms and bonds are vacant sites. Difference charge density is obtained from the difference of spin-up and spin-down charge densities. ($\Delta\rho_{\uparrow,\downarrow} = \rho_{\uparrow} - \rho_{\downarrow}$) The total magnetic moment is calculated as $2\mu_B$. Up arrow indicate the excess spin-up charge. Isosurface value is taken as $3 \times 10^{-3} \text{ eV}/\text{\AA}^3$. Taken from Ataca *et al.*[6] 59
- 4.1 Atomic structure and charge density analysis of 2D single layer MoO₂ as a prototype. (a) Top and (b) side views of H-structure showing the primitive unit cell of 2D hexagonal lattice with Bravais lattice vectors \vec{a} and \vec{b} ($|\vec{a}|=|\vec{b}|$) and relevant internal structural parameters. Large (gray) and small (red) balls indicate metal (M) and oxygen (X=O) atoms, respectively. (c) Contour plots of the total charge density, ρ_T . (d) Isosurfaces of difference charge density, $\Delta\rho$. Turquoise and yellow regions indicate depletion and accumulation of electrons, respectively. (e) Isosurfaces showing *p-d* hybridization in Mo-O bond. Isosurface value is taken as 0.01 electrons/ \AA^3 . In the top view in (a), unlike graphene M and X₂ occupy the alternating corners of a hexagon. 64
- 4.2 Atomic structure and charge density analysis of NiS₂ as a prototype. (a) Top and (b) side views of T-structure showing the primitive unit cell of 2D hexagonal lattice with Bravais lattice vectors \vec{a} and \vec{b} ($|\vec{a}|=|\vec{b}|$) and relevant internal structural parameters. (c) Contour plots of the total charge density, ρ_T . (d) Isosurfaces of difference charge density, $\Delta\rho$. Turquoise and yellow regions indicate depletion and accumulation of electrons, respectively. (e) Isosurfaces showing Ni-S bonds. Isosurface value is taken as 0.01 electrons/ \AA^3 . In the top view in (a), while one of two X atoms occupies alternating corners of a regular hexagon, the second X atoms are displaced by $(\vec{a} + \vec{b})/3$ to occupy the centers of the adjacent hexagons. 65

- 4.3 Top and side views of atomic structures of selected MX_2 compounds obtained after ab-initio molecular dynamic (MD) calculations after specified time steps and temperatures. Numerals below each panel indicate the number of MD time steps. MD results at $T=1000\text{K}$ are also shown for structures, which become unstable at $T=1500\text{K}$ 70
- 4.4 Calculated electronic band structures of 2D stable MX_2 compounds which are stable in H-structure. The zero of the energy is set to the Fermi level, E_F , shown by red/dark dashed dotted line. The energy gap of semiconductors are shaded (yellow/light). For non-magnetic states spin-degenerate bands are shown blue/dark line. For magnetic structures, blue/dark lines represent spin-up bands whereas orange/medium lines are spin-down states. In the same row stable structures with the same M atom, but with different X atoms are presented. Columns present MX_2 manifold with the same X, but differing M atoms. The manifold MoX_2 ($X=\text{O}, \text{S}, \text{Se}, \text{Te}$) in H-structure is presented separately in Fig. 4.6. 74
- 4.5 Calculated electronic band structures of 2D stable MX_2 compounds, which are stable in T-structure. The zero of the energy is set to the Fermi level, E_F , shown by red/dark dashed dotted line. The energy gap of semiconductors are shaded (yellow/light). For nonmagnetic states spin-degenerate bands are shown blue/dark line. For magnetic structures, blue/dark lines represent spin-up bands whereas orange/medium lines are spin-down states. The manifold MX_2 with the same M atom, but with different X atoms is presented in the same row. Columns present MX_2 manifold with the same X, but differing M atoms. 75

- 4.6 Calculated energy band structures, charge density and state densities of single layer MoX_2 ($\text{X}=\text{O}, \text{S}, \text{Se}$ and Te). Left panels are iso-surface charge densities of the specific states at the band edges indicated by numerals. Isosurface value is taken as $0.01 \text{ electrons}/\text{\AA}^3$. Middle panels are band structures along the $M - \Gamma - K - M$ directions of Brillouin zone. The LDA band gap between conduction and valence band is shaded. The zero of energy is set at the Fermi level, E_F , shown by red/dark dashed dotted line. The GW_0 corrected bands are indicated by orange/light dashed lines and dots. The GW_0 corrected band gap of 3D 2H- MoS_2 is indicated by green/dark lines and diamonds. Direct and indirect band gap values are given in units of eV. Right panels are total and orbital projected densities of states DOS. 78
- 4.7 Comparison of the electronic structures of specific suspended MX_2 compounds forming both stable T- and H-structures. (a) Total densities and orbital projected densities of states (DOS) of 2D VS_2 , VSe_2 and VTe_2 compounds in T-structure. (b) Same for 2D VS_2 , VSe_2 and VTe_2 compounds in H-structure. (c) Total and orbital projected densities of states of 2D NiS_2 , NiSe_2 and NiTe_2 compounds in T-structure. (d) Same for 2D NiS_2 , NiSe_2 and NiTe_2 compounds in H-structure. The zero of the energy is set to the Fermi level, E_F , shown by red/dark dashed dotted line. Up and down arrows indicate spin-up and spin-down densities of states. Total density of states are given by thick solid lines. 79
- 4.8 Variation of lattice constants, $|\vec{a}|=|\vec{b}|$ and band gap of 2D single layer ScO_2 (in T-structure), NiO_2 (in T-structure) and WO_2 (H-structure) compounds with U-J. The exchange term J is taken to be 1 eV. 81
- 4.9 Geometric structure after two hydrogen adsorption to S monomer terminated Mo edge of zigzag nanoribbon. 82

- 4.10 Summary of the results of our stability analysis comprising 44 different MX_2 compounds, which may form stable, 2D single layer H- and/or T-structures. Transition metal atoms indicated by M are divided into $3d$, $4d$ and $5d$ groups. MX_2 compounds shaded light blue (gray) form neither stable H- nor T-structure. In each box the lower lying structure (H or T) has the ground state. The resulting structures (T or H) can be half-metallic (if specified by '+'), metallic (if specified by '*') or semiconductor (if specified by '**'). 85
- 5.1 (a) Schematic representation of (4x4) supercell of single layer 1H- MoS_2 . Purple and yellow balls are Mo and S atoms respectively. 1H- MoS_2 can be assumed as positively charged Mo hexagonal layer sandwiched between negatively charged hexagonal H layers. H_2O molecule is shown with red and orange balls, which are O and H atoms respectively. H_2 molecule does not bind to defectless (left side); S- and Mo- vacancy, S_2 di-vacancy (right side) defects on 1H- MoS_2 . The case in S_2 di-vacancy is shown. (b) Plot of variation of repulsive Coulomb force between defectless 1H- MoS_2 and H_2O . . . 90

- 5.2 Splitting of water molecule trapped in a MoS₂ triple-vacancy of 1H-MoS₂. (a) A free H₂O is approaching towards the MoS₂ triple-vacancy. Purple, yellow, red and orange balls indicate Mo, S, O and H atoms, respectively. (b) The precursor state occurs upon structure optimization and leads to the spontaneous splitting of H₂O into OH and H in an exothermic process. This state has the total energy, which is -2.85 eV lower relative to (a). (c) The most energetic (lowest energy) state, which occurred through ab-initio MD calculations at T=1000 K initiating from (b), where H atom is split from OH and is adsorbed to a two folded S atom surrounding the vacancy leaving behind O atom adsorbed to two four folded Mo atoms. This state has -3.39 eV energy relative to (a). (d), (e) and (f) are other intermediate states, which occur in the course of ab-initio MD calculation. Each panel presents both top and side views of atomic configurations. 93
- 5.3 Splitting of second water molecule trapped in the same MoS₂ triple-vacancy in monolayer 1H-MoS₂. In the middle of the hexagon, optimized structure of single O atom in MoS₂ triple-vacancy after the diffusion of two H atoms on 1H-MoS₂ is shown together with approaching water molecule. Purple, yellow, red and white balls indicate Mo, S, O and H, respectively. When the water molecule is trapped in triple-vacancy, its relaxed geometric structure is indicated in (a). On the corners of hexagon, optimized geometric structures taken from molecular dynamics calculations are indicated. Upper figure in each rectangle is the top view whereas bottom part is the side view of H₂O+MoS₂+O complex. The negative energy values indicate how much energy is released upon trapping of H₂O molecule. 95

- 5.4 Counterplots of total charge density of H, O and OH adsorption geometries. There are two sites where H adatom can be adsorbed with a positive binding energy. (a) Adsorption geometry and counterplot of total charge density on a plane passing through Mo atoms and H adatoms. Hydrogen adatom is adsorbed on Mo-layer. (b) Similar to (a), but the adatom is adsorbed at GM site. (c) Adsorption geometry and counter plot of total charge density of O adatom on MoS₂ tri-vacancy. (d) Adsorption geometry and counter plot of total charge density of OH molecule on MoS₂ tri-vacancy. Counterplots are drawn on two different planes. One covering Mo-O bond and O-H bond. A plane shown in every adsorption geometry indicates in which plane counterplots of total charge density is plotted. Purple, yellow, red and white balls are Mo, S, O and H, respectively. 98

- 5.5 Energy variation of a single isolated hydrogen adatom, H, moving along the special directions of 1H-MoS₂ honeycomb structure. (a) Each red dot corresponds to the minimum total energy of H on 1H-MoS₂ surface at a fixed x- and y-lateral position, but its height z together with all atomic positions of 1H-MoS₂ are optimized. B, T, HL and GM indicate bridge, top (of S and Mo), hollow and geometric minimum sites, respectively. The migration path of a single H is shown by dashed red lines on honeycomb. Relevant energy barriers are indicated by ΔQ_1 (occurs between HL-T=Mo indicated by 'x') and ΔQ_2 (occurs at B sites). (b) Similar to (a), but the diffusion direction is from Mo layer to S layer. Calculations are done in fixed z coordinate of H adatom whereas x- and y- coordinates of H together with all atoms of 1H-MoS₂ are relaxed. (c) Similar to (b), but the diffusion direction of H adatom is calculated on Mo layer of 1H-MoS₂. Purple, yellow and white balls indicate Mo, S and H atoms, respectively. (d) Total (TDOS) density of states of phonon frequencies of single H adsorbed on 1H-MoS₂. The density of states which is projected to the modes of H atom (PDOS). 101
- 5.6 (a) The interaction energy between two hydrogen adatoms on 1H-MoS₂; one is initially adsorbed at GM site (shown by blue ball) on the surface, the other (shown by an orange ball) moves on the path of minimum energy barrier. Within the adatom-adatom distance of 1.97 Å H adatoms begin to interact. At the end both adatoms on 1H-MoS₂ form H₂ molecule and release from the surface. Purple and yellow balls are Mo and S atoms, respectively. (b) Relevant atomic structures corresponding to some intermediate steps of ab-initio molecular dynamics calculations at T= 600 K. Initial distance between hydrogen atoms is taken as $d_{H-H}=3.2$ Å longer than the threshold distance. 103

- 5.7 Analytical solution to periodic Schrodinger equation with a potential term taken as the diffusion barrier indicated in Fig. 5.5(a) In (a) the particle (proton) is assumed to be diffusing between the nearest bridge (B) sites and making cyclic motion around S atom. On (b) and (c) the most probable diffusion paths of H atom are considered and passing over the diffusion barrier occurring in between HL and T=Mo sites. The diffusion paths for each case are indicated on honeycombs at lower right corners, respectively. The white regions indicate the vanishing of $|\phi|^2$ 105
- 5.8 Zigzag edge MoS₂ nanoribbon with 12 MoS₂ basis in the unitcell. S edge reconstructions are allowed and the calculations are done in supercell consisting of 4 unitcells in the direction of the nanoribbon. On the right hand side, bare and active edge structures are indicated. H₂O molecule is repelled from the defectless, S, S₂ and Mo vacant regions in the middle and active edges of MoS₂ nanoribbon. MoS, MoS₂ vacancy defects result in splitting of water, bare Mo edge results in the binding of H₂O without splitting. Purple, yellow, red and orange balls are Mo, S, O and H atoms, respectively. 108
- 5.9 Schematic representation of H₂O splitting in the MoS₂ vacancy defects of 1H-MoS₂. A H₂O is trapped and split in the vacancy defect. H atoms prefer to bind to two folded S atoms, where as O atom is strongly bind to four folded Mo atoms. By photon absorption, H atoms either releases or diffuses on 1H-MoS₂ surface. When H atoms are closer to each other than a threshold value, they combined and dissociated from 1H-MoS₂ surface. A second H₂O can also be trapped in the vacancy region. This time single H atom is released from H₂O molecule due to less charge transfer from five fold Mo atoms. Dissociation of H₂ is similar to previous case. Purple, yellow, red and orange balls are Mo, S, O and H atoms, respectively. 111

- 6.1 (a) Various adsorption sites H1, H2 and H3 on the (2×2) cell (top panel) and energy band structure of bare graphene folded to the (2×2) cell (bottom panel). (b) Charge accumulation, $\Delta\rho^+$, calculated for one Li atom adsorbed to a single site specified as H1 (top) and corresponding band structure. (c) Same as (b) for one Li atom adsorbed to H1-site, second Li adsorbed to H3-site of the (2×2) cell of graphene. Zero of band energy is set to the Fermi energy, E_F . Taken from Ataca *et al.*[7] 115
- 6.2 Adsorption sites and energetics of Li adsorbed to the (2×2) cell of graphene and absorption of H_2 molecules by Li atoms. E_L is the binding energy of Li atom adsorbed to H1-site, which is a minimum energy site. For H1+H2 or H1+H3 configuration corresponding to double sided adsorption, E_L is the binding energy of second Li atom and \bar{E}_L is the average binding energy. For H1, H1+H2 and H1+H3 configurations, E_1 is the binding energy of the first H_2 absorbed by each Li atom; E_n ($n=2-4$) is the binding energy of the last n^{th} H_2 molecule absorbed by each Li atom; \bar{E}_n is the average binding energy of n H_2 molecules absorbed by a Li atom. Shaded panel indicates the most favorable H_2 absorption configuration. Taken from Ataca *et al.*[7] 116

- 6.3 (a) Top-right panel: A (4×4) cell of graphene having four Ca atoms. As Ca at the initial position 0 is moved in the direction of the arrow, its z -coordinate is optimized. The remaining three Ca atoms are fully relaxed. Beyond the position 2 of the first Ca, the Coulomb repulsion pushes the second Ca atom in the same direction through positions 3' 4' and 5' to maintain a distance with the first Ca. Top-left: The variation of energy as the first Ca is moves through positions 1-5. (b) Bottom-right panel: Two Ca atoms adsorbed on each (4×4) cell of graphene with their initial positions 0 and 0'. As the first Ca moves from 0 to 1, the second one moves from 0' to 1' having the Ca-Ca distance of 3.74 \AA , whereby the energy is lowered by $\sim 0.176 \text{ meV}$. Two Ca atoms are prevented from being closer to each other and as the first Ca moves from 1 to 2,3,4 and 5 positions, the second one reverses his direction and moves through 2', 3', 4' and 5' in the same direction as the first Ca atom. Bottom-left: The variation of the energy with the positions of Ca atoms. Taken from Ataca *et al.*[8] 120

- 6.4 (a) The (2×2) cell of graphene lattice and the energy band structure of bare graphene folded to the (2×2) cell. (b) Single Ca atom is adsorbed on the H1 adsorption site of the (2×2) cell of graphene, energy band structure and corresponding total density of states (dotted blue-dark curve) and partial density of states projected to Ca- $3d$ orbitals (green-gray). Isosurfaces of the difference charge density, $\Delta\rho$, with pink (light) and blue (dark) isosurfaces indicating charge accumulation and charge depletion regions. Isosurface charge density is taken to be $0.0038 \text{ electrons}/\text{\AA}^3$. (c) Similar to (b) (excluding the partial and total density of states), but Ca atoms are adsorbed on both sides of graphene at the H1 and H2 sites. (H1+H3 configuration is also shown.) (d) Partial densities of states on H- s (red-dark) and Ca- $3d$ (green-gray) orbitals for 2, 3, and 4 H_2 absorbed in H1 configuration, and also isosurface of difference charge densities corresponding to $4\text{H}_2 + \text{Ca} + \text{Graphene}$ configuration. Zero of band energy is set to the Fermi energy, E_F . Taken from Ataca *et al.*[8] 122

- 6.5 Sites and energetics of Ca adsorbed on graphene with the (2×2) coverage and absorption of H₂ molecules by Ca atoms. d_c is the average C-C distance in the graphene layer. E_L is the binding energy of Ca atom adsorbed on H1-site, which is a minimum energy site. For H1+H2 or H1+H3 configurations corresponding to double sided adsorption, E_L is the binding energy of the second Ca atom and \bar{E}_L is the average binding energy. For H1, H1+H2 and H1+H3 configurations, E_1 is the binding energy of the first H₂ absorbed by each Ca atom; E_n ($n=2-5$) is the binding energy of the last n^{th} H₂ molecule absorbed by each Ca atom; \bar{E}_n is the average binding energy of n H₂ molecules absorbed by a Ca atom. Last row indicates the sites and energetics of one Ca atom adsorbed on each (4×4) cell of graphene and absorption of H₂ molecules by each Ca atom. Only the (4×4) coverage can absorb 5 H₂ molecules. The shaded panel indicates energetically the most favorable H₂ absorption configuration. Taken from Ataca *et al.*[8] 124

List of Tables

- 3.1 Lattice constants $|a|=|b|$ and c , and interlayer interaction energy E_i [per graphene (C_2) or MoS_2 unit] of graphite and 2H- MoS_2 calculated using GGA, GGA+D and GGA+DF and LDA methods. The corresponding values calculated for graphene and single layer MoS_2 are given in parenthesis. Experimental values are given for the sake of comparison. Experimental values of lattice constant a of 1H- MoS_2 given by Ref. [9, 10] appear to be too large and not confirmed. Taken from Ataca *et al.*[1] 27
- 3.2 Calculated frequencies of Raman (R) and Infrared (IR) active modes (in cm^{-1}) of 2H- and 1H- MoS_2 at the Γ -point and their symmetry analysis. The subscript u and g represent antisymmetric and symmetric vibrations, respectively. The other subscript i ($i = 1, 2, 3$) indicates the stretching modes. IR and R frequencies of 2H- and 1H- MoS_2 are calculated for the fully optimized lattice constants and internal structural parameters. Entries of IR and R frequencies of 2H- and 1H- MoS_2 indicated by (*) are calculated using the experimental lattice constants a and c of 2H- MoS_2 , but optimizing other internal structural parameters. The entry with (***) is calculated with $a=3.14 \text{ \AA}$ and corresponds to a , which is smaller than the experimental lattice constant a of 2H- MoS_2 . Taken from Ataca *et al.*[1] 32

- 3.3 Calculated values for the properties of 16 adatoms adsorbed on 1H-MoS₂. For specific adatoms, the first and second lines are associated with the adsorption to the Mo-layer and S-layer site, respectively. Other adatoms have only positive binding energy when adsorbed to the S-layer site. The adsorption sites of adatoms are described in Fig. 3.7. h_{Mo} , the height of the adatom from Mo layer; h_S , the height of the adatom from the nearest S-layer; d_{Mo} , the adatom-nearest Mo distance; d_S , the adatom-nearest S distance; E_b , adatom binding energy; μ_T , magnetic moment per supercell in Bohr magneton μ_B ; ρ^* , excess charge on the adatom (where negative sign indicates excess electrons); Φ , photoelectric threshold (work function); P, dipole moment calculated in the direction normal to 1H-MoS₂ surface. E_i , energies of localized states induced by adatoms. Localized states are measured from the top of the valence bands in eV. The occupied ones are indicated by bold numerals and their spin alignments are denoted by either \uparrow or \downarrow . States without the arrow sign indicating of spin alignment are nonmagnetic. Taken from Ataca *et al.*[6] 48

- 3.4 Calculated values of adatoms adsorbed to the bare armchair MoS₂ nanoribbon having $n=12$ MoS₂ units in the primitive unit cell. The supercell in calculations consist of three primitive cells. There are two different adsorption sites as (described in Fig. 3.10) for each adatoms. The positions only with a positive binding energy is indicated. h_{Mo} , the height of the adatom from Mo layer; h_S , the height of the adatom from the nearest S-layer; d_{Mo} , the adatom-nearest Mo distance; d_S , the adatom-nearest S distance; E_b , adatom binding energy; μ_T , magnetic moment per supercell in Bohr magneton μ_B ; ρ^* , excess charge on the adatom (where negative sign indicates excess electrons); Φ , photoelectric threshold (work function); P , dipole moment calculated in the x , y and z direction, respectively. Nanoribbon is in the (x, y) -plane and along the x -direction. E_i , energies of localized states induced by adatoms. Localized states are measured from the top of the valence bands in electron volt. The occupied ones are indicated by bold numerals and their spin alignments are denoted by either \uparrow or \downarrow . States without indicated spin alignment are nonmagnetic. Taken from Ataca *et al.*[5] 52
- 3.5 Calculated vacancy energies E_V (in eV), magnetic moments μ (in μ_B) of five different types of vacancy defects, Mo, MoS, MoS₂, S, S₂ in (7x7) supercell of 1H-MoS₂. NM stands for nonmagnetic state with net $\mu=0 \mu_B$. E_i s denote the energies of localized states in the band gap measured from the top of the valence bands (in eV). The occupied ones are indicated by bold numerals and their spin alignments are denoted by either \uparrow or \downarrow . States without the indication of spin alignment are nonmagnetic. Taken from Ataca *et al.*[6] 57

- 3.6 Calculated vacancy energies E_V (in eV), magnetic moments μ (in μ_B) of five different types of vacancy defects, Mo, MoS, MoS₂, S, S₂ in A-MoS₂NR and Z-MoS₂NR. NM stands for nonmagnetic state with net $\mu=0$. E_i , energies of localized states in the band gap. Localized states are measured from the top of the valence bands in electron volt. The occupied ones are indicated by bold numerals and their spin alignments are denoted by either \uparrow or \downarrow . Nonmagnetic states have no spin alignments. Taken from Ataca *et al.*[5] 60
- 4.1 Calculated values of stable, free-standing, 2D single layer MX₂ in H- and T-structures: Lateral lattice constants, $|\vec{a}| = |\vec{b}|$; bond lengths, d_{M-X} and d_{X-X} ; X-M-X bond angle, θ ; cohesive energy per MX₂ unit, E_C ; formation energy per MX₂ unit E_f (values in parenthesis are calculated using experimental cohesive energies of constituent elements[11]); energy band gap, E_g ; energy band gap corrected with GW₀ correction, $E_g^{GW_0}$ (only for selected compounds); total magnetic moment in the unitcell, μ ; excess charge on M atom (where positive sign indicates depletion of electrons), ρ_M ; excess charge on X atom (where negative sign indicates excess electrons), ρ_X ; in-plane stiffness, C ; 3D bulk structure of MX₂. Structures having indirect band gap according to *LDA* (and GW₀) calculations are indicated with bold face. Following abbreviations are used for 3D bulk structures: 4H = 4H-MX₂, 2H = 2H-MX₂, 3R = 3R-MX₂, 1T = 1T-MX₂ structure; R = Rutile, P = Pyrite, M = Molecule, Mcl = Monoclinic, Ma = Marcasite crystal structure. '*' stands for metastable crystal and '+' is distorted lattice structure. 68
- 4.2 Calculated differential chemisorption energy ΔE_H (see the text) for the first hydrogen atom to the edge of MX₂ nanoribbons. Values in parenthesis are for the second hydrogen atom. 83

5.1 First and second ionization energies, electronegativity and electron affinity of H, O, Cr, Mo, W, S, Se and Te for the search of other possible candidate structures of H₂O splitting. 109

Chapter 1

Introduction

A diminution in the petroleum reserves and boost in CO₂ emissions after the industrial revolution forced the research towards discovering cleaner and new fuel sources. Increasing demand in a clean energy source yielded researchers to search for alternatives which can be obtained, stored, carried and burned easily, safely and cheaply. Among all priorities for new generation fuel, hydrogen molecule having byproduct of only water, after burning is assumed to be the most probable and the cleanest and environmentally friendly fuel source of the future. However free hydrogen does not occur in quantity and thus it must be generated from some other energy sources, materials. Hydrogen is therefore an energy carrier. Few requirements left for scientists to discover is producing H₂ cheaply from renewable energy sources.

Hydrogen economy towards the utilization of hydrogen as a clean and sustainable energy source has three ingredients. These are (i) hydrogen production; (ii) hydrogen storage; and (iii) fuel cells. The first improvement in hydrogen research was the discovery of fuel cells for burning hydrogen molecule to obtain electricity and water as byproducts in late 20th century. There are many different types of fuel cells with different chemistry. They are usually classified by their electrolyte type and the operating temperature. Polymer exchange membrane (PYEMIC), solid oxide (SOFC), and molten-carbonate (MCFC) are the most known types. SOFC and MCFC require high operating temperature and are suitable for large

stationary power generators. PYEMIC will be the type which will be part of our daily life in near future. They operate slightly above room temperature and optimized for small power needs. A PYEMIC consists of 4 parts. These are anode (contains pressured H_2), cathode (where O^{2-} and H^+ combine to form H_2O), electrolyte (proton exchange membrane, where the special reaction occurs) and the catalyst (facilitates the reaction of oxygen and hydrogen in cathode). The membrane blocks electrons. In order pressured H_2 to pass from anode to cathode, molecule is separated and released its electrons. Only protons can pass from the membrane. The electrons pass from the electronic circuits connected to fuel cell, and power the device. The design of desired fuel cells for specific purposes, in terms of heat transfer, optimum area of the stacks is challenging engineering problem.

The realization and the raise of research on fuel cells in mid twentieth century show great importance since fuel cells yielded new research areas such as high capacity hydrogen storage and production of H_2 molecule. These are needed for commercializing the everyday use of the new fuel. Nowadays, there is an increasing research on materials functionalized specifically for high capacity hydrogen storage and production. Once hydrogen is chosen for a potential fuel of the future devices, one has to consider its storage, ease of charge and discharge mechanism. H_2 molecule can be stored in various methods. The easiest one is to store in pressured tanks. The energy cost of pumping H_2 to desired pressures requires comparable energy to the amount you can get from stored H_2 . For example to compress hydrogen to 10000 psi will require a loss of %15 of the energy contained in the hydrogen. A requirement of heavy and substantial tanks to handle the high pressure is the main drawback of this method to use H_2 in transportation. If you liquefy it, one will be able to get more hydrogen energy into a smaller volume, but that requires \sim %30 – 40 of the energy in hydrogen. Also the use of H_2 tanks in vehicles is not suitable.

The most promising, way to store H_2 is using nanotechnology. Using a host medium, generally chosen from light materials, and a dopant which can physisorb H_2 molecule, one can store H_2 molecule in this medium. Since the interaction

between dopant and H_2 is weak slow kinematics, poor reversibility and high dehydrogenation temperatures can be overcome. Recently, much effort has been devoted to engineer carbon based nanostructures[12, 13, 14, 15] which can absorb H_2 molecules with high storage capacity, but can release them easily in the course of consumption in fuel cells. Synthesis of carbon nanotubes and recently graphene[16] (both sides can be used for storage purposes) has made these materials a good candidate for high capacity hydrogen storage. Functionalization of these carbon based materials by transition metal, alkaline and alkaline halide atoms which can hold H_2 molecules by Dewar-Kubas interaction or other types of bonding have been a promising way for H_2 storage. In particular, our calculations on Li and Ca adsorbed on graphene from both sides have indicated that these systems are capable of storing hydrogen with 12.8 % wt, which is known to be higher than the limit set by the Department of Energy in US.

Production of H_2 can be obtained from various methods. It can be converted from fossil fuels, such as natural gas which releases nitrogen oxides. These methods are not environmentally friendly since nitrogen oxides are tens of times more effective in trapping heat than CO_2 . The simplest method is to obtain H_2 from electrolysis of water. The important thing is that from where you produce the electricity. Fossil based electricity production can pollute the environment much more than direct conversion of fuel to desired energy type. One must use renewable energy sources to produce the required amount energy in electrolyses. The most probable production method of H_2 taking into account environmental concerns is using water and the sunlight. Two methods dominated in achieving this goal. First one includes photogeneration cells. In this type of photoelectrochemical reactions, electrolysis of water is taken place, when anode is shined by solar radiation. Semiconductor surfaces or metal complexes in-solution are used to absorb solar energy and act like an electrode. Expensive platinum based electrodes and corrosion of semiconductor surfaces in contact with water are the down sides of this method.[17, 18] Another method, powder based photocatalytic reactions, offers a more efficient and cheap way of producing H_2 . This type of experimental setup includes only water and the photocatalyst to operate. Photocatalysts split the water into its constituents. Nowadays scientists are working

very hard to discover a suitable and sustainable photocatalysts which can operate under visible sun light, and can be produced cheaply.

Exceptional properties, such as high carrier mobility, linearly crossing bands at the Fermi level and perfect electron-hole symmetry which originates from the strictly two-dimensional (2D) honeycomb structure, made graphene an attractive material for future applications.[16, 19] In addition, suspended 2D single layer BN[20] and much recently, single layer transition metal dichalcogenides, MoS₂[21] and WS₂[22] with honeycomb structure have been synthesized. Theoretical[23, 24, 5, 6, 1] and experimental studies dealing with the electronic structure, lattice dynamics, Raman spectrum[25, 3] and Born effective charges indicate that single layer MoS₂ is a nonmagnetic semiconductor displaying exceptional properties. These properties of single layer MoS₂ and its nanoribbons[5] are exploited in diverse fields like nanotribology,[26] hydrogen production,[27] hydrodesulfurization[28] and solar energy production.[29] Most recently, a transistor fabricated from single MoS₂ layer pointed out features of these materials, which can be superior to graphene.[30] While graphene is ideal for fast analog circuits, single layer MoS₂ appears to be promising for optoelectronic devices, solar cells and LEDs. Our thesis aims to develop nanostructures for high capacity hydrogen storage and efficient production of H₂. For the storage we considered functionalization of graphene by Li and Ca, obtained high wt % storage capacity. Our extensive study on MoS₂ motivates us to consider it for H₂ production.

The main objective of this thesis is developing environmentally friendly method to produce H₂ from H₂O and high capacity hydrogen storage medium. Graphene is used for H₂ storage medium, because of its high surface per volume ratio. Both surfaces of graphene can be used as a high capacity hydrogen storage medium upon their functionalization with adatoms.

In Chapter 2, the details of the computational methods will be discussed. Our predictions are based on first-principles density functional theory (DFT) and finite temperature molecular dynamics. Chapter 3 focuses on electronic, magnetic, elastic, mechanical, vibrational and dimensionality effects of MoS₂ structure. This chapter covers our work on three-, two- and one- dimensional MoS₂ together with

functionalization of these structures. In Chapter 4, we go beyond MoS₂ structure. We predicted stable, single layer MX₂ transition metal dichalcogenides in honeycomb like structure. Similarities and differences between MoS₂ and predicted structures are discussed based on mechanical, electronic, magnetic and vibrational properties. In Chapter 5, we will present our predictions on hydrogen production following splitting of H₂O in vacancy defects of single layer MoS₂. Chapter 6 deals with our studies on hydrogen storage on graphene functionalized by Li and Ca adatom adsorption. In Chapter 7, we will conclude the thesis, discussing novel results and future applications of our predictions.

Chapter 2

Methodology - Density Functional Theory

The rise of Quantum Theory (QM) opens a new era in physics. We begin to have the ability to describe the systems in atomic scale and state its energetics. In early times, when the models and calculations are not optimized and the computational power is not so high, scientists prefer experimenting instead of modeling. As the time passed more accurate theories have been invented and computer power increases such that ‘The boundary of feasible quantum mechanical calculations has shifted significantly, to the extent that it may now be more cost effective to employ quantum mechanical modeling even when experiments do offer an alternative.’ Physicists have developed many methods, which can be used to calculate a wide range of physical properties of materials with high accuracy, such as lattice constants, structural parameters, mechanical, electronic and magnetic properties. These methods, which require only a specification of the ions present (by their atomic number), are usually referred to as ab initio methods.[31] While the specification by ab initio has been sometimes a matter of debate, we usually identify our calculations as "first-principles".

There are many different ab initio methods which are optimized for different purposes. Among them, the total-energy pseudopotential methods stand alone,

because it can handle much more number of atoms in calculations. The effect of rise in the computational power can not be inevitable, which also means that there is an increasing class of problems for which it is more cost effective to use quantum-mechanical modeling than experiments to determine the physical parameters. One can easily state that the cost effectiveness of quantum-mechanical modeling methods over physical experimentation will continue to increase with time.

2.1 Overview of Approximations

To investigate the various electronic, magnetic, elastic, vibrational and geometric properties of a solid require calculations of QM total energy of the system and subsequent minimization of that energy with respect to electronic and nuclear coordinates. Due to the large mass differences between the nucleus and electrons, electrons respond to the same forces much faster than that of the nucleus. We can treat nuclei adiabatically meaning that we separate the nuclear and electronic coordinates in the many-body wave function. This is also known as Born-Oppenheimer approximation.

The total energy calculations then include density functional theory to model the electron-electron interaction, pseudopotential theory to model the electron-ion interactions, supercells to model systems with periodic geometries and iterative minimization techniques to relax the electronic coordinates.

2.2 Electron-Electron Interaction

The main idea behind Density Functional Theory (DFT) is to model electrons as a single particle moving in an effective nonlocal potential instead of solving strongly interacting electron gas. Since electrons are fermions in many electron system, the wave function is antisymmetric under the exchange of any two electrons. Having the wave function antisymmetric results in spatial separation between electrons

that have the same spin and this reduces the Coulomb energy of the electronic system. This process which reduces the total energy is known as exchange energy. If electrons that have opposite spins are also spatially separated, the Coulomb energy of the total system can also be reduced below its Hartree-Fock value. The Coulomb energy of the system is reduced, but the kinetic energy of electrons did increased. The difference in energy between the results obtained from Hartree-Fock approximation and the many-body energy of an electronic system is known as correlation energy.

Density Functional Theory is developed by Hohenberg, Kohn and Sham for describing the effects of exchange and correlation in an electron gas. Hohenberg and Kohn showed that total energy of an electron gas can be modeled as a unique functional of electron density. Kohn and Sham then demonstrated how to represent the many-electron problem by exactly equivalent set of self consistent one-electron equations.

The Kohn-Sham Hamiltonian for a set of doubly occupied electronic states is given as:

$$E[\psi_i] = 2 \sum_i \int \left[-\frac{\hbar^2}{2m} \right] \nabla^2 \psi_i d^3r + \int V_{ion}(r) n(r) d^3r + \frac{e^2}{2} \int \frac{n(r)n(r')}{|r-r'|} d^3r d^3r' + E_{XC}[n(r)] + E_{ion}(R_I) \quad (2.1)$$

E_{ion} is the Coulomb energy provided with interactions among the ions (nucleus) at position R_I , V_{ion} is the total electron-ion potential, $n(r)$ is the electron density and $E_{XC}[n(r)]$ is the exchange-correlation functional. The charge density, $n(r)$, is:

$$n(r) = 2 \sum_i |\psi_i(r)|^2 \quad (2.2)$$

Determining the set of wave functions ψ_i that gives minimum Kohn-Sham energy functional:

$$\frac{-\hbar^2}{2m} \nabla^2 + V_{ion}(r) + V_H(r) + V_{XC}(r) \} \psi_i(r) = \epsilon_i \psi_i(r) \quad (2.3)$$

Here ψ_i represents the wave function of the i^{th} electronic state and ϵ_i represents the corresponding eigenvalue. $V_H(r)$ is the Hartree potential and $V_{XC}(r)$ is the exchange correlation potential.

$$V_H(r) = e^2 \int \frac{n(r')}{|r - r'|} d^3r' \quad (2.4)$$

$$V_{XC}(r) = \frac{\delta E_{XC}[n(r)]}{\delta n(r)} \quad (2.5)$$

These equations represent a mapping of the interacting many-electron system to a system of noninteracting electrons in an effective potential caused by all other electrons. We must solve these equations self consistently. The occupied electronic states generate a charge density. From this electronic potential is calculated and used in constructing these equations. The Kohn-Sham eigenvalues are not the energies of the single particle electron states, but rather the derivatives of the total energy with respect to the occupation numbers of these states. Nevertheless, the highest occupied eigenvalue in an atomic or molecular calculation is nearly the unrelaxed ionization energy for that system.[32]

The universally used and easiest method used for describing the exchange-correlation energy of an electronic system is local-density approximation (LDA). The main idea behind this approximation is that the exchange-correlation energy of an electronic system is constructed by assuming that the exchange-correlation energy per electron at a point r in the electron gas, $\epsilon_{XC}(r)$, is equal to the exchange-correlation energy per electron in a homogeneous electron gas that has the same density as the electron at point r .

$$E_{XC}[n(r)] = \int \epsilon_{XC}(r)n(r)d^3r \quad (2.6)$$

$$\frac{\delta E_{XC}[n(r)]}{\delta n(r)} = \frac{\delta[n(r)\epsilon_{XC}(r)]}{\delta n(r)} \quad (2.7)$$

$$\epsilon_{XC}(r) = \epsilon_{XC}^{hom}[n(r)] \quad (2.8)$$

LDA ignores corrections to the exchange-correlation energy at a point r due to nearby inhomogeneities in the electron density. Another functional, Generalized Gradient Approximation (GGA) is still a local, but takes into account the gradient of the density at the same coordinate in addition:

$$E_{XC}[n(r)] = \int \epsilon_{XC}(n, \vec{\Delta}n)n(r)d^3r \quad (2.9)$$

$$(2.10)$$

Shortly we can conclude that LDA appears to give a single well-defined global minimum for the energy of a non-spin-polarized system of electrons in a fixed ionic potential. For magnetic material, one has to expect more than one local minimum in energy. The global minimum of the system is then found by monitoring energy functional over a large region of phase space. By LDA, one can calculate structural, elastic and vibrational properties close to the reality. LDA results in overbinding of atoms, activation energies in chemical reactions are unreliable. Electronic and magnetic properties of structures can be usefully interpreted except for the accurate value of the band gaps. GGA is very good at calculating molecular geometries and ground state energies. GGA corrects the LDA overbinding problem, but this time it results in underbinding. If GGA predicts the binding, it is also predicted by LDA and verified by experiments. On the other hand, if GGA predicts nonbinding, there are cases where LDA as well as experiments can yield binding.[33, 34, 35, 36, 37, 38, 39] GGA softens the bonds by increasing the lattice constants and decreasing bulk moduli. While GGA fails to predict the interlayer interaction caused mainly by weak van der Waals (vdW) forces, the interlayer distance (of graphite and MoS₂), LDA is known to include

vdW interactions.[40, 41, 42, 43] These functionals can also be modified to include long range van der Waals interactions.

2.2.1 Method of Grimme: Introduction of van der Waals interaction

Popular density functionals are unable to describe correctly the van der Waals (vdW) interactions resulting from charge fluctuating charge distributions. A semi-empirical method is recently developed and solved the most suffered handicap of DFT. Taking into account the analytic solution of vdW interaction in solids which is the attractive interaction varies as the minus sixth power of the separation of the two oscillators, Grimme[44] implemented this to DFT as:

$$E_{DFT-D} = E_{DFT} + E_{disp} \quad (2.11)$$

$$E_{disp} = -s_6 \sum_{i=1}^{N_{at}-1} \sum_{j=i+1}^{N_{at}} \frac{C_6^{ij}}{R_{ij}^6} f_{dmp}(R_{ij}) \quad (2.12)$$

E_{DFT} is the usual self-consistent DFT energy, E_{disp} is the empirical correction term, where N_{at} is the number atoms in the unitcell, C_6^{ij} denotes the dispersion coefficient for atom pair ij and is $C_6^{ij} = \sqrt{C_6^i C_6^j}$. C_6^i is the empirical constant different for every atom. s_6 is the global scaling factor depends on which exchange-correlation functional is used in the calculation, R_{ij} is the interatomic distance. A damping function f_{dmp} is used in order to avoid near-singularities for small R_{ij} .

There are also other, fully self-consistent implementations of vdW interaction, but the cohesive energy and lattice constants of MoS₂ structure predicted with this approximation is not the closest to the reported experimental values. Detailed discussions on the effects of this and other vdW corrections on MoS₂ structure is indicated in foregoing chapters. It is important to note that inclusion of vdW in the calculations has negligible effects on the band structure since the corrections only affect only the lattice constants and the bond lengths in very small scale.

2.2.2 LDA+U: Correction in transition-metals

Difficulties and unreliable conclusions arise when a conventional spin polarized LDA approach is applied to the treatment of the electronic structure of material where some of the ions contain partly filled valence d or f orbitals. The origin of the failure of spin polarized LDA in transition metal oxides is associated with an inadequate description of the strong Coulomb repulsion between $3d$ electrons of localized on metal ions. Since the strength of the effective on-site Coulomb interaction between d electrons (Hubbard U : Coulomb-energy cost to place two electrons at the same site.) is comparable with valence bandwidth,[45] the processes related with charge transfer between two metal ions or resulting from addition or removal of d electrons give rise to large fluctuations of the energy of the system, leading to the localization of carriers and to the formation of band gaps. Taking into account the exchange integral for spin particles (J), Stoner parameter, one can modify the Hamiltonian of the system as:

$$E_{LSDA+U} = E_{LSDA}[\epsilon_i] + \frac{U - J}{2} \sum_{l,j,\sigma} \rho_{lj}^{\sigma} \rho_{jl}^{\sigma} \quad (2.13)$$

$$(2.14)$$

where ρ_{jl}^{σ} is the density matrix of d electrons σ is the spin direction and ϵ_i is the eigenvalues. In practice U is ~ 10 eV, where as J is around 1 eV. By varying (U-J) parameter, one can change the electronic and magnetic properties of the system. In order to find the accurate U and J values, one has to compare the band gap energies with the experimental results. If no experiments are available in transition metal oxides, there is no way to find the accurate (U-J) parameter, however the effects of the change in these parameters can be investigated.

2.3 Periodic Supercells

When the system is periodic there are infinitely many number of atoms and electrons. As a result we must include all of the interactions of these particles in our calculations. There are two difficulties of this result. Wave functions must be calculated for each of the infinitely many electrons in the system and the basis set required to expand each wave function is infinite. Here we will use Bloch's Theorem to make things easier.

This theorem states that in a periodic solid each electron wave function can be written as the product of a cell-periodic part and a wavelike part:

$$\psi_i(r) = \exp[ik \cdot r]f_i(r) \quad (2.15)$$

Periodic part of the wave function can be expanded using a basis set consisting of a discrete set of plane waves :

$$f_i(r) = \sum_G c_{i,G} \exp[iG \cdot r] \quad (2.16)$$

Here reciprocal lattice vectors G are defined by using the fact that $G \cdot l = 2\pi m$. Here l is a lattice vector and m is an integer. Then wave function for each electron can be written as :

$$\psi_i(r) = \sum_G c_{i,k+G} \exp[i(k+G) \cdot r] \quad (2.17)$$

By using the boundary conditions electronic states are allowed only at a set of k points in a bulk solid. There is a direct proportionality between the volume of the solid in reciprocal space and the density of allowed k points. By using the Bloch's Theorem we change the problem of calculating infinite number of electronic wave functions to the one of calculating a finite number of electronic

wave functions at an infinite number of k points. The electronic wave functions at k points that are very close together will be almost identical and hence it is possible to represent the electronic wave functions over a region of k space by the wave functions at a single k point. In this case the electronic states at only a finite number of k points are required to calculate the electronic potential and hence determine the total energy of the solid. The magnitude of any error in the total energy due to inadequacy of the k point sampling can always be reduced by using a denser set of k points. The computed total energy will converge as the density of k points increases.[46]

We can expand electronic wave functions at each k point any discrete plane wave basis set by Bloch's Theorem. The coefficients $c_{i,k+G}$ for the plane waves with small kinetic energy are typically more important than those with having a larger energy. By this way we can truncate the plane-wave basis set to include only plane waves that have kinetic energies less than some cutoff energy. Introduction of this cutoff energy to the discrete plane-wave basis set produces a finite basis set. The energy cutoff will lead to small error in total energy calculations, but increasing the value of the cutoff energy, the total energy will converge to a value. Plane-wave representation of Kohn-Sham equations are :

$$\sum_{G'} \left[\frac{\hbar^2}{2m} |k + G|^2 \delta_{GG'} + V_{ion}(G - G') + V_H(G - G') + V_{XC}(G - G') \right] c_{i,k+G'} = \epsilon_i c_{i,k+G} \quad (2.18)$$

The kinetic energy of electrons is diagonal, and the many potentials are described in terms of their Fourier transforms. The dimension of the matrix depends on the cutoff energy value we choose.

2.4 Electron-Ion Interactions

To perform calculation including the effect of all ions and electrons, an extremely large plane wave basis set would be required. The most physical properties of

solids are dependent on the valence electrons to a much greater extent than the core electrons. The pseudopotential approximation exploits this by removing the core electrons and by replacing them and the strong ionic potential by a weaker pseudopotential that acts on a set of pseudo wave functions rather than the true valence wave function. The valence wave functions oscillate rapidly in the region occupied by the core electrons due to the strong ionic potential in this region. These oscillations maintain the orthogonality between the core wave functions and the valence wave functions, which is required by the exclusion principle. The scattering from the pseudopotential must be angular momentum dependent because the phase shift introduced by the ion core is different for each angular momentum component of the valence wave function.

$$V_{NL} = \sum_{lm} |lm\rangle V_l \langle lm| \quad (2.19)$$

Here $|lm\rangle$ represents the spherical harmonics and V_l is the pseudopotential for the angular momentum. A local pseudopotential uses the same potential for all the angular momentum components and its amplitude is only a function of the distance from the nucleus.

We refer to the electron density in the exchange-correlation energy in total energy calculations. If we can find the accurate exchange-correlation energy, we must have the pseudo and real wave function to be identical in both amplitude and spatial dependencies. These will result in charge densities to be the same. Nonlocal pseudopotential that uses different potential for different angular momentum values will describe the scattering from the ion core the best.

As we use pseudopotential in our calculation we can use fewer plane wave basis sets. By this way we removed the rapid oscillations of the valence wave function in the core region of the atom. Small core region electrons are not present at this time. The total energy of the system is much less than the case of all-electrons, but the difference between the electronic energies of different ionic configurations is very similar to all electron case. We can conclude that the total energy is meaningless until now. The true and the important value are the differences in

energies.

2.5 Ion-Ion Interaction

The Coulomb interaction in real and reciprocal space is long ranged. Using Edwald's method, one can obtain the equation given below.

$$\sum_l \frac{1}{R_1 + l - R_2} = \frac{2}{\sqrt{2\pi}} \sum_l \int_\eta^\infty \exp[-|R_1 + l - R_2|^2 \rho^2] d\rho + \quad (2.20)$$

$$\frac{2\pi}{\Omega} \sum_G \int_0^\eta \exp\left\{-\frac{|G|^2}{4\rho^2}\right\} \exp[i(R_1 - R_2) \cdot G] \frac{1}{\rho^3} d\rho$$

Where l is lattice vectors and G is reciprocal lattice vectors and Ω is the volume of the unit cell as before. In this method we try to write the lattice summation of the Coulomb energy with respect to the interaction between an ion positioned at R_2 and an array of atoms positioned at $R_2 + l$. This valid for positive values of the variable η . If we can find an appropriate value for this variable, two summations became rapidly convergent. As a result real and reciprocal space summation can be calculated by few lattice vectors and few reciprocal vectors. For the calculation of the correct energy, we must remove $G = 0$ contribution of the Coulomb energy of the ionic system. Omitting $G = 0$ summation in reciprocal space finally we achieve the relation as :

$$E_{ion} = \frac{1}{2} \sum_{I,J} Z_I Z_J e^2 \left\{ \sum_l \frac{\text{erfc}(\eta |R_1 + l - R_2|)}{|R_1 + l - R_2|} - \frac{2\eta}{\sqrt{2\rho}} \delta_{IJ} + \quad (2.21)$$

$$\frac{4\pi}{\Omega} \sum_{G \neq 0} \frac{1}{|G|^2} \exp\left\{-\frac{|G|^2}{4\eta^2}\right\} \cos[(R_1 - R_2) \cdot G] - \frac{\pi}{\eta^2 \Omega} \right\}$$

Z is the valances of ions I and J . erfc is the error function. $L = 0$ term is neglected because ion does not interfere with its own charge.

2.6 Parameters of DFT Calculations

2.6.1 Pseudopotential Choice

The cost of including the all electrons of each atom in the unitcell is very high since computational time grows significantly by number of electrons. In order to avoid this, we use pseudopotentials in our calculations. These potentials behave the same with the all electron wavefunctions after a cut off radius. Distances before the cut off radius they are not correct. In this thesis we used two different types of pseudopotentials. These are ultrasoft (US)[47] and projector augmented plane waves (PAW)[48]. The differences between them arise in the core region where all electron wavefunctions and pseudowavefunctions differ. In the core region, PAW uses superposition of atomic orbital wavefunctions, however there is no restriction for US except norm conservation. PAW potentials have improved accuracy for magnetic materials, alkali and alkali earth elements, lathanides and actinides. In case of compounds where often species with very different covalent radii are mixed, The PAW potentials are clearly superior. In our calculations, we prefer PAW potentials whenever possible. Most of our calculations are done using VASP software where all PAW potentials are available.[49, 50] In some cases we use PWSCF[51] to check the results and make calculations using density functional perturbation theory, but this software uses US pseudopotentials. We use US potentials in our works on vibrational analysis of MoS₂ structure and hydrogen storage on Li adsorbed graphene structure. Other studies are carried out using PAW potentials.

An element can have various PAW potentials available. The main differences between the potentials depends on which electrons are taken as core electrons and cut off radii of the potential. Generally in modeling transition metal atoms, we take s and d orbitals as valance electrons and left others as core region. In the case of potentials with different cut off radii, our choice depends on the predicted bond length between atoms of the compound. The bond length has to be larger than the sum of cutoff radii of bonding atoms.

2.6.2 Exchange Correlation Functional Choice

We have discussed formalism of LDA and GGA before. The fully treated inclusion of van der Waals interaction in GGA calculations is a very recent improvements. The source was available for us after the beginning of 2011. For this reason the exchange correlation functional in studies that are done, started before this date in this thesis, depend on whether we wanted partly to include vdW partly in the calculations. LDA method is used for partial inclusion of vdW interaction. Our studies on hydrogen storage and prediction of novel transition metal dichalcogenides are done using LDA. GGA method is used on investigation of electronic, magnetic, mechanical and elastic MoS₂ structure. The most precise method including vdW interaction nowadays is GGA method with vdW corrections. This method is used in investigation of vibrational properties of MoS₂ structure and splitting of H₂O on the vacancy defects of MoS₂. All of our calculations are carried out by taking into account spin polarization. Since the electrons of some of transition metal oxides are strongly correlated, they may not be represented properly by DFT. Thus, to correct the deficiencies of DFT we also carried out LDA+U calculations[52] for the prediction of electronic and magnetic structures of transition metal dichalcogenides (MX₂).

2.6.3 Convergence Criteria and Stability Analysis

After selection of pseudopotential of atoms and exchange correlation functional, before starting extensive calculations, we have to determine the value of the cut-off potential and number of \mathbf{k} -points used in the calculation. Kinetic energy cut-off, Brillouin zone (BZ) sampling of the calculations have been determined after extensive convergence analysis. These analyses include the convergence of total energy of the system by increasing the value of cut-off potential and number of \mathbf{k} -points. A plane-wave basis set with kinetic energy cut-off of 600 eV is used. In the self-consistent field potential and total energy calculations BZ is sampled by special \mathbf{k} -points.[53] The numbers of these \mathbf{k} -points are (37x37x1) for the primitive MX₂, MoS₂ and graphene unitcell and are scaled according to the size

of the supercells. Since all of the works in this thesis is based on two dimensional structures, a large spacing of $\sim 15 \text{ \AA}$ between 2D single layers is taken to prevent interlayer interactions. All atomic positions and lattice constants are optimized by using the conjugate gradient method, where the total energy and atomic forces are minimized. The convergence for energy is chosen as 10^{-6} eV between two consecutive steps, and the maximum Hellmann-Feynman forces acting on each atom is less than 0.01 eV/\AA upon ionic relaxation. The pressure in the unit cell is kept below 5 kBar. Bader analysis is used to calculate the charge on atoms.[54] The frequency-dependent GW_0 calculations,[55] are carried out to correct the LDA band gaps. However, while the GW_0 correction was successful in predicting 3D bulk MoS_2 , it overestimates the band gap of 2D MoS_2 in H structure.[6]

In order for a structure to be stable, we carried out three-step stability analysis. First one is finding the global energy minimum of the system. These are simple DFT calculation where we change the lattice dimensions, atom positions to find the lowest energy minimum site. It is not always true that the lowest energy site is stable. A very nice example is silicene.[56] Even though geometry minimization calculations predict a geometry with a lower cohesive energy, the stable geometric structure is the excited state. In the second step, we carried out phonon calculations.

2.6.3.1 Phonon analysis

The energy of an elastic mode of angular frequency ω is $\epsilon = (n + \frac{1}{2})\hbar\omega$ when the mode is excited to quantum number n (when the mode is occupied by n phonons.) Quantizing the mean square of phonon amplitude considering the standing wave mode of amplitude $u = u_0 \cos Kx \cos \omega t$ where u is the displacement of an element from its equilibrium position. The energy in the mode is half kinetic energy and half potential energy when averaged over time. As a result, the square of the amplitude of the mode is:

$$u_0^2 = 4 \left(n + \frac{1}{2} \right) \hbar / \rho V \omega \quad (2.22)$$

Here ρ is the mass density and V is the volume. This relates the displacement in a given mode to the phonon occupancy n of this mode. ($n \geq 0$) The energy of phonon cannot be negative, so the right hand side of the above equation is positive. This results in positive or negative displacements of atoms in the crystal. However if the crystal structure is unstable, then ω will be negative and in this case atom displacements are calculated as imaginary. In terms of physical point of view, this means that the unstable crystal structure can not create a restoring force for the atoms displaced from their equilibrium positions. In order for a system to be stable, calculated ω has to be positive through out all Brillouin Zone.

We carry out phonon calculation using two different methods to check whether all vibrational frequencies are real and 0 or positive. These methods are based on Small Displacement Method (SDM)[57] and density functional perturbation theory.[51] Advantage of perturbative treatment of phonons is in ionic compounds, LO-TO splitting can be observed. This is absent in SDM method, since it only uses forces calculated from self consistent field to generate the dynamic matrix. Once phonons of the system is calculated, one can calculate the Born effective charges, dielectric constants (both at $\omega = 0$ and $\omega = \infty$). By using group theory analysis, looking at the symmetries of the unitcell, one can state the Raman and infrared active modes and their corresponding frequencies in $\omega = 0$. These are further discussed in shift of phonon modes of MoS₂ upon changing the dimensionality, that is the symmetry of the system.

2.6.3.2 Molecular Dynamics Calculations

The last step in our stability analysis is the ab-initio molecular dynamics (MD) calculations. In a classical MD calculation, forces acting on the atoms of crystal are calculated from force field, empirical or semi-empirical approaches and the atoms are displaced accordingly by the time step value supplied by the user. This calculations are carried on iteratively and a realistic movements of atoms are modeled taking into account the temperature effects. Since calculation of atomic forces are computationally much cheaper than ab-initio based calculations,

the duration of classical MD calculations can be comparable to real life time units. Generally these empirical methods does not include effects of electrons and magnetism in calculating the forces. MD calculations based on these may cause incorrect results if there are localized electrons in regions of crystal or change of magnetic state upon the transformation of the structure. However forces calculated from ab-initio methods are precise taking into account all the physical effects in real life, but on the other hand, they are computationally expensive. For this reason ab-initio MD calculations cannot be carried out at real life time durations. We use ab-initio MD calculations to investigate if a structure is stable in a minimum on the Born-Oppenheimer surface.

There are three different ensemble choices we can use in MD calculations. In a micro-canonical ensemble the number of particles N , volume of the system V , and the energy of the system E is kept fixed at each iterative steps. Canonical ensemble is similar to micro-canonical case, except temperature T is kept fixed instead of E . Grand canonical ensemble, which is the most suitable case for macroscopic states, permits the exchange of particles and energy from the environment. In ab-initio MD calculation, one cannot change the number of particles in a supercell and include too many number of atoms to model a macroscopic state. Generally ab-initio MD calculations at nanoscales can be modeled with micro-canonical and canonical ensembles. The main difference between them depends on normalization of either energy or temperature of the system. In reality some subset of a crystal can vibrate with a greater amplitude than the remaining parts at a small period of time. However expectation value of energy is the same over every part over a long period of time. Forcing the total energy to be fixed at very small time steps (micro-canonical ensemble) by normalizing the velocities of atoms in every part of the crystal may not be realistic for modeling a nanoscale area of crystal. For this reason, it is better to permit fluctuation of energy (canonical ensemble) over small length of times at nanoscale. We use canonical ensemble in our calculations which complies best with reality. The length of time steps is another important parameter in molecular dynamics calculations. By using this value, based on the calculated forces on the atoms, the atoms are displaced at

each iteration. Taking extreme values for this parameter leads to longer displacements in atoms at each step and may raise instabilities on the system which can breakup crystal structure. Smaller values are relevant for observing a reaction happening on a material. Average values for time steps are ~ 2 femto seconds. In each chapter this value is supplied when ab-initio MD calculations are carried out.

Chapter 3

Properties of MoS₂ Structure

3.1 Preliminary Information

Three-dimensional (3D) MoS₂, a well-known transition-metal dichalcogenide has two different stable structures: These are 3R-MoS₂ polytype[58] and layered 2H-MoS₂. The latter consists of the stacking of MoS₂ layers and is the subject matter of the present section. Various properties of 2H-MoS₂, (Ref.[59, 60, 61, 62, 2, 63, 64, 65, 66, 67, 68, 69, 70, 71, 72, 73]), in particular lattice dynamics and electronic energy band structure have been studied extensively. Liquid exfoliation of nanosheets of MoS₂ and other transition metal dichalcogenides, such as MoSe₂, WS₂, MoTe₂, NbSe₂, NiTe₂, are reported.[74] Recently 2D suspended single layer MoS₂ sheets, i.e. 1H-MoS₂ having hexagonal lattice have been produced.[75, 76, 77, 78] 1H-MoS₂ is made of hexagons with Mo and two S atoms situated at alternating corners. Single layer MoS₂ nanocrystals of ~ 30 Å width were also synthesized on the Au(111) surface[79] and the first direct real space STM images of single layer MoS₂ nanosheets have been reported. In the meantime, theoretical studies (Ref.[80, 81, 82, 83, 84, 72, 85, 5, 6]) on 1H-MoS₂ have appeared. Three-dimensional 2H-MoS₂ and 2D 1H-MoS₂,[6] quasi 1D nanotubes[82] and nanoribbons[5, 72, 83] of MoS₂ share the honeycomb structure and display interesting dimensionality effects.

Properties of MoS_2 nanocrystals are explored in diverse fields, such as nanotribology[86], hydrogen production[27, 87], hydrodesulfurization catalyst used for removing sulfur compounds from oil[88, 89, 90, 91, 92, 93, 94], solar cells [29], photocatalysis.[95] Triangular MoS_2 nanocrystals of diverse sizes were investigated using atom-resolved scanning tunneling microscopy.[96] Superlow coefficient of sliding friction between surfaces coated with 1H- MoS_2 has been measured much recently.[26] A transistor fabricated from the single layer MoS_2 has heralded the features of 1H- MoS_2 , which is superior to graphene.[30] Studies to date suggest that MoS_2 sheets can be promising for optoelectronic devices, solar cells, and LEDs. Most recently, the Raman spectra of MoS_2 sheets have been measured as a function of their thickness.[78, 3]

Despite the fact that 2H- MoS_2 is a layered material, where MoS_2 layers were bound by weak interlayer interaction, significant dimensionality effects have been observed. For example, while 3D MoS_2 is an indirect band gap semiconductor, the band gap increases and becomes direct in 2D single layer MoS_2 . [77] This dimensionality effect may lead to photoluminescence applications in nanoelectronics.[24] While the lattice dynamics of 2H- MoS_2 have been studied actively in the past by using inelastic neutron scattering and Raman-Infrared spectroscopy[2, 81] and its phonon dispersion curves, phonon density of states, Infrared and Raman active modes are calculated in terms of force constants derived from experimental data, yet an ab-initio treatment including van der Waals interaction (vdW) is absent. Recent papers[78, 3] investigating the Raman spectra of 3D and 2D MoS_2 came up with conflicting conclusions.

Various properties revealed earlier for 3D graphitic MoS_2 and nowadays for 2D single layer 1H- MoS_2 have made the functionalization of these structures by adatoms or vacancy defects a current issue. Ab-initio calculations were carried for adsorption of thiophene[97] on catalytically active surface of MoS_2 crystal, which is used in hydrodesulfurization process. Similarly, the adsorption of aromatic (thiophene, benzothiophene, benzene, naphthalene, pyridine, quinoline) and conjugated compounds (butadiene) on the basal plane (0001) of MoS_2 were studied.[71] Huang and Cho[70] investigated the adsorption of CO on MoS_2 surface and calculated the relative energies of different reaction paths. Implementing

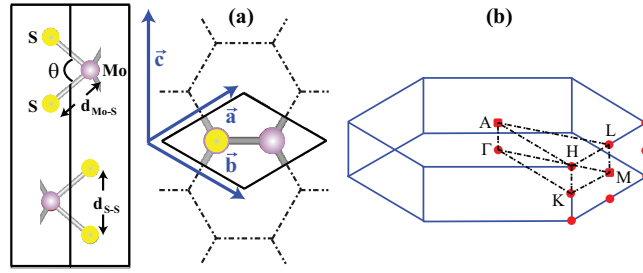


Figure 3.1: (a) Side and top views of atomic structure of 2H- MoS_2 with hexagonal lattice. The unit cell is delineated, lattice constants $|a| = |b|$, c and internal structure parameters are indicated. Honeycomb structure consisting of Mo (red ball) and S_2 (grey balls) located at the corners of hexagons is seen in the top view. (b) Corresponding Brillouin zone with symmetry directions. Taken from Ataca *et al.*[1]

local magnetism through defects or impurities has been the focus of first-principles calculations. Fuhr *et al.*[68] found that S vacancy defect on MoS_2 surface, as well as substitutional doping of Pd and Au do not induce magnetic moment, whereas Fe and V induce magnetic moments when substituted with S atoms at MoS_2 surface. Adsorption and substitutional doping of Nb atoms on MoS_2 surface were also investigated.[69] Since the magnetism based on sp -orbitals yields long-range exchange coupling interactions as compared to d - and f - orbitals, implementing magnetic properties to MoS_2 monolayer through nonmagnetic adatoms have been also considered. Theoretical studies concluded that H, B, C, N and O can significantly modify the magnetic and electronic properties of this material.[98]

In this section we present a systematic study to reveal the general properties of 1H- MoS_2 . These include: (i) Stability analysis of MoS_2 structure including nanoribbons. (ii) Electronic and magnetic properties of MoS_2 and its nanoribbons. (iii) Mechanical properties of, (iv) Functionalization through adatom adsorption in, (v) Vacancy defects in 1H- MoS_2 and its nanoribbons.

3.2 Optimized Structures of MoS_2

The interaction between 1H- MoS_2 layers in 2H- MoS_2 has predominantly vdW character. Therefore, DFT calculations within GGA but without vdW are known to overestimate the interlayer distance and the lattice parameter c in Fig. 3.1 (a). To present a correct estimation of lattice constants, we included vdW correction to GGA calculations using two different methods. The first one (GGA+D) is used mainly for molecules and corrects GGA by adding interatomic C_6/R^6 interaction. The C_6 coefficient and cutoff distance are deduced from relevant molecules.[99] Second method (GGA+DF) aims at solutions from the first-principles without empiricism and uses non-local exchange-correlation functional to treat vdW interaction in GGA.[100] The latter method is tested for molecules and solids. In order to find the most appropriate method we carried out GGA calculations without vdW correction, as well as GGA+D and GGA+DF calculations. For the sake of comparison, we also performed LDA calculations, which is known to include vdW interaction partially.[101, 102] In our analysis we consider two layered 3D crystals both having honeycomb structure, namely graphite and 2H- MoS_2 , in which the cohesions of layers are known to be achieved mainly by the weak vdW interaction. The optimized lattice constants $|a| = |b|$ and c , and interlayer interaction energy E_i calculated by using these methods are presented in Tab. 3.1. For comparison the experimental values are also given. The interlayer interaction energy or cohesion of 2H- MoS_2 relative to individual MoS_2 layers can be deduced by calculating the total energy of 2H- MoS_2 as a function of interlayer spacing z in the direction perpendicular to MoS_2 layer, i.e. $E_T(z)$ and by setting $E_T(z \rightarrow \infty) = 0$. Then the absolute value of half of the minimum of $E_T(z = c)$ is taken as E_i (interlayer interaction energy per layer).

For graphite, GGA without vdW attains the experimental a , but overestimates c by 25% relative to the experimental value.[103, 104, 105, 106, 107] Expectantly, the calculated interlayer interaction energy $E_i=5$ meV per layer is much smaller than the experimental value.[103, 104, 105, 106, 107] On the other hand, the values of c and E_i calculated for graphite are improved significantly when vdW correction is included. While GGA+DF overestimates c by 6.6%, GGA+D

Table 3.1: Lattice constants $|a|=|b|$ and c , and interlayer interaction energy E_i [per graphene (C_2) or MoS_2 unit] of graphite and 2H- MoS_2 calculated using GGA, GGA+D and GGA+DF and LDA methods. The corresponding values calculated for graphene and single layer MoS_2 are given in parenthesis. Experimental values are given for the sake of comparison. Experimental values of lattice constant a of 1H- MoS_2 given by Ref. [9, 10] appear to be too large and not confirmed. Taken from Ataca *et al.*[1]

	Graphite (Graphene)			2H- MoS_2 (1H- MoS_2)		
	a (Å)	c (Å)	E_i (eV/ C_2 KCal/Mole)	a (Å)	c (Å)	E_i (meV/ MoS_2 KCal/Mole)
GGA	2.461 (2.463)	8.407	5, 0.115	3.215 (3.214)	15.540	6, 0.138
GGA+D	2.461 (2.463)	6.425	122, 2.816	3.220 (3.220)	12.411	160, 3.693
GGA+DF	2.463 (2.463)	7.157	116, 2.678	3.258 (3.254)	13.152	176, 4.063
LDA+TF	2.411 (2.411)	6.669	96, 2.216	3.125 (3.118)	12.137	110, 2.539
Experiment	2.461-2.463[103, 104, 105, 106, 107] (2.455)	6.708-6.712[103, 104, 105, 106, 107]	104±10[103, 104, 105, 106, 107], 2.401±0.231	3.16[108, 109, 66] (3.20[9], 3.27[10])	12.29[108, 66], 12.30[109]	140±22[10], 3.239±0.498

underestimates it by 4.2%. However, both methods result overestimate E_i by 14% relative to experimental value. Interestingly, LDA yield almost the experimental value of c , even if it underestimates the experimental E_i by 8%.

An analysis made for 2H- MoS_2 reveals similar trends and indicates vdW interaction as the dominant interaction between its layers. While interlayer interaction calculated with GGA is only 6 meV per MoS_2 unit, c is badly overestimated to be 15.54 Å. This is 26,4 % longer relative to experimental value of lattice constant c measured[108, 109, 66] to be $c = 12.29 - 12.30$ Å. While GGA optimizes lateral lattice constants at $|a| = |b| = 3.215$ Å, the measured lateral lattice constants $|a| = |b| = 3.16$ Å.[108, 109, 66] In contrast, GGA+D and GGA+DF methods estimate E_i to be 160 meV and 176 meV, respectively. Accordingly, c values calculated by these vdW corrections are 12.41 Å (i.e. overestimated by 0.9 %) and 13.15 Å (overestimated by 7.0%), respectively. The lateral lattice constant a is optimized by GGA+D to be ~ 3.22 Å (3.258 Å by GGA+DF). On the other hand, LDA underestimates both a and c by $\sim 2\%$ relative to experimental value and predicts $E_i=110$ meV. In view of this analysis and comparison with measured[108, 109, 66] lattice constants, GGA+D method appears to be suitable to obtain optimized structure and related properties of 2H- MoS_2 and 1H- MoS_2 . For the rest of this section, we will use results obtained from this method unless it is stated otherwise.

Two dimensional 1H- MoS_2 can maintain its physical properties, when its size is large. However a small flake or a ribbon can display rather different electronic and magnetic properties. In particular, edge atoms may influence the physical

properties. The passivation of edge atoms by hydrogen atoms also result in significant changes in the properties of the nanoribbons. In this respect, one expects that the armchair (A- MoS_2NR) or zigzag (Z- MoS_2NR) nanoribbons of 1H- MoS_2 can display even more interesting electronic and magnetic properties.

We consider bare, as well as hydrogen saturated armchair and zigzag nanoribbons. These nanoribbons are specified by their width w in \AA or n number of Mo-S₂ basis in the unit cell. We take armchair nanoribbon with $n=12$ and zigzag nanoribbons with $n=6$ as prototypes. The distance between Mo and S atom, $d_{\text{Mo-S}}$ varies depending on the position in the ribbon. For example for $n=12$, while at the center of the armchair nanoribbon, $d_{\text{Mo-S}}=2.44 \text{ \AA}$, and $d_{\text{S-S}}=3.15 \text{ \AA}$, at the edge of the armchair nanoribbons, they change to $d_{\text{Mo-S}}=2.56 \text{ \AA}$ and $d_{\text{S-S}}=3.27 \text{ \AA}$. The lattice parameters at the center of ribbons attain the same values as 1H- MoS_2 . The average binding energy of hydrogen atoms passivating Mo and S atoms at the edges of the nanoribbon is $E_b=3.64 \text{ eV}$. The lengths of Mo-H and S-H bonds are 1.70 \AA and 1.36 \AA , respectively. The distance between S atoms at the edge is calculated as 3.27 \AA upon hydrogen passivation.

3.3 Stability of MoS_2

Previously, the lattice dynamics of 2H- MoS_2 has been investigated both experimentally and theoretically. The phonon dispersion curves and density of states have been obtained by fitting the force constants to experimental data.[2, 81] Meanwhile 2D sheets of MoS_2 including the single layer 1H- MoS_2 were synthesized.[75, 79, 76, 77] Our objective is (i) to calculate phonon dispersion curves and total density of states of both 2H- MoS_2 and 1H- MoS_2 from the first-principles including vdW correction; (ii) to reveal the dimensionality effects between 3D and 2D MoS_2 ; (iii) to provide understanding of phonon anomalies observed in Raman spectra[78, 3]; and (iv) to provide stability analysis of nanoribbons.

While Mo atoms in 2H- MoS_2 occupy sites of D_{3h} symmetry, S atoms obey

C_{3v} symmetry. The overall symmetry of the crystal is D_{6h} , having 24 symmetry elements and 12 irreducible representations. Four second order representations involve the lateral (in-plane) displacements of Mo and S atoms, as indicated in Fig. 3.2. First order representations are coupled with the displacements perpendicular to the layers of atoms or parallel to z -axis. Similar observations are also valid for monolayer 1H- MoS_2 having D_{3h} symmetry, 12 symmetry elements and 6 irreducible representations. In order for an irreducible representation to be Infrared active mode, it must create a dipole moment in the system. For 2H- MoS_2 , E_{1u} and A_{2u} modes are Infrared active. Similarly, E' and A_2'' modes are Infrared active modes of 1H- MoS_2 . Raman active modes induce polarization, or quadruple moment in the lattice. A_{1g} , E_{1g} and E_{2g} modes are Raman active modes for 2H- MoS_2 , so as A_1' , E' and E'' modes for 1H- MoS_2 .

Verble and Wieting[59, 60] related the interlayer interaction in 2H- MoS_2 with the splitting of the frequencies of E_{2g} and E_{1u} modes. In both modes the first layer atoms have similar displacements, but the displacements of the second layer atoms are in opposite direction as indicated in Fig. 3.2. Minute difference between the frequencies of E_{2g} and E_{1u} shows that the interlayer vdW interaction in 2H- MoS_2 is small. Wakabayashi *et al.*[2] first reported the phonon dispersion of 2H- MoS_2 by neutron scattering. Because of experimental limitations, they only reported 12 phonon branches along $\Gamma - M$ and $\Gamma - A$ direction out of 18 available ones. The error term in their experiments is $\pm 5\%$. Bertrand[80] reported that surface phonons have frequencies lower than those of bulk MoS_2 phonons. There is a softening of phonon modes upon going to the edges of nanocrystal 2H- MoS_2 . Recent experimental study by Livneh and Sterer[111] revealed the effect of pressure and temperature on the Raman active modes of 2H- MoS_2 . They reported that upon increasing the temperature of the system, the frequencies of Raman active modes decrease. Whereas the frequencies of Raman active modes increases with increasing pressure.

Phonon dispersion curves of 3D and 2D MoS_2 and their total densities of states calculated within DFPT[51] using structure optimized GGA+D are presented in Fig. 3.2. Specific experimental data and earlier calculations are also indicated for the sake of comparison. The phonon branches calculated from the first-principles

for 3D MoS_2 are in overall agreement with experimental data as well as with that calculated using valence force field method.[2]. The calculated acoustical and optical branches of 1H- MoS_2 , $\Omega(\mathbf{k})$ which are positive for any \mathbf{k} in BZ. This indicates that the suspended, single layer 1H- MoS_2 structure is stable.

Phonon dispersion curves and corresponding density of states for 2H- MoS_2 and 1H- MoS_2 are similar, except that the number of branches in the former are doubled. Owing to the weak vdW interaction some branches are slightly split. The difference between 2H- and 1H- MoS_2 is substantiated by the difference of total density of states, i.e $\Delta D(\Omega) = D_{3D}(\Omega) - 2D_{2D}(\Omega)$. The plot of $\Delta D(\Omega)$ in Fig. 3.2(e) indicates an overall shift of critical point frequencies of 3D MoS_2 to slightly higher values, while some modes show a reverse trend. The out of plane acoustical (ZA) mode of 1H- MoS_2 has parabolic dispersion, since the transverse forces decay exponentially. Also the LO-TO splitting is properly predicted. We also determined the Infrared (IR) and Raman (R) active modes at the Γ -point of BZ. Our results presented in Tab. 3.2.

Earlier, Raman [81, 59, 60, 65, 80, 112] and Infrared spectra [59, 60, 73] of 2H- MoS_2 were studied experimentally. Wieting and Verble[59, 60] reported three Raman active modes at 287, 383 and 409 cm^{-1} . On the other hand, Chen and Wang [112] have observed four Raman active modes in bulk at $E_{2g}^2=32 \text{ cm}^{-1}$, $E_{1g}=286 \text{ cm}^{-1}$, $E_{2g}^1=383 \text{ cm}^{-1}$ and $A_{1g}=408 \text{ cm}^{-1}$. The small E_{2g}^2 mode is not observed by Wieting and Verble[59, 60] because of the spectral limit of the Raman measurements between 20-1000 cm^{-1} . Also experimentally, at the zone center, IR active modes are observed at 384 cm^{-1} [59, 60, 73] and 470 cm^{-1} [59, 60] (468 cm^{-1} [73]). For the case of 1H- MoS_2 , Lee *et al.*[78] investigated the Raman spectra of 2D MoS_2 sheets as a function of thickness down to a single layer 1H- MoS_2 . They reported that the frequency of the Raman active A_{1g} mode of 2H- MoS_2 (i.e. thick sheet) decreases gradually from 408 cm^{-1} to $\sim 403 \text{ cm}^{-1}$ corresponding to the frequency of A_1' of 1H- MoS_2 indicating the phonon softening. As for the Raman active mode of 1H- MoS_2 E' displays a reverse behavior and hence its frequency decreases from 383.4 cm^{-1} to 382 cm^{-1} corresponding to the frequency of E_{2g} mode of 2H- MoS_2 . Even if the lateral displacements of atoms in E_{2g} mode are not affected significantly, one nevertheless expects that all modes of

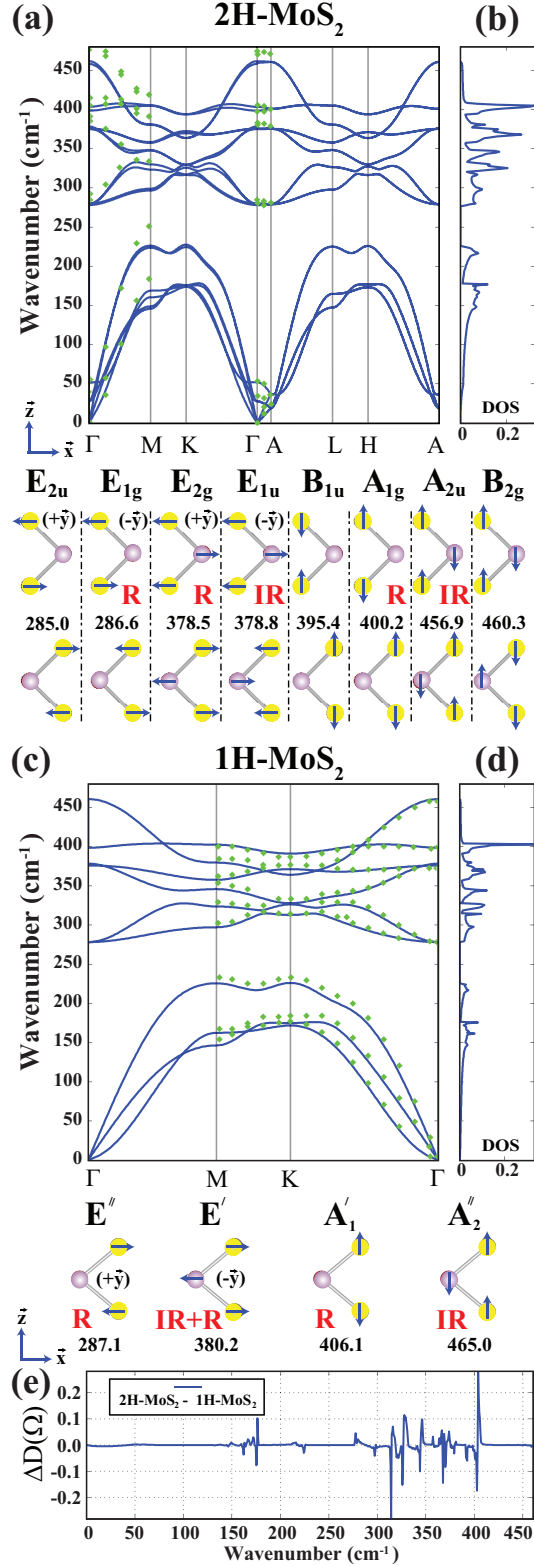


Figure 3.2: (a) Calculated phonon dispersion curves of 2H- MoS_2 , $\Omega(\mathbf{k})$ versus \mathbf{k} along symmetry directions of BZ and corresponding density of states (b). (c) and (d) are the same as (a) and (b) for 1H- MoS_2 . (e) Difference of the densities of states of 2H- MoS_2 and 1H- MoS_2 (see text). Phonon branches derived from neutron scattering data[2] and branches calculated by using a local basis set[3, 4] are indicated in (a) and (c) by green (light) squares, respectively. Infrared (IR) and Raman (R) active modes with symmetry representations and frequencies (cm^{-1}) at the Γ -point are indicated. Taken from Ataca *et al.*[1]

Table 3.2: Calculated frequencies of Raman (R) and Infrared (IR) active modes (in cm^{-1}) of 2H- and 1H- MoS_2 at the Γ -point and their symmetry analysis. The subscript u and g represent antisymmetric and symmetric vibrations, respectively. The other subscript i ($i = 1, 2, 3$) indicates the stretching modes. IR and R frequencies of 2H- and 1H- MoS_2 are calculated for the fully optimized lattice constants and internal structural parameters. Entries of IR and R frequencies of 2H- and 1H- MoS_2 indicated by (*) are calculated using the experimental lattice constants a and c of 2H- MoS_2 , but optimizing other internal structural parameters. The entry with (**) is calculated with $a=3.14 \text{ \AA}$ and corresponds to a , which is smaller than the experimental lattice constant a of 2H- MoS_2 . Taken from Ataca *et al.*[1]

2H- MoS_2	Lattice Symmetry: $D_{6h} = D_6 \times i$		
	# of Symmetry Elements: 24		# of Irreducible Representations: 12
	Atom	Wyckoff position	phonon modes
	Mo	2c	$2 A_{2u} + 2 B_{2g} + 2 E_{2g} + 2 E_{1u}$
	S	4f	$A_{1g} + 2 A_{2u} + 2 B_{2g} + B_{1u} + 2 E_{1u} + 2 E_{2g} + E_{2u} + E_{1g}$
	Raman= $A_{1g} + 2 E_{2g} + E_{1g}$ IR= $2 A_{2u} + 2 E_{1u}$		
	Lattice Constants	IR (cm^{-1})	Raman (cm^{-1})
	$a = 3.220 \text{ \AA}; c = 12.411 \text{ \AA}$	$A_{2u}(456.9); E_{1u}(378.8)$	$A_{1g}(400.2), E_{2g}(378.5); E_{1g}(286.6)$
	(*) $a = 3.160 \text{ \AA}; c = 12.300 \text{ \AA}$	$A_{2u}(467.6); E_{1u}(381.6)$	$A_{1g}(407.7), E_{2g}(381.3); E_{1g}(277.8)$
1H- MoS_2	Lattice Symmetry: $D_{3h} = D_3 \times i$		
	# of Symmetry Elements: 12		# of Irreducible Representations: 6
	Atom	Wyckoff position	phonon modes
	Mo	1a	$2 A_2'' + 2 E'$
	S	2e	$A_1' + 2 A_2'' + 2 E' + 2 E''$
	Raman= $2 E' + E'' + A_1'$ IR= $2 E' + 2 A_2''$		
	Lattice Constants	IR (cm^{-1})	Raman (cm^{-1})
	$a = 3.221 \text{ \AA}$	$A_2''(465.0); E'(380.2)$	$A_1'(406.1); E'(380.2), E''(287.1)$
	(*) $a = 3.160 \text{ \AA}$	$A_2''(468.0); E'(381.2)$	$A_1'(397.8); E'(381.2), E''(274.5)$
	(**) $a = 3.140 \text{ \AA}$	$A_2''(467.5); E'(385.0)$	$A_1'(392.7); E'(385.0), E''(279.9)$

3D bulk MoS_2 slightly soften in single layer MoS_2 due to the absence of interlayer interaction. The observation by Lee *et al.*[78] was surprising. In fact, recent study by Ramakrishna *et al.*[3] ended up with a different trend; they observed that both A_{1g} and E'_{2g} modes of 2H- MoS_2 sheets become softer as their thickness decreases.

We attempted to clarify the controversial results reported for the above crucial dimensionality effect. To this end, we calculated the frequencies of Raman active modes of 2H- MoS_2 and 1H- MoS_2 and compared our results with available experimental data.[59, 60, 73, 78, 3] Present GGA+D calculations predict Raman active modes $E_{1g}=286.6 \text{ cm}^{-1}$, $E_{2g}^1=378.5 \text{ cm}^{-1}$ and $A_{1g}=400.2 \text{ cm}^{-1}$ using the optimized lattice constants of $a=3.22 \text{ \AA}$ and $c=12.41 \text{ \AA}$. The optimized lattice constant of 1H- MoS_2 did not alter from the optimized value of 3D bulk despite the absence of interlayer interaction. Using the optimized lateral lattice constant $a=3.22 \text{ \AA}$, we obtained the frequencies of the Raman active modes as $E'=380.2 \text{ cm}^{-1}$ and $A'_1=406.1 \text{ cm}^{-1}$. (See Table 3.2) According to these results of ab-initio GGA+D method, the frequencies of both modes should increase as one goes from 3D to 2D single layer, which disagree with experimental results, except the behavior of $E_{2g} \rightarrow E'$ reported by Lee *et al.*[78]

The source of this disagreement between ab-initio calculations and experimental data is sought in the lattice constants, which are overestimated by GGA+D calculations. We repeated the same GGA+D calculations using experimental lattice constants,[108, 109, 66] namely $a=3.16 \text{ \AA}$ and $c=12.30 \text{ \AA}$ for 2H- MoS_2 and $a=3.16 \text{ \AA}$ for 1H- MoS_2 by assuming that the lateral lattice constant, a , did not change by going from 3D to single layer. We find that $A_{1g}=407.7$, $E_{2g}=381.3 \text{ cm}^{-1}$ and $E_{1g}=277.8 \text{ cm}^{-1}$ for 2H- MoS_2 , while for 1H- MoS_2 $A'_1=397.8 \text{ cm}^{-1}$, $E'=381.2 \text{ cm}^{-1}$ and $E''=274.5$. Apparently, Raman active modes of 2H- MoS_2 calculated with experimental lattice constants are in good agreement with observed Raman frequencies.[59, 112] Moreover, we are able to reproduce the experimental trend that frequency of the Raman active mode A_{1g} softens for $A_{1g} \rightarrow A'$, i.e. as the dimensionality is reduced from 3D to 2D. The change in the frequency is negligibly small for $E_{2g} \rightarrow E'$. Noting the fact that the lattice constant of graphene, a , gets slightly smaller than that of 3D graphite, despite GGA+D optimizes a of

3D and 2D almost at the same value. Considering the possibility that the lattice constant of 1H- MoS_2 a can get smaller than the lateral lattice constant of 3D MoS_2 $a=3.16 \text{ \AA}$, we repeated our calculations for 1H- MoS_2 using $a=3.14 \text{ \AA}$ and found that the frequency of E' increases from 381.2 cm^{-1} to 385 cm^{-1} confirming the anomalous effect reported by Lee *et al.* (See Table 3.2). This is, however, a hypothetical situation and will be clarified when an experimental data on the lattice constant a of freestanding 1H- MoS_2 will be available. We also note that Raman active modes of 2H- MoS_2 calculated by LDA, which underestimates the lattice constants was able to reproduce the same dimensionality effect between 3D and 2D MoS_2 as reported by Lee *et al.*[78], namely that while A' softens, E' becomes harder by going from 3D to 2D. To address the question, whether the Raman active modes of the slabs of 2D MoS_2 comply with the above trends, we calculated the frequencies of two layer and three layer MoS_2 using the experimental value of lattice constant, a of 2H- MoS_2 . Since there is no data available for the spacings of layers in slabs, we used again the experimental lattice constant c of 2H- MoS_2 and set the spacings equal to $c/2$. We found that A'_1 increases with increasing number of layers (namely $A'_1 \rightarrow 404.9 \text{ cm}^{-1}$ for bilayer MoS_2 and $A'_1 \rightarrow 405.9 \text{ cm}^{-1}$ for three layer MoS_2 , and approaches to A'_1 of 2H- MoS_2 . Nevertheless, the absence of experimental data on the structure of bilayer and three layer MoS_2 slabs prevents us to draw more definite conclusions regarding phonon softening or phonon hardening with dimensionality.

In Table 3.2 we present the frequencies of the IR active modes calculated using optimized as well as experimental lattice constants. For 2H- MoS_2 , the present GGA+D calculations using experimental lattice constants can give values in good agreement with experimental data, namely $A_{2u}=467.6 \text{ cm}^{-1}$ (as compared to experimental value of 468 cm^{-1}) and $E_{1u}=381.6 \text{ cm}^{-1}$ (as compared to experimental value of 384 cm^{-1}).[59, 73]

Born effective charges and interlayer and intralayer dielectric constants can be obtained from phonon calculations. Sun *et al.*[73] obtained high frequency dielectric constants, ϵ and Born effective charge, Z_B^* , of 2H- MoS_2 by fitting to the experimental data. They found Born effective charges, $Z_B^*[\text{Mo}]=1.11$ electrons (positive charge) for Mo and $Z_B^*[\text{S}]=-0.52$ electrons (negative charge) for

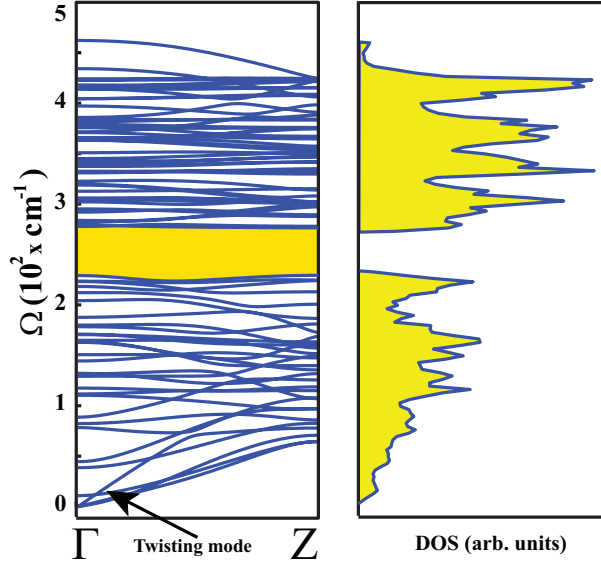


Figure 3.3: Calculated phonon frequencies, $\Omega(\mathbf{k})$ of the bare armchair MoS₂ nanoribbon with $w = 17.75 \text{ \AA}$ or $n = 12$ (there are 36 atoms in the primitive cell) are presented along symmetry directions of the Brillouin zone using Small Displacement Method (SDM), and corresponding densities of states (DOS). Taken from Ataca *et al.*[5]

each S atom and dielectric constants $\epsilon_{\parallel} = 15.2$ and $\epsilon_{\perp} = 6.2$ in the intralayer and interlayer directions, respectively. Here we calculate Born effective charges and high frequency dielectric constant of 2H-MoS₂ to be $Z_B^*[Mo] = 1.23$ electrons and $Z_B^*[S] = -0.57$ electrons.[113] High frequency dielectric constants are calculated to be, $\epsilon_{\parallel} = 15.60$ and $\epsilon_{\perp} = 6.34$ in the intralayer and interlayer directions, respectively. The values calculated from the first-principles are in good agreement with those determined by Sun *et al.*[73] from experimental data. As for 1H-MoS₂, Born effective charges are calculated to be $Z_B^*[Mo] = 1.21$ electrons for Mo and $Z_B^*[S] = -0.57$ electrons for S. These values are close to those of 2H-MoS₂. However, high frequency dielectric constants of 1H-MoS₂, which differ dramatically from 3D MoS₂ due to dimensionality effect, are $\epsilon_{\parallel} = 4.58$ and $\epsilon_{\perp} = 1.26$ in the intralayer and interlayer directions, respectively.

For the stability analysis of MoS₂ nanoribbons, we carried out a rigorous test through phonon calculations in addition to structure optimization through energy minimization. If the calculated frequencies of specific phonon modes are

imaginary, the structure becomes unstable for the corresponding \mathbf{k} -wave vectors in the BZ. Here we present an example for the stability test of nanoribbons, whereby we calculate the phonon frequencies of the bare armchair nanoribbon with $n=12$. The calculated phonon branches and corresponding density of states (DOS) are presented in Fig. 3.3. The out of plane (ZA) branch with parabolic dispersion and fourth acoustic branch (or twisting mode[114]) characteristics of nanoribbons are obtained. Earlier, the branch of twisting mode was revealed in MoS_2 nanotubes.[115] Similar twisting modes are also calculated for ZnO nanoribbons.[116] The overall shape of DOS of nanoribbons are similar to that of 2D MoS_2 sheets[78], except that the gap between optical and acoustical branches is reduced due to edge phonon states. For the same reason additional peaks occur for flat phonon branches of edge modes in band continua. All modes having positive frequency indicate that the bare armchair nanoribbon of MoS_2 with $n=12$ is stable. It is also expected that other bare nanoribbons having $n > 12$ are stable.

3.4 Mechanical Properties of MoS_2

The cohesive energy per MoS_2 unit relative to the free Mo and S atoms, $E_C = -E_T[\text{Crystal}] + E_T[\text{Mo}] + 2E_T[\text{S}]$, is calculated from the structure optimized total energies of the 3D crystal, $E_T[2\text{H} - \text{MoS}_2]/2$ or 2D crystal $E_T[1\text{H} - \text{MoS}_2]$ and the free atom total energies of Mo and S, $E_T[\text{Mo}]$ and $E_T[\text{S}]$, respectively. The calculated values of E_C for 2H- MoS_2 and 1H- MoS_2 are 15.316 eV and 15.156 eV per MoS_2 unit, respectively. Their difference is exactly the interlayer interaction energy of 3D MoS_2 , which was calculated to be 160 meV. This indicates that the cohesion of the layers in 2H- MoS_2 is the same as the cohesion of 1H- MoS_2 . In addition to cohesive energy, the zero pressure bulk modulus B_0 , is an important mechanical property of 3D crystals. Here we calculated the bulk modulus of 2H- MoS_2 by fitting the Murnaghan equation [117] as 44 GPa. The experimental value[118] is given as 43 GPa. Using van der Waals included DFT Rydberg *et al.*[67] calculated B_0 as 39 GPa. Our value calculated for the bulk modulus of B_0 is in good agreement with the experimental value.

Single layer, 1H- MoS_2 has high planar strength, but transversal flexibility. While Young's modulus normally characterizes the mechanical strength of bulk materials, owing to the ambiguities in defining the Young's modulus for the 2D honeycomb structure one can use in-plane stiffness $C = (1/A_0) \cdot (\partial^2 E_S / \partial \epsilon_s^2)$ in terms of the equilibrium area of the 2D cell, A_0 . [119, 120] We focused our attention on the harmonic range of the elastic deformation, where the structure responded to strain ϵ linearly. Here ϵ_s is the elongation per unit length. The strain energy is defined as $E_S = E_T(\epsilon_s) - E_T(\epsilon_s = 0)$; namely, the total energy at a given strain ϵ_s minus the total energy at zero strain. The calculated in-plane stiffness of 1H- MoS_2 is 145.82 N/m. This value can be compared with the experimental value of graphene, i.e. 340 ± 50 N/m. [121]

Currently, the behavior of honeycomb structures under tension has been a subject of current interest. [122, 123, 124, 125, 126, 127] While 1H- MoS_2 have honeycomb structure, its atomic configuration and bonding of atoms are dramatically different from graphene. Therefore, the response of A- and Z- MoS_2 NRs to the strain is expected to be different from graphene. The elastic properties of the quasi 1D MoS_2 nanoribbons are examined through the variation of the total energy with applied strain. Generally, nanoribbons change their electronic and magnetic properties under uniaxial tension in the elastic deformation range. Here we present the response of A- MoS_2 NR and Z- MoS_2 NR to the strain in elastic range.

Nanomechanics of both bare A- MoS_2 NR with $n=12$ and Z- MoS_2 NR with $n=6$ is explored by calculating the mechanical properties as a response to the strain along the axis of the ribbon. To allow more variational freedom and reconstruction, segments of these NRs are treated within supercell geometry using periodic boundary conditions and spin-polarized calculations are carried out. Each supercell, both having total of 108 atoms, contains three unit cells for armchair and six unit cells for zigzag nanoribbons, respectively. The stretching of the ribbon is achieved by increasing the equilibrium lattice constant c_0 by Δc , to attain the axial strain $\epsilon = \Delta c / c_0$. We optimized the atomic structure at each increment of the strain, $\Delta \epsilon = 0.01$ and calculated the total energy under strain $E_T(\epsilon)$. Then the strain energy can be given by, $E_S = E_T(\epsilon) - E_T(\epsilon = 0)$; namely, the total

energy at a given strain ϵ minus the total energy at zero strain. The tension force, $F_T = -\partial E_S(\epsilon)/\partial c$ and the force constant $\kappa = \partial^2 E_S/\partial c^2$ are obtained from the strain energy. The in-plane stiffness can be deduced from κ by defining an effective width for the ribbon.

For both A- and Z- MoS_2 NR the hexagonal symmetry is disturbed, but overall honeycomb like structure is maintained in the elastic range. However, stretched ribbons can return to its original geometry when the tension is released. In the harmonic range the force constant is calculated to be $\kappa = 116.39$ N/m and 92.38 N/m for A- MoS_2 having $n = 12$ and Z- MoS_2 NR having $n = 6$, respectively. Similarly, the calculated in-plane stiffness for the same ribbons are $C = 108.47$ N/m and 103.71 N/m, respectively. The difference between the values of armchair and zigzag nanoribbon occurs due to different bond and edge directions. As the width of the nanoribbon goes to infinity these two values are expected to converge to a single value. It should be noted that κ is approximately proportional to n , but C is independent of n for large n . Small deviations arise from the edge effects.

For applied strains in the plastic deformation range the atomic structure of the ribbon undergoes irreversible structural changes, whereby uniform honeycomb structure is destroyed. At the first yielding point the strain energy drops suddenly, where the ribbons undergo an irreversible structural transformation. Beyond the yielding point the ribbons are recovered and started to deform elastically until next yielding. Thus, variation of the total energy and atomic structure with stretching of nanoribbons exhibit sequential elastic and yielding stages.

3.5 Electronic and Magnetic Properties

3.5.1 2H- MoS_2 and 1H- MoS_2

In Figure 3.4 (a) we schematically illustrate the hexagonal crystal lattice, resulting in a honeycomb structure. The contour plots of total charge density, $\rho(\mathbf{r}) = \sum^{occ} |\Psi(\mathbf{k}, \mathbf{r})|^2$, and difference charge density isosurfaces, $\Delta\rho(\mathbf{r})$ (which is

obtained by subtracting the free atom charge densities of Mo and S atoms from the total charge density of 1H- MoS_2) are also shown in Fig. 3.4 (b) and (c), respectively. There are ambiguities in determining the charge transfer; calculated excess charges may depend on the method used. While different methods result in different values for charge transfer (or excess charge on the atoms), its direction can be predicted unambiguously. Based on Mulliken[128, 129] analysis the excess charge on each S atom and depletion of electrons on each Mo atom is calculated to be 0.205 electrons and 0.410 electrons, respectively. (For 2H- MoS_2 0.215 electrons and 0.430 electrons, respectively.) Electronic charge transferred from Mo to S atoms gives rise to an excess charge around S atoms. Consequently, 1H- MoS_2 can be viewed as a positively charged Mo planes sandwiched between two negatively charged planes of S atoms as presented in Fig. 3.4 (c). We note the direction of calculated charge transfer is in compliance with the Pauling's electronegativity scale,[129] as well as Born effective charges. The repulsive Coulomb force between negatively charged S atoms facing each other in adjacent MoS_2 layers weakens the interlayer interaction in two individual 1H- MoS_2 (or bilayer of MoS_2), as well as in graphitic 2H- MoS_2 .

Electronic structure of 2D suspended single layer 1H- MoS_2 and corresponding total (TDOS) and projected (PDOS) density of states calculated within GGA+PAW are presented in Fig. 3.4 (d) and (e). The states at the band edges, as well as at lower lying conduction and higher lying valence bands originate from the hybridization of Mo-4*d* and S-3*p* orbitals. The direct band gap is $E_g=1.58$ eV. The band gap calculated within LDA+PAW is $E_g=1.87$ eV, which is in good agreement with the band gap measured using complementary techniques of optical absorption, photoluminescence and photoconductivity as 1.90 eV.[77] Earlier Bollinger *et al.*[85] predicted the band gap to be 1.64 eV using GGA+ultrasoft pseudopotential. However, Li and Galli[130] with similar computational method calculated the band gap as 1.80 eV. Li *et al.*[83] calculated the direct band gap 1.69 eV within GGA+PAW using relatively smaller energy cut-off. Mendez *et al.*[72] found the direct band gap within LDA as $E_g=1.8$ eV using local basis set.[4]

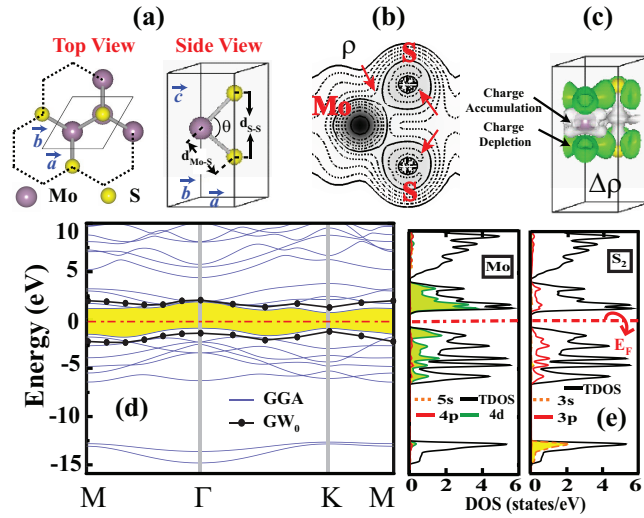


Figure 3.4: (a) Top and side views of atomic structure of 2D 1H-MoS₂ with hexagonal lattice. The hexagonal unit cell with lattice constants $|a| = |b|$ is delineated by thin solid lines. Honeycomb structure consisting of Mo and S₂ atoms located at the corners is highlighted by dotted hexagons. (b) Contour plots of charge density, ρ (see text for definition) in a vertical plane passing through Mo-S bonds. Arrows indicate the increasing value of charge density. (c) Isosurface plot of difference charge density, $\Delta\rho$ (see text for definition). Isosurface value is taken as 0.006 electrons/ \AA^3 . (d) Energy band structure of 1H-MoS₂ calculated by GGA+PAW using optimized structure. Zero of energy is set to the Fermi level indicated by dash-dotted line. The gap between valence and conduction band is shaded; GW₀ corrected valence and conduction bands are shown by filled circles. (e) Total density of states (TDOS) and orbital projected density of states (PDOS) for Mo and S. Taken from Ataca *et al.*[6]

Lebegue and Eriksson[84] carried out LDA+PAW calculations using experimental lattice constants and found the band gap to be 1.78 eV. The band gap calculated in the present work is in fair agreement with previous studies.[85, 83, 72] However, we show that band gaps determined in earlier studies increase ~ 1 eV upon GW_0 correction. The band gap calculated within GGA(LDA)+PAW is corrected using self-energy method GW_0 to be 2.50(2.57) eV. The corrected band gap is ~ 0.6 - 0.7 eV larger than the value measured experimentally.[77] The situation with graphitic MoS_2 , which consists of the stacking of 1H- MoS_2 layers is, however, different. The indirect band gap of graphitic MoS_2 calculated within GGA(LDA)+PAW is 0.85(0.72) eV and is corrected to be 1.44 (1.28) eV. In particular LDA+PAW band gap corrected by GW_0 is in good agreement with the experimental value.[131] Since LDA/GGA is designed to describe systems with slowly varying electron density and may fail to model localized d -orbitals,[132] more accurate band gap calculations can be carried out using generalized Kohn-Sham scheme, screened nonlocal exchange functional, HSE.[133] Starting from nonlocal charge density and wavefunctions, we calculated HSE and G_0W_0 [132] corrected electronic band structure of MoS_2 as a direct band gap of 2.23 and 2.78 eV, respectively. Surprisingly, the band gap of 2D 1H- MoS_2 is overestimated by GW_0 correction. The photoelectric threshold of 1H- MoS_2 is calculated as 5.96 eV.

Finally, we emphasize two important dimensionality effects related with the electronic structure of MoS_2 , which have important consequences like photoluminescence: (i) By going from graphitic MoS_2 to single layer 1H- MoS_2 the energy band gap changes from indirect to direct. (ii) The minimum gap increases by ~ 0.6 eV. The transformation from indirect to direct gap is related with the orbital composition of states at the edges of conduction and valence bands.[134, 130] The widening of the band gap in 2D occurs due to the absence of S - p_z orbital interaction between adjacent MoS_2 layers and appears as the manifestation of the quantum confinement in the direction perpendicular to the MoS_2 layer.[77]

3.5.2 Armchair and Zigzag Nanoribbons of MoS_2

Similar to the single layer 1H- MoS_2 , its armchair nanoribbons (A- MoS_2NR) are also semiconductors. The bare A- MoS_2NR is a nonmagnetic, direct band gap semiconductor. Upon hydrogen termination of the edges, the band gap increases. Also the direct band gap shows variation with n , like the family behavior of graphene nanoribbons. However, unlike armchair graphene nanoribbons[135], the band gaps of A- MoS_2NR 's do not vary significantly with its width w or n . For narrow armchair nanoribbons with $n < 7$ the calculated value of the band gap is larger than that of wide nanoribbons due to quantum confinement effect. The variation of E_g with n is in agreement with that calculated by Li *et al.*[83]

The electronic band structure and charge density of specific states are examined in detail for a bare A- MoS_2NR of $n=12$ in Fig. 3.5(a). The edge states, which are driven from Mo-4*d* and S-3*p* orbitals and have their charge localized at the edges of the nanoribbon form flat bands located in the large band gap of 1H- MoS_2 . Because of these edge states, the band gaps of bare armchair nanoribbons are smaller than that of 1H- MoS_2 . Upon termination of each Mo atom at the edge by two hydrogen and each S atom by a single hydrogen atom, the part of edge states are discarded and thus the band gap slightly increases. As seen in Fig. 3.5 (b), the remaining edge states continue to determine the band gap of the ribbon. Even if the character of these bands change, their charges continue to be located near the edge of the ribbon. Nevertheless, the band gaps of hydrogen saturated armchair nanoribbons remain to be smaller than that of 2D 1H- MoS_2 .

Furthermore we investigated the variation of band gap of hydrogen saturated armchair nanoribbons as a function of n . For $n \leq 7$ the values of band gap are larger due to quantum confinement effect, but for $n \geq 7$ they tend to oscillate showing a family like behavior. These oscillations follow those found for bare armchair nanoribbon.[83] All calculated A- MoS_2NR are found to be direct band gap semiconductors.

In contrast to A- MoS_2NR , the bare zigzag nanoribbons Z- MoS_2NR are spin-polarized metals. Here we consider Z- MoS_2NR with $n=6$ as a prototype. In

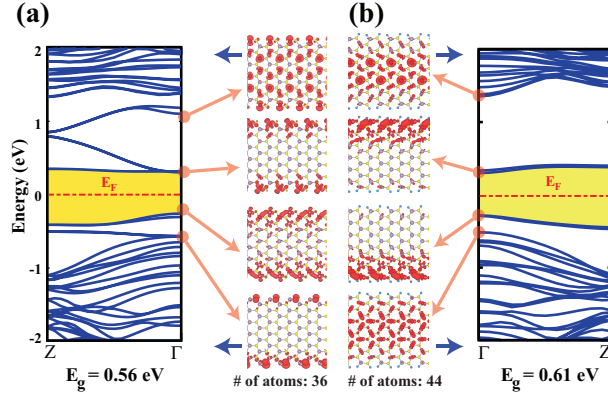


Figure 3.5: (a) Energy band structure of bare A- MoS_2NR having $n=12$ and the width $w=17.75 \text{ \AA}$. The band gap is shaded and the zero of energy is set at the Fermi level. At the right-hand side, charge density isosurfaces of specific states at the conduction and valence band edges are shown. (b) Same as (a), but the edge atoms are saturated by H atoms as described in the text. Large (purple), medium (yellow) and small (blue) balls are Mo, S, and H atoms, respectively. Short and dark arrows indicate the direction of the axes of nanoribbons. Total number of atoms in the unit cells are indicated. Taken from Ataca *et al.*[5]

Fig. 3.6, it is shown that the edge atoms of this nanoribbon undergo a (2×1) reconstruction by lowering its total energy by 0.75 eV . Interestingly, as a result of reconstruction, the bare Z- MoS_2NR is a half-metal with integer magnetic moment per primitive cell, namely $\mu=2 \mu_B$. Thus the nanoribbon is metallic for majority (spin-up) bands, but a semiconductor for minority (spin-down) bands with an indirect band gap of $\sim 0.50 \text{ eV}$. We check that half-metallic state of bare Z- MoS_2NR 's is maintained for $n=5$, and $n=8$. The half-metallic property is destroyed upon the saturation of the edge atoms by hydrogen. The magnetic moment of the ribbon and the density of spin states at the Fermi level depend on how Mo and S atoms at the edges of the ribbon are passivated by hydrogen. One distinguishes three different hydrogen passivations, each leads to different magnetic moments as indicated in Fig. 3.6. As the number of passivating hydrogen atoms increases the number of bands crossing the Fermi level decreases. However the spin-polarization is relatively higher, if each S atoms at one edge are passivated by single hydrogen atom and each Mo atom at the other edge is passivated by double hydrogen. Interestingly, the latter nanoribbon in Fig. 3.6(d) is metallic for one spin direction and semimetal for the opposite spin direction.

Different spin polarizations found for different spin directions can make potential nanostructure for applications in spintronics.

Earlier Li *et al.*[83] examined electronic and magnetic properties of armchair and zigzag MoS_2 nanoribbons using VASP[49, 50] within DFT. They found that armchair nanoribbons are nonmagnetic semiconductors and their direct energy band gap vary with n and becomes 0.56 eV as $n \rightarrow \infty$. They did not consider hydrogen passivation of edge atoms. They also noted that the value of net magnetic moment can change, but the ferromagnetic state of zigzag nanoribbons are maintained even after H passivation of edge atoms. Mendez *et al.*[72] investigated armchair nanoribbons and concluded that these nanoribbons are metallic and have a net magnetic moment, but they change to semiconductor after hydrogen passivation of edge atoms. Their calculations show that in the case of bare armchair nanoribbons, the magnetic state is energetically more favorable by 14 meV and for H-saturated zigzag nanoribbons the antiferromagnetic state is favorable relative to the ferromagnetic state by 15 meV. These results disagree the present results, as well as with those of Li *et al.*[83]

Normally, the bare and unreconstructed zigzag nanoribbons have sizable electric dipole moment along the direction from the edge having only negatively charged S atoms to the other edge having only positively charged Mo atoms. The dipole moment is calculated to be 55.4 eÅ per cell of Z- MoS_2 NR having $n = 6$, but it reduces to 0.07 Å upon reconstruction of the edges. Present results show that the edge reconstruction ought to be treated properly to reveal the half-metallic state and to estimate the correct dipole moment.

3.6 Functionalization of MoS_2

There are numerous ways of functionalization a materials. In this section, we will focus on functionalization of both 1H- MoS_2 and MoS_2 nanoribbons by adatom adsorption and vacancy defect creation.

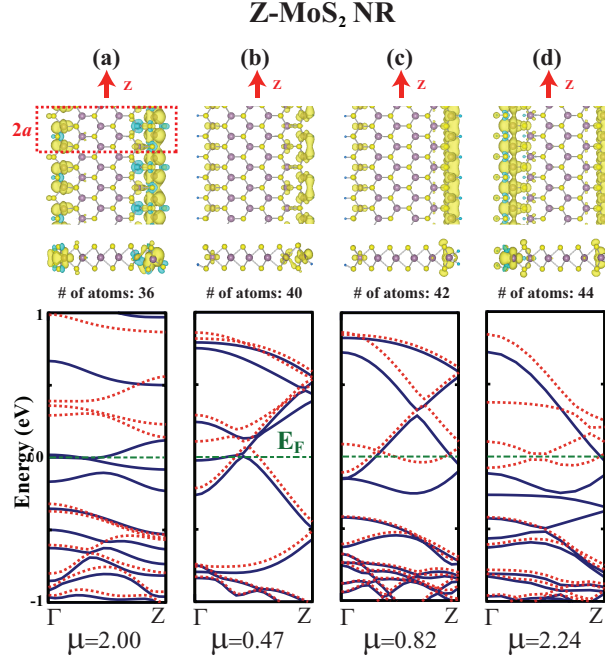


Figure 3.6: Atomic and energy band structure of bare and hydrogen saturated zigzag nanoribbon $\text{Z-MoS}_2\text{NR}$ having $n=6$ Mo-S_2 basis in the primitive unit cell. The top and side views of the atomic structure together with the difference of spin-up and spin-down charges, $\Delta\rho = \rho^\uparrow - \rho^\downarrow$, are shown by yellow/light and turquoise/dark isosurfaces, respectively. The isosurface value is taken to be 10^{-3} electrons per \AA^3 . The (2×1) unit cell with the lattice constant $2a$ is delineated. Large (purple), medium (yellow) and small (blue) balls are Mo, S, and H atoms, respectively. The zero of energy is set at the Fermi level shown by dash-dotted green/dark lines. Energy bands with solid (blue) and dashed (red) lines show spin-up and spin-down states, respectively. (a) The bare $\text{Z-MoS}_2\text{NR}$ having $\mu=2 \mu_B$ per cell displays half-metallic properties. (b) Spin-polarized ground state of $\text{Z-MoS}_2\text{NR}$ with Mo atoms at one edge and bottom S atoms at the other are passivated by single hydrogen. (c) Similar to (b), but Mo atoms are passivated by two hydrogen atoms. (d) Similar to (c), but top S atoms at the other edge are also passivated by single hydrogen atoms. The net magnetic moment of each case is indicated below the corresponding band panels. Bands are calculated using double cells. Small arrows along z -axis indicate the direction of the nanoribbon. The total number of atoms in supercell calculations are indicated for each case. Taken from Ataca *et al.*[5]

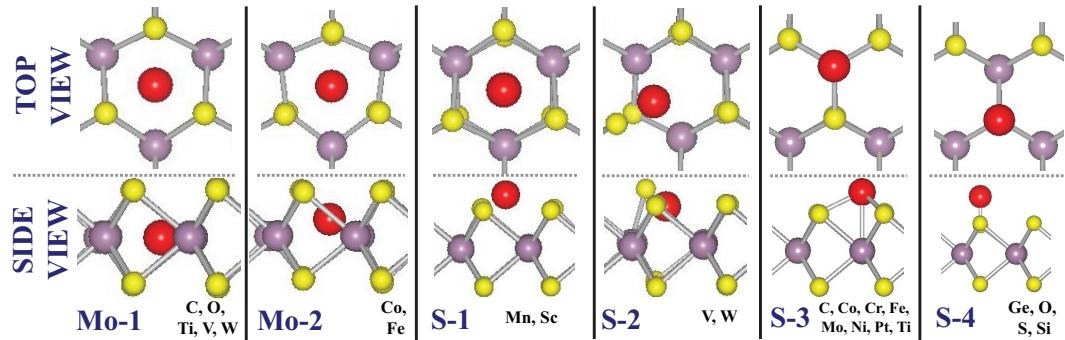


Figure 3.7: Top and side views are the schematic representation of possible adsorption geometries of adatoms obtained after the structure optimization. Adatoms, host Mo and S atoms are represented by red (large-dark), purple (medium-gray) and yellow (small-light) balls, respectively. Side views clarify the heights of adatoms from Mo and S atomic planes. Different adsorption sites are specified below each entry as 'Mo(S)-#', where Mo(S) indicates that adatoms are placed initially (before structure optimization) to Mo(S) plane. In Mo-1 and Mo-2 geometries the adatoms are in and slightly above the Mo-layer. S-1, S-2,... S-4 positions are associated with the S-layer. The adatoms adsorbed at each site are given at the lower right hand side of each entry. Taken from Ataca *et al.*[6]

3.6.1 Functionalization by Adatom Adsorption

Adsorption of adatoms is widely used and an efficient way to provide new functionalities to structures in nanoscale applications.[136, 137, 138, 7, 8, 135, 139] Among 16 different adatoms, namely, C, Co, Cr, Fe, Ge, Mn, Mo, Ni, O, Pt, S, Sc, Si, Ti, V and W, we were interested in 10 transition metal elements to determine ones which can induce magnetization in nonmagnetic 1H- MoS_2 . Group 4A elements, i.e. C, Si and Ge are considered, since these atoms can form stable, planar or buckled honeycomb structures.[140, 141, 56] Carbon was of particular interest for the fabrication of graphene+ MoS_2 complex or nanomeshes. Mo and S being host atoms in 1H- MoS_2 , they can exist as residues. Whether MoS_2 can be oxidized is an important issue, which may limit future applications. The first question one has to address is, of course, whether these adatoms can form strong and stable bonding with 1H- MoS_2 . The equilibrium adsorption sites of these 16 atoms are determined by first placing them to one of four different adsorption

sites and subsequently by optimizing whole structure. Four possible adsorption sites considered initially for each adatom before the structure optimization are: (i) Hollow site slightly above the center of hexagon at Mo atomic plane. (ii) Hollow site above the center of hexagon at S-plane. (iii) Top of Mo atom. (iv) Top of S atom. Here the bridge site above the Mo-S bond is very similar to adsorption of adatom at the top of Mo atom. In order to avoid adatom-adatom coupling, the (4x4) supercell of 1H- MoS_2 is used, where the nearest adatom-adatom distance is $\sim 12.8 \text{ \AA}$. Thus, the results can be related to the adsorption of an isolated adatom. The minimum energy positions of adatoms after the optimization process are described in Fig. 3.7. We note that C, Co, Fe, O, Ti, V and W have two different binding sites (one having higher binding energy, E_b); each site leading to dramatically different electronic and magnetic structure. Six distinct adsorption sites described in Fig. 3.7, namely Mo-1, Mo-2, S-1, S-2, S-3 and S-4 are distinguished after structure optimization.

All relevant data obtained from our calculations of adatoms adsorbed to 1H- MoS_2 are presented in Tab. 3.3. The height of the adatom from the Mo- or S-planes are calculated relative to the average heights of Mo- and S- atoms in the corresponding planes. The binding energy, E_b is calculated as $E_b = E_{ad} + E_{\text{MoS}_2} - E_{ad+\text{MoS}_2}$. Here, E_{ad} is the ground state energy of free adatom calculated in the same supercell with the same parameters; E_{MoS_2} is the total energy of (4x4) supercell of 1H- MoS_2 and $E_{ad+\text{MoS}_2}$ is the optimized total energy of adatom+(4x4) supercell of 1H- MoS_2 . Among different adatoms studied here, Cr has the weakest binding energy ($E_b = 1.08 \text{ eV}$); W has the strongest binding ($E_b = 4.93 \text{ eV}$) and creates a local reconstruction on S-layer. The excess charge[54] of the adatom ρ^* , is obtained by subtracting the calculated charge at the adatom, ρ_A from the valence charge of the adatom Z_A , namely $\rho^* = Z_A - \rho_A$. Accordingly $\rho^* < 0$ implies excess electron at the adatom site. The magnetic moments are obtained by carrying out spin-polarized calculations without assigning initial atomic magnetic moments on adatoms. Upon relaxation the final magnetic moment is obtained.

Since the adatom-adatom interaction is hindered by a large separation between them, the adatoms presented in Tab. 3.3 give rise to localized electronic states in the band gap and resonant states in band continua and hence modify

Table 3.3: Calculated values for the properties of 16 adatoms adsorbed on 1H- MoS_2 . For specific adatoms, the first and second lines are associated with the adsorption to the Mo-layer and S-layer site, respectively. Other adatoms have only positive binding energy when adsorbed to the S-layer site. The adsorption sites of adatoms are described in Fig. 3.7. h_{Mo} , the height of the adatom from Mo layer; h_{S} , the height of the adatom from the nearest S-layer; d_{Mo} , the adatom-nearest Mo distance; d_{S} , the adatom-nearest S distance; E_b , adatom binding energy; μ_T , magnetic moment per supercell in Bohr magneton μ_B ; ρ^* , excess charge on the adatom (where negative sign indicates excess electrons); Φ , photoelectric threshold (work function); P, dipole moment calculated in the direction normal to 1H- MoS_2 surface. E_i , energies of localized states induced by adatoms. Localized states are measured from the top of the valence bands in eV. The occupied ones are indicated by bold numerals and their spin alignments are denoted by either \uparrow or \downarrow . States without the arrow sign indicating of spin alignment are nonmagnetic. Taken from Ataca *et al.*[6]

Atom	Site	h_{Mo} (Å)	h_{S} (Å)	d_{Mo} (Å)	d_{S} (Å)	E_b (eV)	μ_T (μ_B)	ρ^* (e)	Φ (eV)	P ($e \times \text{Å}$)	E_i \uparrow : Spin-up, \downarrow : Spin-down States
C	Mo-1	-0.01	1.56	2.04	2.44	3.28	NM	-0.65	5.81	0.00	0.14 , 0.19 , 2.18, 4.85
	S-3	1.58	-0.05	2.07	1.80	2.69	2.00	-0.58	5.74	-0.10	0.26 \uparrow , 0.30 \downarrow , 1.07 \uparrow , 1.13 \uparrow , 1.55 \downarrow , 1.60 \downarrow
Co	Mo-2	0.61	0.99	2.22	2.19	0.96	1.00	0.15	5.57	-0.07	0.61 \uparrow , 0.66 \uparrow , 0.82 \downarrow , 0.87 \downarrow , 0.89 \uparrow , 1.13 \downarrow
	S-3	2.52	0.94	2.56	2.11	2.92	1.00	0.44	5.17	-0.38	0.29 \uparrow , 0.51 \uparrow , 0.57 \downarrow , 0.62 \uparrow , 0.99 \downarrow , 1.00 \downarrow
Cr	S-3	2.79	1.21	2.77	2.26	1.08	4.00	0.91	4.25	-0.75	0.19 \uparrow , 0.22 \uparrow , 0.59 \uparrow , 0.64 \uparrow , 0.68 \uparrow , 1.60 \downarrow , 1.73 \downarrow
Fe	Mo-2	0.31	1.29	2.21	2.26	0.39	2.00	0.34	5.07	-0.04	0.32 \uparrow , 0.48 \uparrow , 0.87 \uparrow , 1.01 \downarrow , 1.15 \downarrow , 1.32 \downarrow
	S-3	2.52	0.93	2.53	2.14	2.42	2.00	0.59	4.99	-0.46	-0.03 \uparrow , 0.18 \uparrow , 0.21 \uparrow , 0.22 \uparrow , 0.91 \downarrow , 0.93 \downarrow , 1.31 \downarrow
Ge	S-4	3.83	2.26	4.28	2.30	1.18	2.00	0.39	4.78	-0.27	1.10 \uparrow , 1.11 \uparrow , 1.72 \downarrow , 1.75 \downarrow
Mn	S-1	2.51	0.93	3.06	2.15	1.37	3.00	0.81	4.75	-0.44	0.16 \uparrow , 0.17 \uparrow , 0.49 \uparrow , 0.50 \uparrow , 1.30 \downarrow , 1.98 \downarrow , 2.05 \downarrow
Mo	S-3	2.89	1.31	2.84	2.30	1.43	4.00	0.81	4.54	-0.76	0.48 \uparrow , 0.79 \uparrow , 0.87 \uparrow , 0.91 \uparrow , 1.16 \downarrow , 1.42 \downarrow , 1.54 \downarrow
Ni	S-3	2.52	0.94	2.56	2.12	3.65	NM	0.36	5.58	-0.31	0.12 , 0.16 , 0.21 , 0.50 , 0.51 , 0.57
O	Mo-1	-0.01	1.57	1.95	2.56	2.24	NM	-1.11	5.72	0.00	-6.36 , -6.34 , -5.66 , 0.32
	S-4	2.94	1.38	3.51	1.49	3.99	NM	-0.91	5.96	0.35	-5.63 , -1.16 , -0.90
Pt	S-3	2.78	1.21	2.76	2.31	2.92	NM	0.08	5.66	-0.26	0.26 , 0.27 , 0.37 , 1.76
S	S-4	3.48	1.91	3.96	1.94	2.17	NM	-0.11	5.96	0.23	0.00 , 0.06 , 0.11
Sc	S-1	2.84	1.25	3.30	2.29	2.63	1.00	1.45	4.31	-1.18	1.28 \uparrow , 1.31 \uparrow , 1.35 \downarrow , 1.49 \downarrow , 2.25 \downarrow , 2.39 \uparrow
Si	S-4	3.73	2.16	4.18	2.17	1.39	2.00	0.58	4.94	-0.14	0.98 \uparrow , 0.99 \uparrow , 1.65 \downarrow , 1.68 \downarrow
Ti	Mo-1	0.00	1.58	2.31	2.42	1.23	NM	1.14	5.71	0.00	0.26 , 0.34 , 0.36 , 1.74, 1.77
	S-3	2.95	1.38	2.99	2.32	2.62	4.00	1.16	4.32	-1.12	1.18 \uparrow , 1.24 \uparrow , 1.35 \uparrow , 1.37 \uparrow , 1.54 \uparrow , 1.77 \downarrow , 1.81 \downarrow
V	Mo-1	0.03	1.55	2.95	2.34	1.25	1.00	1.05	4.61	0.00	0.12 \uparrow , 0.16 \downarrow , 0.17 \uparrow , 0.21 \downarrow , 1.54 \uparrow , 1.67 \uparrow , 1.69 \downarrow
	S-2	1.87	0.19	2.56	2.07	2.76	1.00	1.05	5.18	0.04	0.07 \uparrow , 0.18 \downarrow , 0.84 \uparrow , 1.23 \downarrow , 1.45 \uparrow , 1.54 \downarrow
W	Mo-1	0.01	1.58	2.41	2.42	1.18	2.00	1.05	4.66	0.01	0.16 \uparrow , 0.21 \downarrow , 1.41 \uparrow , 1.49 \uparrow , 1.61 \downarrow , 1.81 \downarrow
	S-2	1.87	0.16	2.61	2.15	4.93	NM	0.85	5.58	0.12	0.13 , 0.19 , 0.58 , 1.57, 1.75

the electronic properties of 1H- MoS_2 . In Fig. 3.8, localized states of O, Ti, Cr and Ge together with band decomposed charge density isosurfaces are presented. These atoms are specifically selected, since they are representatives of some of the adatoms presented Tab. 3.3. Oxygen adatom when placed on the S plane is adsorbed on top of S atom (S-4 site) with a binding energy of 3.99 eV. This site is in agreement with the results of He *et al.*[98] However, we predict also a local minimum at Mo-1 site with relatively smaller binding energy ($E_b = 2.44$ eV). Adsorbed O is nonmagnetic at both sites. Oxygen adatom having the highest electronegativity and highest negative excess charge among all other adatoms have localized states in the valence band. When O is adsorbed at Mo-1 site, the only localized state occurring in the band gap is filled and originate from the combination of O- p_z orbital with the p -orbitals of nearest S atoms. Sulfur being in the same group with O displays similar electronic properties and have localized states in the band gap just above the valence band originated from its p_x and p_y orbitals.

Titanium can be adsorbed to both Mo and S layers. In Fig. 3.8 localized states of both adsorption geometries are indicated. When Ti adsorbed to Mo-1 site, nearest d_{z^2} orbitals of Mo atoms play an important role in the binding mechanism. Charge density isosurface of the state numbered as '1' in Fig. 3.8 is dominated from Ti's d_{z^2} , whereas isosurfaces '2' and '3' are dominated by d_{xy} and $d_{x^2-y^2}$ of Ti which are parallel to Mo-layer. As for Ti adsorbed at S-3 site, Ti- d_{xy} and d_{xz} orbitals states dominate states numbered as '1' and '2' but the state numbered as '3' originates mainly from Ti- d_{z^2} orbital. Cr and Mo adatoms at S-3 site on 1H- MoS_2 surface have four d -states singly occupied, but d_{xy} state is doubly occupied. Cr- s and Mo- s orbitals are vacant in both adatoms. Hence Cr and Mo has local magnetic moment of $\mu = 4\mu_B$. As for W adatom at S-2 site, its localized magnetic moment of $\mu = 2\mu_B$ occurs from the spin-polarized d -orbitals of W together with the p -orbitals of nearest S-atom.

Carbon adatom is of particular interest. Previously, He *et al.*[98] found that the lowest energy adsorption position of C adatom occurs in the plane of sulfur

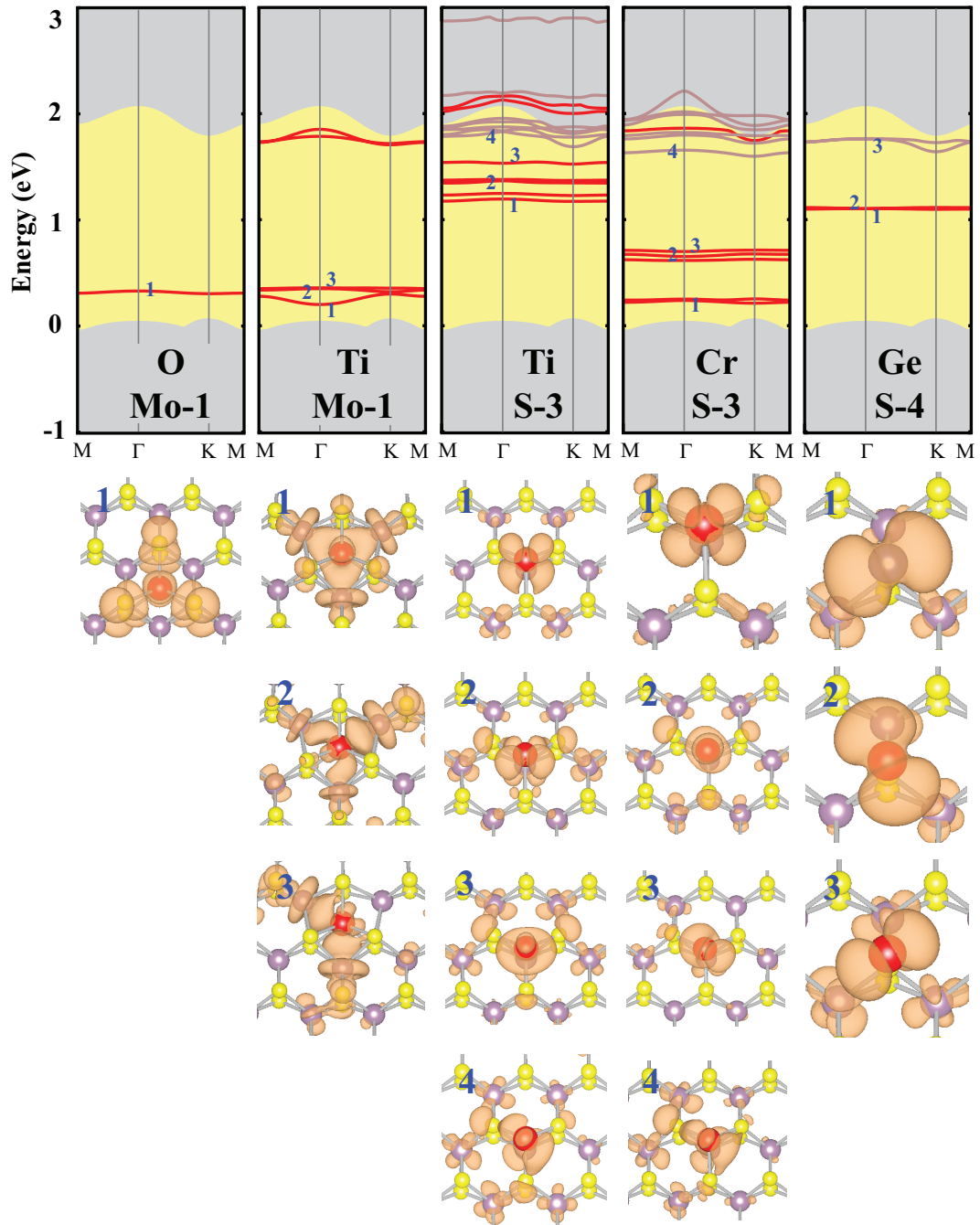


Figure 3.8: Schematic diagram of the relevant energy levels (or bands) of single adatom (O, Ti, Cr and Ge) adsorbed to each (4×4) supercell of 1H- MoS_2 . The grey (light) shaded region in the background is the valence and conduction band continua. For nonmagnetic case, red (dark) bands are contributed more than 50% by adatoms orbitals, For magnetic case, spin-up and spin-down bands are shown by red (dark) and brown (light) lines, respectively. Solid bands indicate that the contribution of adatom to the band is more than 50%. In the lower part of each panel the adsorption site is indicated by the labeling of Fig. 3.7. Charge density isosurfaces of adatom states specified by numerals are shown below. The isosurface value is taken as 2×10^{-5} electrons/ \AA^3 . Taken from Ataca *et al.*[6]

atoms on top of Mo atom (namely S-3 site shown in Fig. 3.7). Here, we found the same site with a binding energy of $E_b=2.69$ eV. However, C adatom can go over a shallow barrier to a more stable adsorption position, namely Mo-1 site with $E_b=3.28$ eV at the center of three Mo atoms below the plane of S atoms. In Fig. 3.9 we present a detailed analysis of these two adsorption sites. For Mo-1 site, sp^2 hybridized orbitals of C adatom and d_{xy} and $d_{x^2-y^2}$ orbitals of surrounding 3 Mo atoms form three bonds, but the system remains nonmagnetic. In the case of S-3 site, sp^2 hybridized orbitals of C adatom form three bonds with the orbitals of surrounding three S atoms of 1H- MoS_2 . The interaction of p_z orbital of C adatom with the underlying Mo d_{z^2} orbitals results in a significant charge transfer from Mo to C adatom. This creates a local magnetic moment of $\mu=2 \mu_B$ on Mo atom. The charge density contour plots in Fig. 3.9 (b) and (c) in a perpendicular and lateral planes show the bonding configuration. Recently a peculiar growth process, where carbon adatoms adsorbed to graphene readily diffuse above room temperature and nucleate segments of linear carbon chains (CACs) attached on graphene is predicted.[142] The diffusion barrier they calculate on graphene is reported as 0.37 eV. The energy difference of C adatom between different adsorption sites, namely S-3 and S-4, is 0.45 eV and comparable to that of C atom on graphene. Here we went beyond the adsorption of individual atoms and addressed the question whether carbon adatoms can also lead to the formation of CACs on 1H- MoS_2 . Different from the single C adatom adsorption on 1H- MoS_2 , CACs (starting from C_2) prefer to adsorb on the top of S atoms as shown in Fig. 3.9 (d) and (e). When attached to 1H- MoS_2 , CACs favor cumulene like structures with slightly alternating bonds and with a different kind of even-odd disparity. Therefore the top-site geometry occurs due to the double $sp+\pi$ -bonding within cumulene. Similar to the case in graphene, the binding energy of CACs having even number of C atoms are greater than those having odd number of C atoms. Even though CAC on graphene are nonmagnetic structures, odd number CACs on 1H- MoS_2 have a magnetic moment of $2 \mu_B$ arising from C atoms at the edges of CAC.

Since the atomic radii of other group 4A elements, Si and Ge, are larger than that of C adatom, their adsorption geometry differs from the adsorption site of C at the S-3 site. Si and Ge can only be adsorbed on the S-plane at the S-4 site

Table 3.4: Calculated values of adatoms adsorbed to the bare armchair MoS₂ nanoribbon having $n=12$ MoS₂ units in the primitive unit cell. The supercell in calculations consist of three primitive cells. There are two different adsorption sites as (described in Fig. 3.10) for each adatoms. The positions only with a positive binding energy is indicated. h_{Mo} , the height of the adatom from Mo layer; h_S , the height of the adatom from the nearest S-layer; d_{Mo} , the adatom-nearest Mo distance; d_S , the adatom-nearest S distance; E_b , adatom binding energy; μ_T , magnetic moment per supercell in Bohr magneton μ_B ; ρ^* , excess charge on the adatom (where negative sign indicates excess electrons); Φ , photoelectric threshold (work function); P, dipole moment calculated in the x , y and z direction, respectively. Nanoribbon is in the (x, y) -plane and along the x -direction. E_i , energies of localized states induced by adatoms. Localized states are measured from the top of the valence bands in electron volt. The occupied ones are indicated by bold numerals and their spin alignments are denoted by either \uparrow or \downarrow . States without indicated spin alignment are nonmagnetic. Taken from Ataca *et al.*[5]

Atom	Site	h_{Mo} (Å)	h_S (Å)	d_{Mo} (Å)	d_S (Å)	E_b (eV)	μ_T (μ_B)	ρ^* (e)	Φ (eV)	P ($e \times \text{Å}$)	E_i ↑: Spin-up, ↓: Spin-down States
C	NR _{IE} -1	0.63	0.95	1.95	1.81	5.69	NM	-0.67	5.60	(-22.45, 0.63, -0.15)	-15.05 , -9.05
	NR _{OE} -1	-0.01	1.55	2.00	1.79	6.35	NM	-0.56	5.43	(-26.58, 0.52, -0.02)	-15.63 , -8.48
O	NR _{OE} -2	0.00	1.56	1.72	3.56	6.67	NM	-0.73	5.64	(0.84, 1.52, 0.00)	-5.82 , -5.81 , -5.63 , -1.16 , -0.90
Co	NR _{IE} -2	0.11	1.45	2.40	2.15	4.81	1.00	0.22	5.42	(3.15, 0.04, -0.09)	-1.12 ↑, -0.40 ↑, -0.36 ↓, -0.31 ↑, 0.38↓, 0.38↓, 1.23↑
	NR _{OE} -1	-0.02	1.55	2.32	2.17	4.44	0.85	0.26	5.19	(-13.83, -1.45, -0.03)	-0.95 ↑, 0.16 ↑, 0.29 ↓, 0.56↓, 1.17↓, 1.23↑

and attain a local magnetic moment of $\mu = 2 \mu_B$. This is a crucial result, since magnetic properties to MoS₂ monolayer are implemented through nonmagnetic adatoms.

The excess charge on the adatom (which is denoted as ρ^* in Tab. 3.3), as well as the position of the highest localized state in the gap are correlated with its electronegativity. For example, among C, Si and Ge, C has the highest electronegativity. While C has negative excess charge, Si and Ge becomes positively charged when adsorbed. Calculated dipole moment on the system of C adatom adsorbed to S-layer is diminished due to the local reconstruction. While adsorbed C, O and S adatoms have excess electrons, all other adatoms in Tab. 3.3 are positively charged. Vanadium and W adsorbed at S-2 site have significant positive charge, but both induce minute electric dipole moment due to the local reconstruction. It should be noted that excess charging of surfaces of 1H-MoS₂ by a higher level of coverage of specific adatoms can improve its functionalities in tribology.

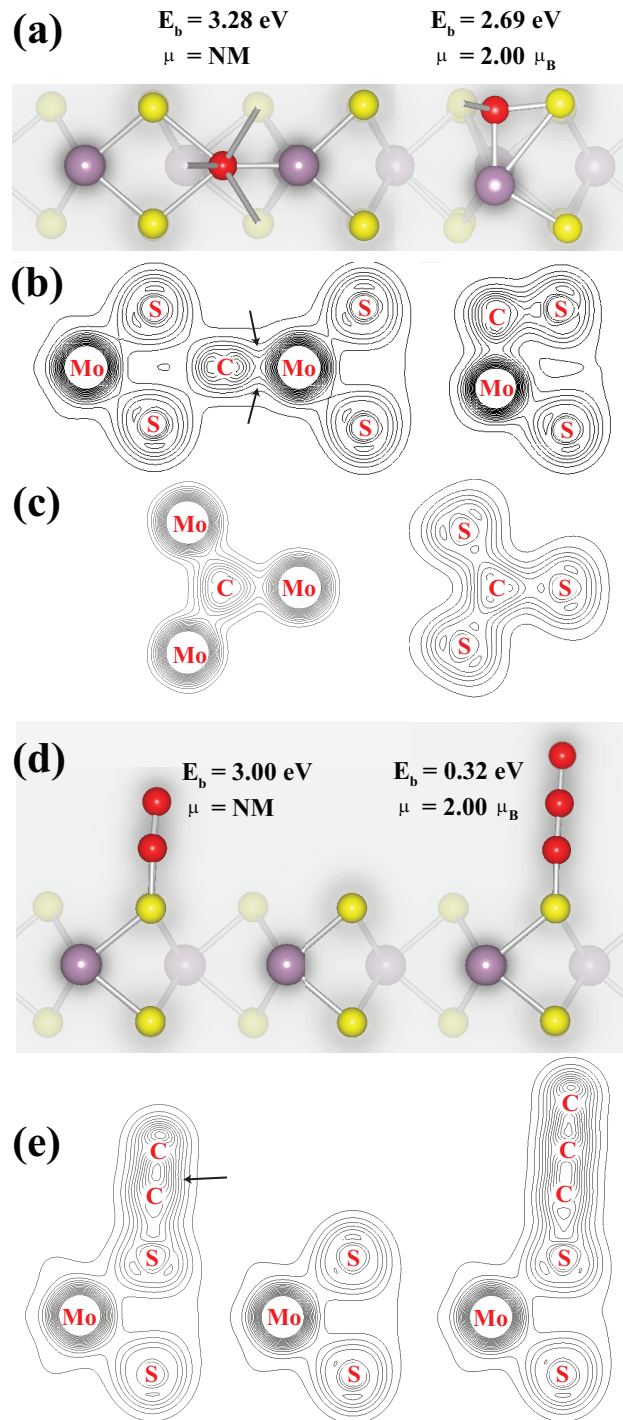


Figure 3.9: Analysis of bonding configuration of C adatoms on 1H-MoS₂. (a) Geometries of single C adatom adsorbed in the Mo-plane (left) and in the S-plane (right). Adatoms, host Mo and S atoms are represented by red (medium-dark), purple (large-gray) and yellow (small-light) balls, respectively. (b) Contour plots of total charge density of plane passing through atoms and bonds highlighted (not shaded) in (a). (c) Contour plots of total charge density on the horizontal plane passing through Mo-C and S-C bonds parallel to 1H-MoS₂. (d) Adsorption geometry and energetics of C₂ and C₃ on 1H-MoS₂. (e) Contour plots of total charge density on the vertical plane passing through atoms and bonds emphasized (not shaded) in (d). The direction of the arrows indicate the increasing charge density. Taken from Ataca *et al.*[6]

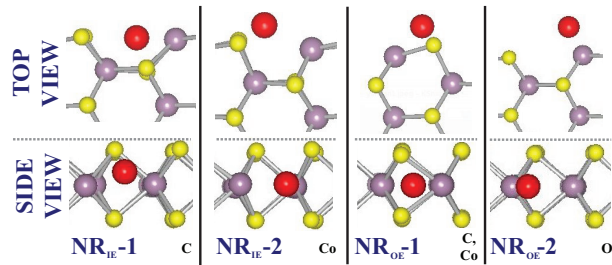


Figure 3.10: Top and side views for the schematic representation of possible adsorption geometries of adatoms obtained after the structure optimization. Adatoms, Mo and S are represented by red (large-dark), purple (medium-gray) and yellow (small-light) balls, respectively. Side view clarifies the height of adatoms from Mo and S atomic planes. In each possible adsorption geometry, the entry on the lower-left part indicates where the adatom is initially placed. All sites show geometries associated with the adsorption to a bare armchair ($n=12$) nanoribbon (NR). The calculations are carried out in the supercell geometry where a single adatom is adsorbed at every three unit cells. The total number of atoms in the supercell is 109. Possible adsorption geometries in NR_{IE} (adatom is initially placed at the inner edge of bare armchair NR) and NR_{OE} (adatom is initially placed at the outer edge of bare armchair NR). Adatoms indicated at lower right part of every possible adsorption geometry correspond to those, which are relaxed to this particular geometry upon structure optimization. Taken from Ataca *et al.*[5]

In the case of adatom adsorption to MoS_2 nanoribbons, we consider armchair nanoribbon as a prototype since it is nonmagnetic and band gap does not vary significantly as the width of the nanoribbon varied. By this way, we can model the effect of adatoms simply. We investigate the adsorption of C, O and Co. C is widely investigated in other honeycomb structures; the adsorption O is expected to result in important changes due to its high electronegativity. On the other hand, Co being a transition metal atom is expected to attribute magnetic properties. In the supercell geometry, a single adatom is adsorbed at every three unit cells, which leads to the adatom-adatom distance of $\sim 16.60 \text{ \AA}$. We found that the edges of the nanoribbon are active sites for adsorption and are energetically more favorable relative to the center of nanoribbon. As described in Fig. 3.10, adatoms adsorbed at the inner (NR_{IE}) and outer parts of the edges (NR_{OE}) of the armchair nanoribbon result in a reconstruction on the edges and form strong bonds with nanoribbon. In Table 3.4, we present all relevant data obtained from our calculations of adatoms adsorbed to A- MoS_2 NR. The height of the adatom from the Mo- or S-planes are calculated relative to the average heights of Mo- and S- atoms in the corresponding planes. The binding energy, E_b is calculated as $E_b = E_{ad} + E_{A-\text{MoS}_2} - E_{ad+A-\text{MoS}_2}$. Here, E_{ad} is the ground state energy of free adatom calculated in the same supercell with the same parameters; $E_{A-\text{MoS}_2}$ is the total energy of nanoribbon and $E_{ad+A-\text{MoS}_2}$ is the energy of adatom+A- MoS_2 NR complex. Here the adatom+A- MoS_2 NR complex attains net magnetic moment after the adsorption of transition metal atom, Co. Adsorption of C and O do not cause any spin polarization in all adsorption geometries. Adsorbed O having the highest electronegativity among the adsorbates treated here has highest excess charge; C is also negatively charged in both adsorption geometries. Co adatom having electronegativity smaller than those of both constituent atoms of the nanoribbon is positively charged. The depletion and annihilation of charge from the adatom result in a small dipole moment in the y -direction, which is normal to the ribbon. Since adatom-adatom interaction is hindered due to large supercell dimensions, the localized states form flat bands in the supercell geometry. For C and O localized states deep in the valance band are generally due to their low energy $2s$ -states. For Co adatom most of the localized states originate from $3d$ -orbitals.

3.6.2 Functionalization by Vacancy Defects

It is known that the vacancy defect in 2D graphene,[143, 144, 145, 146, 147] graphene nanoribbons,[148, 149] 2D graphane[150] and graphane nanoribbons[151] give rise to crucial changes in the electronic and magnetic structure. According to Lieb's theorem,[152] the net magnetic moment of the structure occurs due to the difference in the number of atoms belonging to different sublattices A and B, namely $\mu = (N_A - N_B)\mu_B$. While magnetic moments calculated using DFT for vacancies in 2D graphene and armchair graphene nanoribbons generally confirmed Lieb's theorem, results are diversified for vacancies in zigzag graphene nanoribbons[148, 149] due to the coupling with magnetic edge states. In the case of 1H- MoS_2 , Lieb's theorem cannot be directly applicable, even if alternating Mo and S units form a honeycomb structure. We investigated five different types of vacancy defects, namely Mo-, S-vacancy, MoS-, S_2 -divacancy and MoS_2 -triple vacancy, which are formed in 2D 1H- MoS_2 . All structures are optimized upon the creation of a particular type of vacancy. Vacancy energies, E_V , are calculated by subtracting the total energy of the perfect structure (without vacancy) from the sum of the total energy of a structure having a particular type of vacancy and the total energy(ies) of missing atoms in the vacancy defect. Here all structures are optimized in their ground states (whether magnetic or nonmagnetic). Positive E_V indicates that the formation of vacancy defect is an endothermic process. In Table 3.5 vacancy energies as defined above and their magnetic ground states are presented. We note that the equilibrium concentrations of vacancies are usually very low owing their high formation energies. Nonetheless, new techniques have been developed to create defects, which makes also the generation of nanomeshes vacancies possible.[153, 154, 155]

We carried out calculations on vacancy defects of Mo, S and S_2 , in the (2x2), (4x4) and (7x7) supercells of 1H- MoS_2 structure. Even if relatively larger sizes of supercells are not affected, the size of supercell is contracted upon creating a vacancy defect in the (2x2) supercell. In addition to these, we also consider MoS-divacancy and MoS_2 -triple vacancies in (7x7) supercells. For all these supercell sizes including the (7x7) supercell, we have carried out calculations with

Table 3.5: Calculated vacancy energies E_V (in eV), magnetic moments μ (in μ_B) of five different types of vacancy defects, Mo, MoS, MoS_2 , S, S_2 in (7x7) supercell of 1H- MoS_2 . NM stands for nonmagnetic state with net $\mu=0 \mu_B$. E_i s denote the energies of localized states in the band gap measured from the top of the valence bands (in eV). The occupied ones are indicated by bold numerals and their spin alignments are denoted by either \uparrow or \downarrow . States without the indication of spin alignment are nonmagnetic. Taken from Ataca *et al.*[6]

	Mo	MoS	MoS_2	S	S_2
	$E_V-\mu$	$E_V-\mu$	$E_V-\mu$	$E_V-\mu$	$E_V-\mu$
2D	13.44-NM	17.36-NM	22.63-2.00	5.89-NM	11.74-NM
E_1	0.26	0.15	0.15 \uparrow	0.12	0.12
E_2	0.27	0.25	0.16 \uparrow	1.22	1.17
E_3	0.61	0.54	0.25 \downarrow	1.23	1.19
E_4	1.02	0.69	0.28 \uparrow		
E_5		1.21	0.53 \downarrow		
E_6		1.36	0.73 \uparrow		

many different initial magnetic moment configurations, but all of the vacancy defects, except MoS_2 triple vacancy, the magnetic moment on any of the atoms in the supercell vanished. To justify these results, we also repeated the calculations using LDA+PAW, which also results in a magnetic state for MoS_2 -triple vacancy having a net magnetic moment of $\mu_T = 2\mu_B$. We seek the origin of magnetic states in the charge transfer between Mo and S and hence examined charge densities around the vacancy defects. In case of S and S_2 vacancy defects, the excess (positive) charge on the nearest Mo adatoms around the vacancy slightly decreases, and hence does not cause any magnetic moment. The charge transfers and resulting excess charges around Mo and MoS_2 vacancies are affected even up to third nearest neighbor atoms. For example S atoms around Mo vacancy have 0.1 electrons less charge, since the third Mo atom, which provides excess electrons to S is missing. However these S atoms surrounding Mo vacancy receive more charge from nearest two Mo atoms. Similar cases also investigated for MoS vacancy defects. Nonetheless, the charge transfers at the close proximity of S, S_2 , Mo and MoS vacancies are not significant as compared with those of the perfect structure and consequently do not lead to a magnetic state. Interestingly, the disturbances in the charge transfer due to MoS_2 -triple vacancy are significant

and result in the magnetic state at the close proximity of the defect.

In Figure 3.11, we present the isosurfaces of the difference of charge density of spin-up and spin-down states (i.e. $\Delta\rho_{\uparrow,\downarrow} = \rho_{\uparrow} - \rho_{\downarrow}$ at the close proximity of MoS_2 vacancy. After reconstruction around the vacancy, 2 Mo and 4 S atoms have dangling bonds. In this case, Mo atoms having dangling bonds are also less positively charged and S atoms having dangling bonds are less negatively charged as compared with those of perfect MoS_2 . However, in comparison with S, S_2 , Mo and MoS vacancies the amount of charge transfers here are almost doubled to cause to significant disturbances and spin polarization. The total magnetic moment of $2 \mu_B$ are originated equally from d_{yz} and d_{zx} orbitals of Mo and p orbitals of S which have dangling bonds as seen in Fig. 3.11. The nonmagnetic state is ~ 130 meV energetically less favorable. Electronically, vacancy defects give rise to states in the band gap, which are localized at atoms around the vacancy (see Table 3.5). The band gap, as well as the electronic properties of 1H- MoS_2 are modified by these states.

For a hydrogen saturated armchair nanoribbon (A- MoS_2NR), having width $n=12$, the vacancy defects formed near the center of the nanoribbons are treated in a supercell geometry, where a single defect is repeated in every four unit cell. For this supercell configuration, vacancy-vacancy coupling becomes minute and the resulting defect states appear as flat bands. Similar to 1H- MoS_2 , all the vacancy types have zero net magnetic moments, except MoS_2 -triple vacancy, which has a net magnetic moment of $\mu = 2\mu_B$ per supercell. The nonmagnetic excited states associated with vacancy defects occur above ~ 120 meV, and are derived from Mo- $4d$ and S- $3p$ orbitals around the vacancy. Calculated vacancy energies, net magnetic moments per cell are presented in Table 3.6.

Similar to the armchair nanoribbons, various vacancy, di- and triple-vacancy defects formed in the center of hydrogenated zigzag nanoribbon (Z- MoS_2NR), having width $n=6$ are treated in a supercell geometry, where a single defect is repeated in every eight unit cell. Calculated vacancy energies, net magnetic moments per cell are presented in Table 3.6. It is found that in the presence of a vacancy defect, such as MoS-divacancy, S_2 -divacancy, Mo-vacancy and S-vacancy,

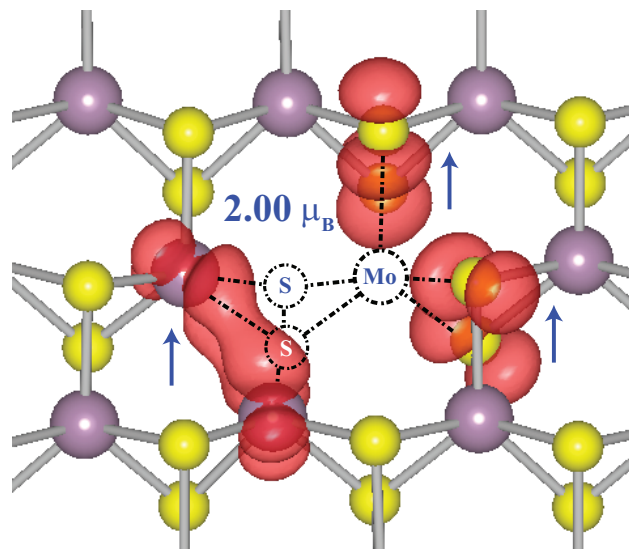


Figure 3.11: Isosurfaces of difference charge density of MoS_2 vacancy defect in the (7×7) supercell of 1H- MoS_2 . Dashed atoms and bonds are vacant sites. Difference charge density is obtained from the difference of spin-up and spin-down charge densities. ($\Delta\rho_{\uparrow,\downarrow} = \rho_{\uparrow} - \rho_{\downarrow}$) The total magnetic moment is calculated as $2 \mu_B$. Up arrow indicate the excess spin-up charge. Isosurface value is taken as $3 \times 10^{-3} \text{ eV/\AA}^3$. Taken from Ataca *et al.*[6]

Table 3.6: Calculated vacancy energies E_V (in eV), magnetic moments μ (in μ_B) of five different types of vacancy defects, Mo, MoS, MoS_2 , S, S_2 in A- MoS_2 NR and Z- MoS_2 NR. NM stands for nonmagnetic state with net $\mu=0$. E_i , energies of localized states in the band gap. Localized states are measured from the top of the valence bands in electron volt. The occupied ones are indicated by bold numerals and their spin alignments are denoted by either \uparrow or \downarrow . Nonmagnetic states have no spin alignments. Taken from Ataca *et al.*[5]

	Mo	MoS	MoS_2	S	S_2
	$E_V-\mu$	$E_V-\mu$	$E_V-\mu$	$E_V-\mu$	$E_V-\mu$
A- MoS_2 NR	16.92-NM	17.47-NM	22.94-2.00	5.82-NM	11.55-NM
E_i	0.09 , 0.11 , 0.35, 0.48	0.11 , 0.40, 0.49	0.02 \uparrow , 0.03 \downarrow , 0.33 \downarrow , 0.34 \downarrow , 0.50 \uparrow	-	-
Z- MoS_2 NR	15.78-8.06	16.41-8.66	22.02-8.67	5.09-8.61	10.77-8.31

the spin-polarization of the zigzag nanoribbons appears to be suppressed. For example, while defect free, zigzag nanoribbons are metallic and spin-polarized ground state with net magnetic moment of $\mu = 2.24\mu_B$ per double unit cell, the total magnetic moment of eight unit cell decreases to $\sim \mu = 8.30\mu_B$ per supercell from $\mu = 8.96\mu_B$ in the presence of vacancy defects. In particular, the net magnetic moment of MoS_2 -triple vacancy appear to compensate for the edge magnetization of the zigzag MoS_2 NR to result in a net magnetic moment of $8.67\mu_B$ per supercell.

Chapter 4

Beyond MoS₂: Stable, single layer MX₂ transition metal oxides and dichalcogenides in honeycomb like structure

4.1 Preliminary Information

Exceptional properties, such as high carrier mobility, linearly crossing bands at the Fermi level and perfect electron-hole symmetry which originates from the strictly two-dimensional (2D) honeycomb structure, made graphene an attractive material for future applications.[16, 19] Other Group IV elements, Si and Ge, also have been shown to form buckled honeycomb structures with bands linearly crossing at the Fermi level.[156, 157] In addition, suspended 2D single layer BN[20] and much recently, single layer transition metal dichalcogenides, MoS₂[21] and WS₂[22] with honeycomb structure have been synthesized. Single layer NbSe₂ was synthesized only on SiO₂ substrate.[158] Theoretical[23, 24, 5, 6, 1] and experimental studies dealing with the electronic structure, lattice dynamics, Raman spectrum[25, 3] and Born effective charges indicate that single layer MoS₂ is a

nonmagnetic semiconductor displaying exceptional properties. In a recent study, a transistor is fabricated from single MoS_2 layer.[30] While graphene is ideal for fast analog circuits, single layer MoS_2 appears to be promising for optoelectronic devices, solar cells and LEDs.

Three-dimensional (3D) MX_2 (M: Transition Metal; X: Chalcogen atom) compounds are one of the most interesting class of materials, which display a wide range of important properties. Their bulk compounds include oxide superconductors,[159] half-metallic magnets,[160] superlubricants,[26] catalyst in redox-based reactions,[161] solar converters[162] *etc.* Some of these compounds have D_{6h} point group symmetry and occur in layered structures formed from the stacking of weakly interacting 2D MX_2 layers and are specified as 2H- MX_2 . Another type of layered structure known as 1T structure has D_{3d} point group symmetry and is common to several of MX_2 compounds. Only a few 3D MX_2 compounds can be stable both in 2H and 1T structures. In addition to 2H and 1T layered structures, some MX_2 compounds can be stable in one of 3D structures known as rutile, 3R, marcasite, anatase, pyrite and tetragonal structures. An extensive review of bulk 3D MX_2 compounds can be found in Ref. [163]. Following outline on the properties of 3D MX_2 compounds heralds the importance of their single layer structures.

Rutile crystal and thin films of CrO_2 have been investigated due to their spintronic applications. Tunneling magnetoresistance in films of half-metallic CrO_2 was initially observed.[164] Electronic and magnetic properties of bulk[165] and epitaxial[166] CrO_2 are also reported theoretically.[167] Single layer of CoO_2 plays an important role for understanding the superconducting properties of Ni and Co oxide based compounds. In these structures single layers of CoO_2 are separated generally by thick insulating layers of Na^+ ions and H_2O molecules.[159] High T_C superconducting properties of these structures arise from the single layer of CoO_2 plane. Electronic, magnetic and optical properties of cubic pyrite type CoS_2 structure are investigated theoretically[160, 168, 169, 170, 171] and focused on the half-metallic property of this magnet. Experimental synthesis of pyrite CoS_2 was achieved much earlier.[172, 112] One can synthesized pyrite phase of CoSe_2 and FeSe_2 by photoinduced structural conservation.[173]

VO_2 have various allotropes at different temperatures. For example at low temperature monoclinic (M1) phase occurs, whereas at high temperatures rutile metallic phase is favorable. By varying the temperature of the system, one can observe the metal insulator transition.[174] Not only visible light absorption of TiO_2 layers can be enhanced by insertion of thin (~ 2 nm) VO_2 film[175], but also TiO_2 plays an important role to hinder the oxidation of VO_2 . [176] Thin films of VO_2 also display thermochromic properties in which temperature affects the color of the substance.[177, 178] Absence of nesting in charge-density-wave system in 1T-VS_2 has been attributed to the weak electron-electron interaction. Synthesis and characterization of layered structure of bulk VSe_2 and its superconducting properties were also investigated experimentally.[179, 180]

The interaction of iron with chalcogens specifically with O_2 molecule is of great interest, since it takes place in processes varying from corrosion to oxygen transport in biological systems. It can also be used as catalysts or catalytic supports in redox-based reactions.[161] FeS_2 , the most well known compound among other Fe based materials, has been studied extensively. The pyrite structure, the most stable polymorph of FeS_2 , is a crucial compound in materials research.[181, 182, 183, 184, 185] Recently a new method has been put forward and used to synthesize 2D nanowire networks of FeS_2 . [186] Powders of FeS_2 showing rod-like morphologies are attracting considerable interest, since it is a promising material for solar energy conversion. The shape and thermodynamical stability of FeS_2 powders have been investigated using first-principles methods pointing out the differences between nano and macro scale.[187] FeS_2 nanosheets on iron substrates are also used as photocathodes from tandem dye-sensitized solar cells.[188] FeS_2 pyrite nanocrystal inks are also used in thin-film photovoltaic solar cells.[162]

The most recent experimental study by Coleman *et al.*, [74] which reported liquid exfoliation of MoS_2 , WS_2 , MoSe_2 , TaSe_2 , NbSe_2 , NiTe_2 , MoTe_2 nanosheets having honeycomb like structures has motivated us to engage in an extensive analysis of stability to address the question whether other single layer transition metal dioxides or dichalcogenides MX_2 , can exist in honeycomb like structures. In this chapter we examined 44 MX_2 compounds ($\text{M} = \text{Sc, Ti, V, Cr, Mn, Fe, Co, Ni, Nb, Mo, W}$ and $\text{X} = \text{O, S, Se, Te}$) to reveal which ones can be stable in 2D

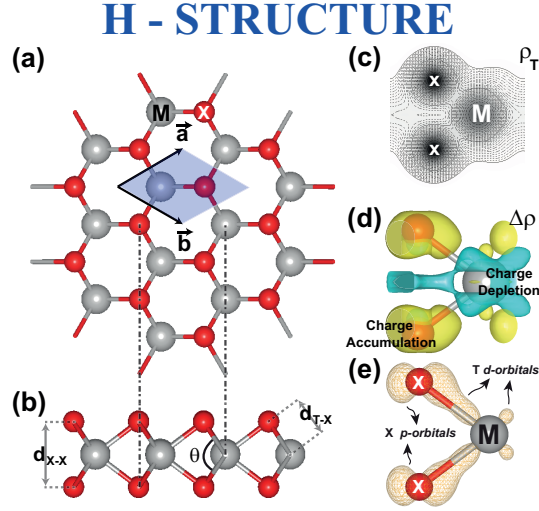


Figure 4.1: Atomic structure and charge density analysis of 2D single layer MoO_2 as a prototype. (a) Top and (b) side views of H-structure showing the primitive unit cell of 2D hexagonal lattice with Bravais lattice vectors \vec{a} and \vec{b} ($|\vec{a}|=|\vec{b}|$) and relevant internal structural parameters. Large (gray) and small (red) balls indicate metal (M) and oxygen (X=O) atoms, respectively. (c) Contour plots of the total charge density, ρ_T . (d) Isosurfaces of difference charge density, $\Delta\rho$. Turquoise and yellow regions indicate depletion and accumulation of electrons, respectively. (e) Isosurfaces showing p - d hybridization in Mo-O bond. Isosurface value is taken as 0.01 electrons/ \AA^3 . In the top view in (a), unlike graphene M and X_2 occupy the alternating corners of a hexagon.

suspended, single layer structure. We took into account two different single layer structures, namely honeycomb H- and centered honeycomb T-structures; both can be viewed as positively charged 2D hexagonal lattice of M atoms, which is sandwiched between two hexagonal lattices of negatively charged X atoms. In both H- and T-structures, instead of forming covalent sp^2 -bonding with three neighboring carbon atoms in graphene, each M atom has six nearest X atoms and each X atom has three nearest M atom forming p - d hybridized ionic M-X bonds. Figure 4.1 and Figure 4.2 describe 2D single layer H- and T-structures together with their hexagonal unit cell, contour plots of the total charge density ρ_T , the isosurfaces of difference charge density $\Delta\rho$ (where charges of free atoms situated at the optimized crystal structure are subtracted from ρ_T).

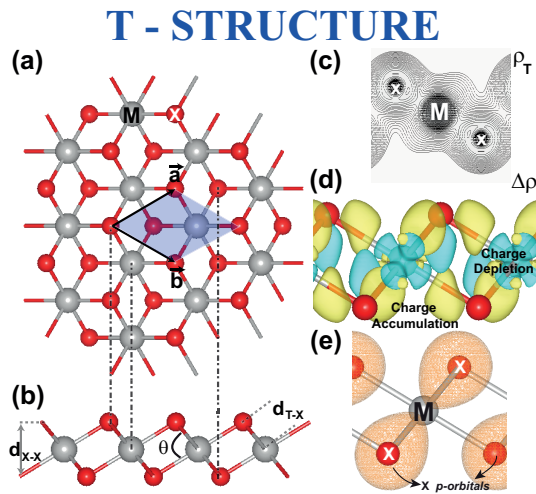


Figure 4.2: Atomic structure and charge density analysis of NiS_2 as a prototype. (a) Top and (b) side views of T-structure showing the primitive unit cell of 2D hexagonal lattice with Bravais lattice vectors \vec{a} and \vec{b} ($|\vec{a}|=|\vec{b}|$) and relevant internal structural parameters. (c) Contour plots of the total charge density, ρ_T . (d) Isosurfaces of difference charge density, $\Delta\rho$. Turquoise and yellow regions indicate depletion and accumulation of electrons, respectively. (e) Isosurfaces showing Ni-S bonds. Isosurface value is taken as $0.01 \text{ electrons}/\text{\AA}^3$. In the top view in (a), while one of two X atoms occupies alternating corners of a regular hexagon, the second X atoms are displaced by $(\vec{a} + \vec{b})/3$ to occupy the centers of the adjacent hexagons.

4.2 Stability analysis

MX_2 compounds have diverse 3D crystal structures in different space groups, which are given in Table 4.1. Among these 2H and 1T structures are layered and hence like graphite they are formed by stacking of specific layers. The structures of the remaining MX_2 compounds are not layered. The focus of our study is to determine which ones of MX_2 compounds can form stable 2D single layer structures. Our study considers only the structures having hexagonal lattice as shown in Fig. 4.1 and Fig. 4.2. These are H-structure (honeycomb) with D_{3h} point group symmetry and T-structure (centered honeycomb) with C_{3v} symmetry. The formation of single layer MX_2 compounds on a sample specific substrate may be relatively easy, but it is beyond the scope of the present study. In the course of this study, Ding *et al.*[189] investigated electronic and vibrational properties of single layer MX_2 ($M = \text{Mo}, \text{Nb}, \text{W}, \text{Ta}$; $X = \text{S}, \text{Se}, \text{Te}$) in H-structure. The only reason they considered H-structure is because these compounds form stable 2H- MX_2 in 3D. Instead of providing tests whether these 2D nanostructures are stable through full spectrum of phonons and temperature dependent ab-initio MD calculations, they calculated the phonon frequencies only at the Γ point to reveal the Raman active modes. In this respect, the work by Ding *et al.*[189] has a scope different from the present section and they apparently consider a small fraction of the manifold we treat here.

4.2.1 Structure optimization

We start our analysis of stability by calculating the total energy of MX_2 compounds in these H and T structures. Optimization takes place by minimizing the total energy and atomic forces by varying atomic positions in the unit cell and the lattice constants. If a structure is stable, the optimization usually converges to a structure. Furthermore, we calculated the cohesive energy relative to free constituent atoms, according to the formula given in the Section 3.4. We found that the calculated cohesive energies are all positive and are in the range of 10-20 eV indicating a strong binding. It should be noted that E_C is different from the

formation energies E_f , which are obtained by subtracting the cohesive energies of constituent elements in their equilibrium states (in bulk, liquid or gas forms) $E_c[M]$ and $E_c[X]$. Namely, $E_f = E_C - E_c[M] - 2E_c[X]$. For the sake of comparison, we calculate E_f using both experimental cohesive energies[11] and calculated cohesive energies of constituent elements. Calculated formation energies are positive for all H- or T-structure, which were found to be stable as a result of series of stability analysis. The optimized lattice constants and other structure parameters of stable structures are presented also in Table 4.1. The data on the lattice constants of MX_2 compounds in H-structure are not available yet. Even if the lattice constants of MoS_2 in H-structure (which is the most studied single layer MX_2) are not measured experimentally yet, they can be inferred from the lattice constants of 2H- MoS_2 . Thus the lattice constants of MoS_2 are expected to be close to those of 2H- MoS_2 , which are measured to be $a=b=3.16 \text{ \AA}$. LDA approximation is known to yield overbinding and hence lattice constants slightly shorter than the experimental values. In our study, LDA and GGA+vdW predictions are 3.11 \AA and 3.22 \AA , respectively and discussed in detail in the previous chapter.

4.2.2 Lattice Dynamics

Even if the total energy of a structure can be minimized, the stability may not be assured. Therefore, frequencies of the vibration modes of optimized single layer MX_2 in H- or T-structure are calculated for all \mathbf{k} -points in BZ to provide a rigorous test for the stability of a given structure. A structure is taken to be stable only when all calculated frequencies are positive; otherwise imaginary frequencies indicate instability. In such calculations the long wave length acoustical modes are vulnerable to instability. Thus, caution has to be taken in calculating forces with extreme accuracy.[229]

We calculated phonon branches of MX_2 compounds in H- and T-structure, which display three acoustical branches separated by a gap from six optical branches. Except a few compounds, which have imaginary frequencies in small domains as $\Omega(\mathbf{k}) \rightarrow 0$ (or $\lambda \rightarrow \infty$), all 52 2D single layer MX_2 compounds have phonon branches, which have positive frequencies in BZ. Some of MO_2 compounds

having H- and T-structures appear to have imaginary frequencies in the said domains, which may be due to limitations of DFT in highly correlated electron systems in MO_2 compounds.

Significant charge transfer and resulting polar character is the marked feature of 2D MX_2 compounds. Unlike graphene and silicene,[156, 230, 231, 232, 233, 234, 235, 236] H- and T-structure of MX_2 exhibit an interesting charge distribution as shown in Fig. 4.1 and Fig. 4.2; namely outer planes of X atoms are negatively charged, whereas the plane of M atoms between them is positively charged. Bader analysis[54] yields that electrons from M atoms are transferred to two X atoms leaving a depletion of electronic charge on M (i.e. $\rho_M > 0$) and an excess of electronic charge on X (i.e. $\rho_X < 0$). As expected $\rho_M = 2|\rho_X|$. However, CoTe_2 and NiTe_2 appear to be an exception, where the direction of charge transfer is reversed according to Bader analysis. Also excluding a few exception in transition metal oxides, ρ_M increases with decreasing row number of X atoms.

We note that the nanoribbons of MX_2 in H- and T-structures can be of interest for electronic applications. The armchair and zigzag nanoribbons of single layer MX_2 with different widths display a number of interesting properties,[5] such as band gaps showing family behavior as in graphite nanoribbons, half metallicity.[5] Earlier, the stability analysis through phonon calculations has been used successfully to examine the stability of MoS_2 armchair nanoribbon in H-structure.[5] The same analysis can be used to reveal whether the nanoribbons of specific 2D MX_2 structures are stable.

4.2.2.1 Ab-initio molecular dynamics calculation

Even if the stability of the 2D H- and T-structure of a given MX_2 compound is certified through phonon calculations, the stable structure may correspond to a local shallow minimum. Under these circumstances, the structure may be destabilized at finite temperature by abandoning the shallow minimum, even if 2D honeycomb structure is stable at $T=0$ K. This possibility of instability is tested for specific

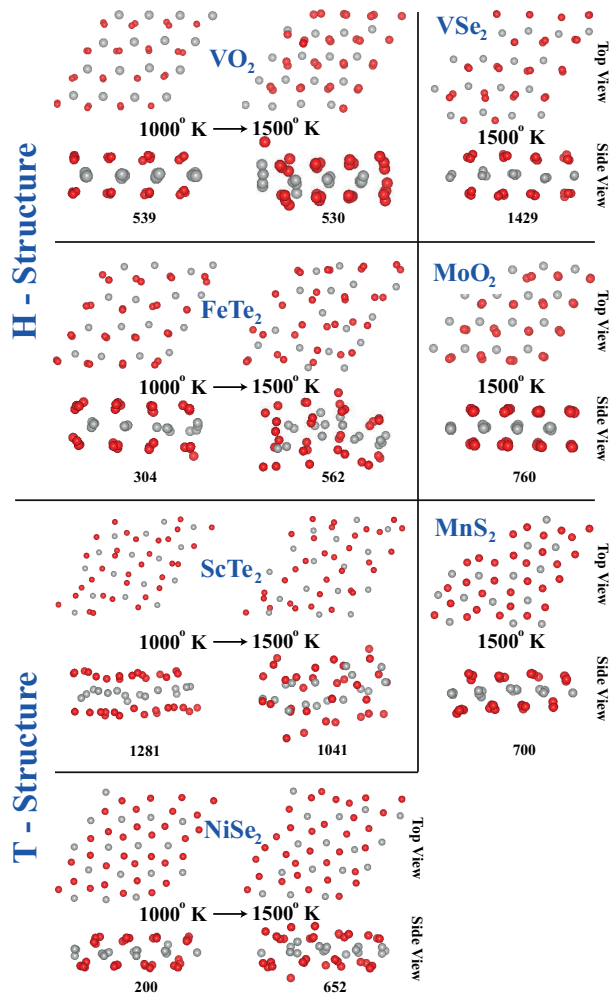


Figure 4.3: Top and side views of atomic structures of selected MX_2 compounds obtained after ab-initio molecular dynamic (MD) calculations after specified time steps and temperatures. Numerals below each panel indicate the number of MD time steps. MD results at $T=1000\text{K}$ are also shown for structures, which become unstable at $T=1500\text{K}$.

compounds using first-principles molecular dynamics (MD) calculations at various elevated temperatures, $T=500\text{K}$, 1000K and 1500K . The time steps are taken to be 2×10^{-15} seconds and velocities of atoms are normalized in every 40 steps for $T=500\text{ K}$ and 100 steps for $T=1000\text{ K}$ and 1500 K . For H-structure we consider FeTe_2 , MoO_2 , VO_2 and VSe_2 . The first three compounds have 3D crystal different from layered 2H- and 1T structures and hence they may be found to be very unlikely to occur in H-structure. In addition, because of imaginary frequencies as $\Omega(\mathbf{k}) \rightarrow 0$ in a small domain, these compounds vulnerable to instability for $\lambda \rightarrow \infty$. As for VSe_2 it has layered 1T structure and hence it is conspicuous whether H-structure can occur even if less energetic than T-structure. To avoid stability, which can be imposed by periodic boundary conditions using (1x1) unit cell calculations are carried out using (4x4) supercells. Since all four compounds remained intact after many steps (>250) at $T=500\text{ K}$, calculations are switched to $T=1000\text{ K}$ with velocity normalization at every 100 steps. Higher temperatures and normalization at relatively larger number of steps can speed up the instability, which would normally occur at relatively smaller temperature after large number of steps. If the system continues to remain stable after sufficiently large number of steps at $T=1000\text{ K}$ we raised the temperature and let MD calculations run at $T=1500\text{ K}$. $T=1500\text{ K}$ is rather high temperature and is expected to accelerate a structural instability, which could have occurred at relatively low temperatures. In fact, while H-structure of FeTe_2 remained stable after 304 steps at $T=1000\text{ K}$, it severely distorted after 562 steps at $T=1500\text{ K}$. It appears that FeTe_2 is in a shallow minimum at Born-Oppenheimer surface, so that this compound cannot survive until the temperatures, where other three compounds can remain stable. MoO_2 in H-structure was stable after 546 steps at $T=1000\text{K}$, and remained to be stable after 760 steps at $T=1500\text{ K}$. We concluded that MoO_2 can remain stable in H-structure at moderate temperatures. The situation with VO_2 is similar to that of MoO_2 , except that an O atom desorbed after 530 time step at $T=1500\text{ K}$. VSe_2 continues to be stable after 1429 time steps at $T=1500\text{K}$. The momentary geometries of MX_2 structures after several time steps are shown in Fig. 4.3.

For T-structure, we considered MnS_2 , NiSe_2 and ScTe_2 and performed ab-initio MD calculations first at $T=1000$ K and then we raised the temperature to 1500 K by normalizing the system at every 100 steps. MnS_2 was stable after 740 steps at $T=1000$ K and continues to be stable after 700 steps at $T=1500$ K with almost perfect centered honeycombs. However, the situation is different for ScTe_2 and NiSe_2 . ScTe_2 is distorted already after 1281 time steps at $T=1000$ K, and severely distorted and dissociated after 1041 time steps at $T=1500$ K. The centered honeycomb structure of NiSe_2 , which was maintained after 200 steps at $T=1000$ K, is severely distorted after 652 time steps at $T=1500$ K.

In concluding this section, ab-initio MD calculations, especially spin-polarized ones are time consuming, and hence do not allow us to obtain quantitative results. Nevertheless, we note that no matter what the parent 3D structure is, present analysis show that single layer MX_2 compounds certified to be stable through phonon calculations can remain stable at finite temperature, even above the room temperature, once they are synthesized or produced in H- or T-structures. The instability or distortion of each compound can occur at different temperature. Among structures we studied in this section those having relatively smaller formation energies become unstable or undergo severe distortion at high temperatures.

4.2.3 Mechanical Properties

Elastic constants can give further indications about the strength of stable H- and T-structures. Honeycomb structure usually underlies the unusual mechanical properties providing high in-plane strength, and flexibility in the deformations perpendicular to the atomic planes. We focused on the harmonic range of the elastic deformation, where the structure responded to strain linearly and reversibly. Method of calculation of elastic properties are indicated in Section 3.4. The calculated in-plane stiffness of single layer MX_2 materials presented in Table 4.1 ranging from 250 N/m to 9 N/m can be contrasted with the values calculated for graphene and BN, 357 N/m (experimental value 340 ± 50 N/m) and 267 N/m,

respectively. We note that generally in-plane stiffness values increase with decreasing row number of X; namely the compound softens as the row number of X increases. Accordingly, the calculated values of C is usually low for compounds having X=Te. The in-plane stiffness of WX_2 is usually higher than other MX_2 . Also C of H-structure is usually higher than that of T-structure if both structures occur for the same compound. C values given by bold numerals in Table 4.1 do not deform symmetrically. Low C and nonuniform deformation under uniform stress imply possible instability at finite temperatures.

4.3 Electronic and magnetic properties

The stable MX_2 compounds in H- and T-structures display a rich diversity of electronic and magnetic properties. Rather than providing an in-depth analysis, our discussion will be focused to the broad properties and classes showing similar properties. Depending on the combination of M and X, single layer MX_2 's can be semiconductor, ferromagnetic or nonmagnetic metal. In Fig. 4.4, Fig. 4.5 and Fig. 4.6 we present the electronic energy band structures of all stable MX_2 compounds having H- and T-structure. Because of available experimental data, the band structure of the manifold MoX_2 (X=O, S, Se, Te) in H-structure is given separately in Fig. 4.6 for detailed discussion. The MS_2 manifold (M=Sc, V, Cr, Fe, Ni and W) includes semiconductors, magnetic and nonmagnetic metals both in H-, and T-structure.

Semiconducting single layer MX_2 's having H-structure can be treated in two groups, which display rather different band structures. The first group, transition metal oxides (i.e. M=Sc, Cr, Mo, W and X=O) differ from the other group (i.e. M=Cr, Mo, W and X=S, Se, Te) by their relatively smaller band gaps and lower band-edge state densities. Here we discuss these groups by considering the band structures of MoO_2 and MoS_2 as prototypes as shown in Fig. 4.6. For both groups the bands at the edges of conduction and valence band are composed from Mo- $4d$ and X- p orbitals. However, the types (symmetry) and contributions of these orbitals vary with \mathbf{k} and with the constituents M and X. The M-X bonds of single

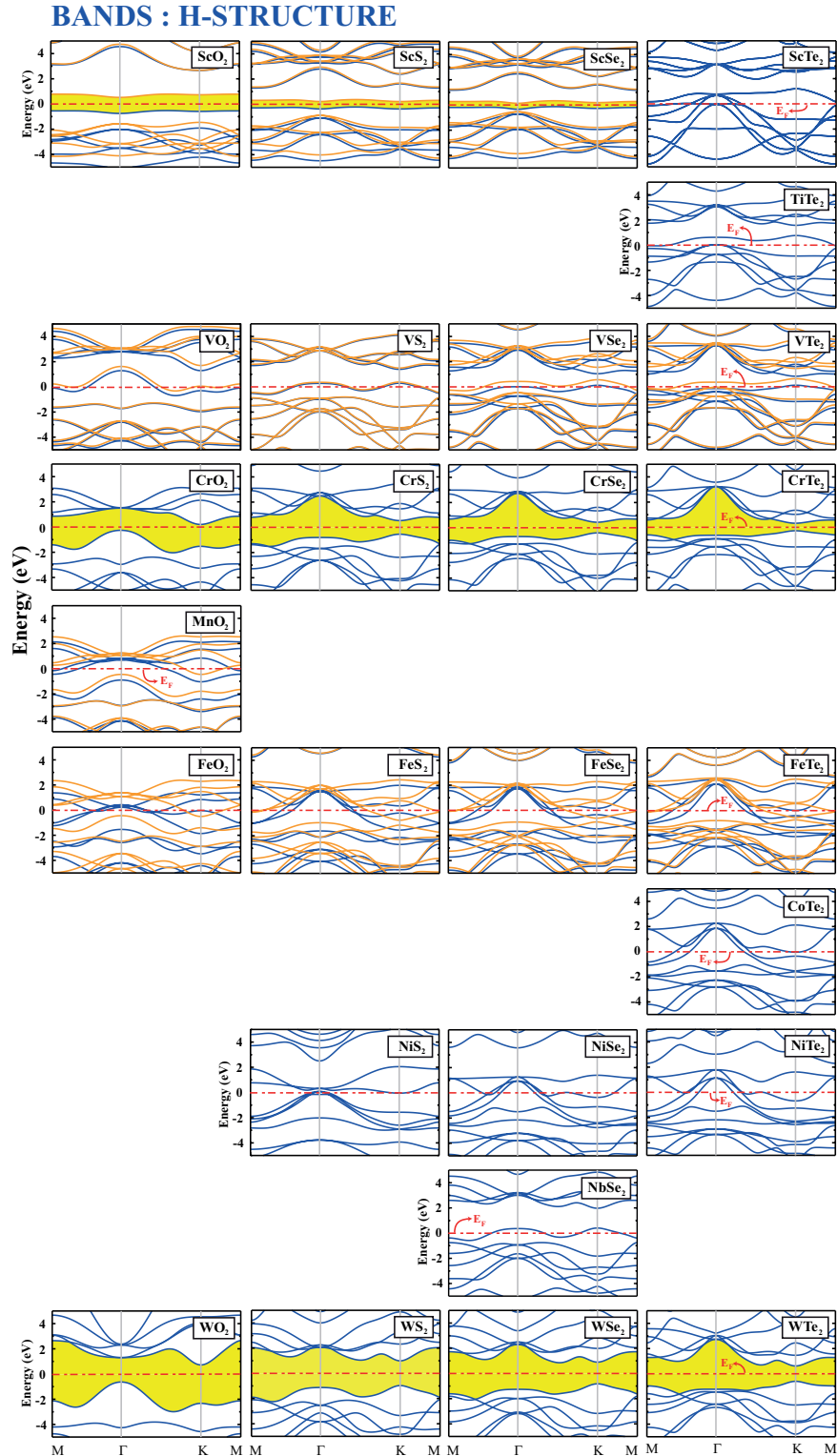


Figure 4.4: Calculated electronic band structures of 2D stable MX_2 compounds which are stable in H-structure. The zero of the energy is set to the Fermi level, E_F , shown by red/dark dashed dotted line. The energy gap of semiconductors are shaded (yellow/light). For nonmagnetic states spin-degenerate bands are shown blue/dark line. For magnetic structures, blue/dark lines represent spin-up bands whereas orange/medium lines are spin-down states. In the same row stable structures with the same M atom, but with different X atoms are presented. Columns present MX_2 manifold with the same X, but differing M atoms. The manifold MoX_2 ($X=\text{O}, \text{S}, \text{Se}, \text{Te}$) in H-structure is presented separately in Fig. 4.6.

BANDS : T-STRUCTURE

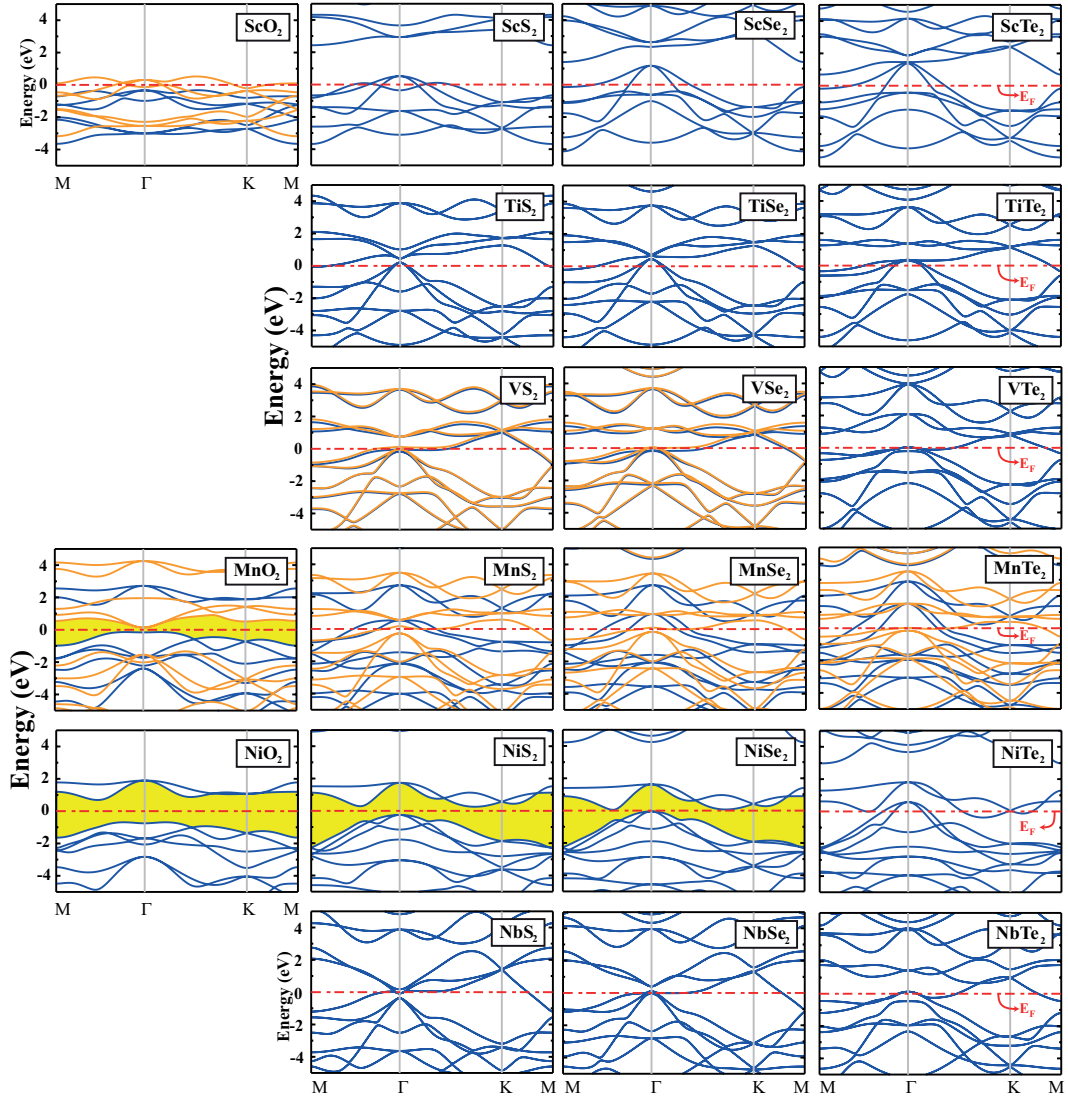


Figure 4.5: Calculated electronic band structures of 2D stable MX_2 compounds, which are stable in T-structure. The zero of the energy is set to the Fermi level, E_F , shown by red/dark dashed dotted line. The energy gap of semiconductors are shaded (yellow/light). For nonmagnetic states spin-degenerate bands are shown blue/dark line. For magnetic structures, blue/dark lines represent spin-up bands whereas orange/medium lines are spin-down states. The manifold MX_2 with the same M atom, but with different X atoms is presented in the same row. Columns present MX_2 manifold with the same X, but differing M atoms.

layer MoO_2 is 0.3-0.7 Å shorter than those in second group. Accordingly, the highest valence band at Γ combined from Mo- d_{z^2} and O- p_z orbitals has higher dispersion. This band is pushed up towards the conduction band to lower the indirect band gap between the conduction band minimum at K -point and valence band maximum at the Γ -point. Accordingly, the smallest band gap of all MO_2 honeycomb structures are indirect. On the other hand, the topmost valence band of MoS_2 , which has relatively higher Mo- d_{z^2} contribution and relatively larger M-X bonds, is flattened and its energy is lowered. Under these circumstances the smallest band gap of second group is usually direct (except MoSe_2 , which has an indirect gap only 4 meV smaller than the direct one) and occurs at the K -point between the conduction band minimum (80% Mo- d and 20% S- p_x) and valence band maximum (90% Mo- $d_{x^2-y^2}$ and 10% S- p_x). The characters of these states at the K -point are similar for X=S, Se, Te, but their direct band gap decreases slightly by going from S to Te, since $a=b$ increases from 3.12 Å to 3.46 Å. The isosurface charge densities of states at the band edges of MoSe_2 and MoTe_2 are also presented. The direct band gap of MoO_2 at the K -point is significantly larger than that of MoS_2 , since Mo-O bond is much shorter (2.78 Å). The distinction between the energy band structures of the first group and second group is also seen in the calculated total and orbital density of states given in Fig. 4.6. Another noteworthy trend we deduce from our calculations that for all single layer MX_2 semiconductors, the band gap generally increases as $\text{M}=\text{Sc} \rightarrow \text{W}$. In spite of the striking similarity of the band structures of MX_2 (X=O, S, Se and Te) as M goes from V to W, they are essentially either metal or semiconductor depending on the number of d -states of the free M atoms.

We also note that ferromagnetic metals, such as VX_2 or FeX_2 (X=O, S, Se, Te) in H-structure have the magnetic moment located at the transition metal atoms. In the case of ScX_2 (X=O, S, Se), which are ferromagnetic semiconductors, the magnetic moment is located at the site of chalcogen atoms. This occurs due to fact that Sc atom having relatively low electronegativity with respect to chalcogen atoms undergoes crucial amount of transfer of charge to X atoms. Magnetic moments then accumulate on the chalcogen atoms. In all magnetic structures, we

further carried out supercell calculations to take into account the antiferromagnetic ordering in neighboring unit cells. We conclude that ferromagnetic ordering is the energetically most favorable one.

Now we continue our discussion of the bands of MX_2 in T-structure given in Fig. 4.6: Like MoX_2 manifolds in H-structure, here nonmagnetic semiconductors occur in NiX_2 with O, S and Se. NiTe_2 is nonmagnetic metal in T-structure. NiS_2 , NiSe_2 and NiTe_2 can occur both in T- and H- structure, T being 0.2-0.5 eV energetically more favorable. However, energy band structures display significant differences by going from T to H-structure. While NiS_2 and NiSe_2 are nonmagnetic metals in H-structure, same compounds are narrow and indirect band gap semiconductors in T-structure. Even if 3D NbX_2 (X=S, Se and Te) can occur in 1T and 2H structures, NbS_2 and NbTe_2 are stable only in T-structures. Even if NbSe_2 can have both H- and T-structure, it is metallic in H-structure and 12 meV more energetic than the corresponding T-structure. Two dimensional and suspended NbSe_2 in H-structure is of particular interest, since 3D NbSe_2 is a superconductor. Similar to NiX_2 manifold, VX_2 (X=S, Se and Te) compounds form both in T- and H- structures, which have practically same cohesive energies within the accuracy limits of numerical calculations carried in the present study. In Fig. 4.7 we compare total and orbital projected densities of states (DOS) of these structures. In spite of small energy difference between T- and H-structures of these compounds, significant differences and striking common features in electronic structures are revealed. For example, VX_2 in T- and H-structures one recognizes differences in DOS. However, for both structures DOS at E_F originate from V 3d-states and are rather high. As for NiX_2 , the character of bands undergoes a change by going from T- to H-structure.

4.4 LDA+U calculations

It is known that electrons in transition metal oxides are highly correlated, which in turn limits the application of DFT to these class of materials. In this respect,

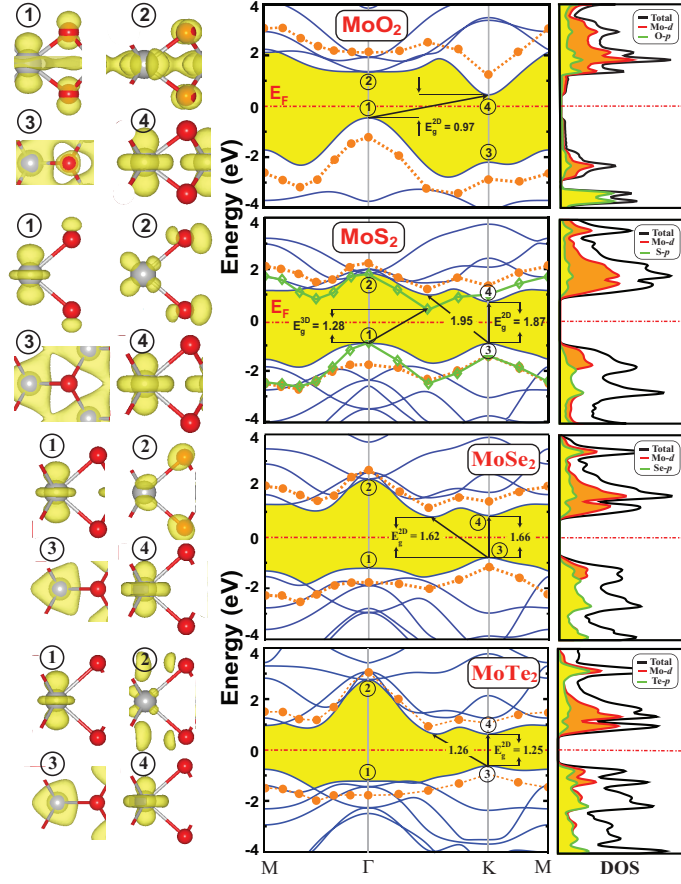


Figure 4.6: Calculated energy band structures, charge density and state densities of single layer MoX_2 ($X = \text{O}, \text{S}, \text{Se}$ and Te). Left panels are isosurface charge densities of the specific states at the band edges indicated by numerals. Isosurface value is taken as $0.01 \text{ electrons}/\text{\AA}^3$. Middle panels are band structures along the $M - \Gamma - K - M$ directions of Brillouin zone. The LDA band gap between conduction and valence band is shaded. The zero of energy is set at the Fermi level, E_F , shown by red/dark dashed dotted line. The GW₀ corrected bands are indicated by orange/light dashed lines and dots. The GW₀ corrected band gap of 3D 2H- MoS_2 is indicated by green/dark lines and diamonds. Direct and indirect band gap values are given in units of eV. Right panels are total and orbital projected densities of states DOS.

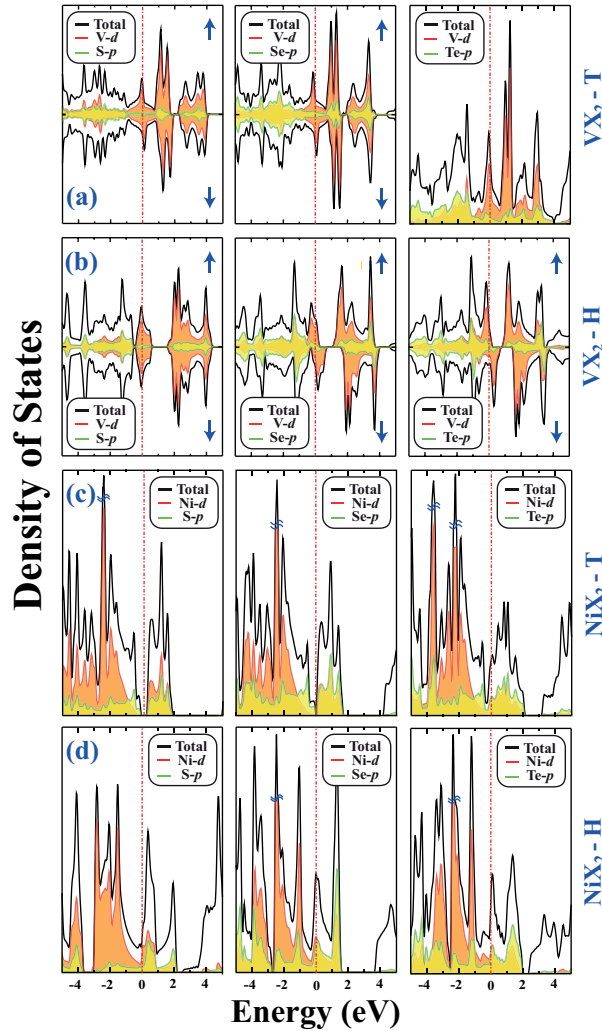


Figure 4.7: Comparison of the electronic structures of specific suspended MX_2 compounds forming both stable T- and H-structures. (a) Total densities and orbital projected densities of states (DOS) of 2D VS_2 , VSe_2 and VTe_2 compounds in T-structure. (b) Same for 2D VS_2 , VSe_2 and VTe_2 compounds in H-structure. (c) Total and orbital projected densities of states of 2D NiS_2 , NiSe_2 and NiTe_2 compounds in T-structure. (d) Same for 2D NiS_2 , NiSe_2 and NiTe_2 compounds in H-structure. The zero of the energy is set to the Fermi level, E_F , shown by red/dark dashed dotted line. Up and down arrows indicate spin-up and spin-down densities of states. Total density of states are given by thick solid lines.

predictions obtained using DFT should be taken with caution. LDA+U corrections are carried out on NiO_2 and ScO_2 in T- and on WO_2 in H-structure using the method introduced by Dudarev *et al.*[52]. In this method, the total energy of the system depends on $U - J$ term, where U is the on-site Coulomb repulsion or Hubbard term and J is the exchange parameter. Since realistic values of U and J for MO_2 compounds having either H- or T-structures are not available yet, in the present LDA+U calculations, we considered $U - J$ varying between 1 eV and 12 eV in 1 eV steps. Therefore, our analysis can only provide trends how their band gaps and lattice constants vary with U .

Bare LDA yields that ScO_2 has a half metallic ground state with integer magnetic moment per unit cell. Spin-up bands have a gap between filled and unoccupied bands, while three spin-down bands derived from oxygen p -orbitals cross the Fermi level and hence are metallic. The isosurfaces of difference charge density of spin-up and spin-down states suggests that the magnetic moment arises from the excess charge on O transferred from Sc atoms. Accordingly, Hubbard U correction is taken into account for both $3d$ -orbitals of transition metal atom and $2p$ -orbitals of O. Upon LDA+U calculations two of the three metallic bands are not affected, but energy of the third band derived from O p_z -orbital increases with increasing U energy. Eventually, the metallic spin-down bands split and open a band gap to become also semiconductor when $(U - J) > 4$. In addition, the size of the unitcell increased up to %6 for $(U - J)=11$ eV.

Bare LDA predicts that both NiO_2 and WO_2 are nonmagnetic semiconductors. The band at the edge of valence band of NiO_2 , which is non-dispersive around Γ -point is derived mainly from $3d$ -orbitals. Whereas bands slightly below the valence band edge are derived O $2p$ -orbitals. In LDA+U calculations, while the valence band edge derived from Ni $3d$ -orbitals is lowered with increasing U , the bands derived from O $2p$ -orbitals become unaltered. At the end, the bands gap of NiO_2 increases with increasing U . In contrast, the lattice constants as well as the characters of valence and conduction bands of WO_2 do not change upon Coulomb correction term. In Fig. 4.8, results of our LDA+U calculations with $J=1$ eV are summarized. Apparently, the effect of Coulomb correlation is significant for ScO_2 and NiO_2 having $3d$ -orbitals. However, WO_2 having bands derived

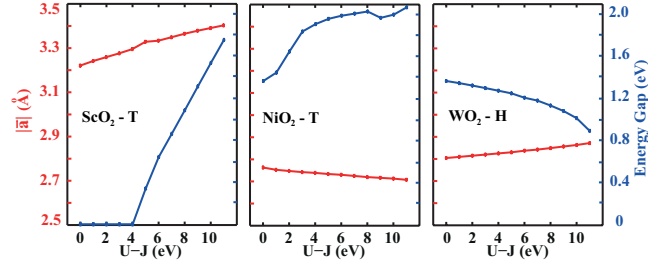


Figure 4.8: Variation of lattice constants, $|\vec{a}|=|\vec{b}|$ and band gap of 2D single layer ScO_2 (in T-structure), NiO_2 (in T-structure) and WO_2 (H-structure) compounds with U-J. The exchange term J is taken to be 1 eV.

from 5d-orbitals are not affected seriously from LDA+U calculations. As for the question whether the stability of MO_2 compounds in H- or T-structure is affected after LDA+U calculations is addressed by redoing the same phonon calculations with $U=5, 9$ and 12 eV. The stabilities of these compounds are maintained after LDA+U corrections.

4.5 MX_2 as a hydrogen evolution reaction (HER) candidate

Hydrogen evolution reaction (HER) is where protons get excess electrons and then chemically combine to form H_2 molecule. This reaction takes place at the last step after the split of water into its constituent atoms. Hinnemann *et al.*[27] recently reported that MoS_2 can be a good candidate for HER by observing plants's hydrogenase and nitrogenase enzymes. Active edges of MoS_2 nanoparticles were the place where HER takes place. The edges of nanoparticles are like Mo dominated edges of zigzag nanoribbons where consecutive edge Mo atoms are terminated by an excess S atom lying in the same plane as Mo atoms. Upon the adsorption of H atom to excess S atoms, their planar structure is disturbed and at the edges, S atoms are buckled as shown in Fig. 4.9. Since only this edge is HER active side, we modeled HER in a supercell consisting of four zigzag nanoribbons where $n = 6$ (number of M- X_2 basis in the unitcell.). In this section calculations include van der Waals interaction[44] and exchange correlation functional

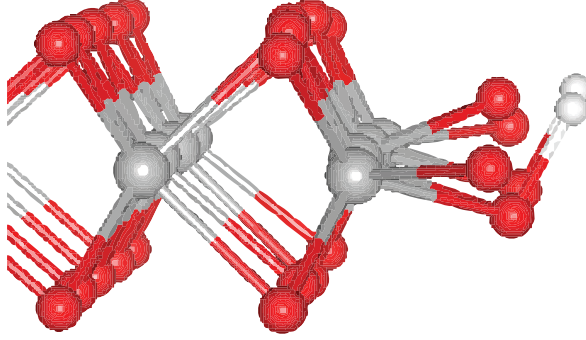


Figure 4.9: Geometric structure after two hydrogen adsorption to S monomer terminated Mo edge of zigzag nanoribbon.

is represented by the Generalized Gradient Approximation (GGA) characterized by Perdew-Burke-Ernzerhof[237] (PBE).

In previous sections we found that electronic and magnetic properties of 1H-MoS₂ is very similar to those of MX₂ structures where M=Cr, Mo, W and X=S, Se, Te. Since structures based on MoX₂ and WX₂ are recently synthesized,[74] we skipped compounds including Cr as a transition metal. We first calculated differential hydrogen chemisorption energy, ΔE_H which is $\Delta E_H = E_{\text{MoS}_2+n\text{H}} - E_{\text{MoS}_2+(n-1)\text{H}} - 1/2E_{\text{H}_2}$ where $E_{\text{MoS}_2+n\text{H}}$ is the total energy of MoS₂ nanoribbon with n hydrogen atoms are adsorbed at the active edge, $E_{\text{MoS}_2+(n-1)\text{H}}$ is the total energy of the nanoribbon with $(n - 1)$ hydrogen atoms are adsorbed and E_{H_2} is the total energy of hydrogen molecule. This energy defines the energy needed to increase the coverage of the active edge by one hydrogen atom. Since our calculations are carried on supercell containing 4 $n = 6$ zigzag nanoribbons, our supercell can adsorb up to 4 hydrogen atoms similar to the case in Hinnemann *et al.*[27] The calculated first and second hydrogen energies are indicated in Table 4.2. First hydrogen adsorption of MoS₂, MoSe₂ and second hydrogen adsorption to MoS₂ are energetically exothermic. (Hinnemann *et al.*[27] found the first and second differential hydrogen chemisorption energy as -0.62 and -0.21 eV because they did not include van der Waals interaction in their DFT calculations and they used different exchange correlation functional, RPBE.)

To clarify if the reaction is spontaneous or not, one has to calculate the Gibbs

Table 4.2: Calculated differential chemisorption energy ΔE_H (see the text) for the first hydrogen atom to the edge of MX_2 nanoribbons. Values in parenthesis are for the second hydrogen atom.

	MS_2	MSe_2	MTe_2
MoX_2	-0.84(-0.36)	-0.20(0.29)	0.10(0.42)
WX_2	0.08(0.34)	0.16(0.61)	0.35(0.69)

free energy of H adsorption to the active edges of zigzag nanoribbons. The DFT calculations do not include contributions from zero-point energies and entropy of the system. These should be calculated separately and added to hydrogen chemisorption energy. Gibbs free energy for hydrogen adsorption can be calculated as $\Delta G_H^0 = \Delta E_H + \Delta E_{ZPE} - T\Delta S_H$ where ΔS_H is the entropy difference between the adsorbed and the gas phase, ΔE_{ZPE} is the difference in zero point energy between the adsorbed and the gas phase and ΔE_H is the hydrogen chemisorption energy as indicated before. The energy contribution from the configurational and vibrational entropy is neglected as indicated earlier by Hinnemann *et al.*[27] The entropy of hydrogen adsorption can be taken as $\Delta S_H = 1/2S_{H_2}^0$ where $S_{H_2}^0$ is the entropy of H_2 at the gas phase.

The zero point energy of a system can be calculated as:

$$E_{ZPE} = -3Nk_B \int_0^\infty g(w) \ln w dw + 3Nk_B(1 + \ln k_B T) \quad (4.1)$$

where $g(w)$ is the phonon density of states of the system and w is the frequency. Calculation of phonon density of states of a supercell of nanoribbon without any symmetry is extremely difficult. One has to make at least $3N$ calculations (N is the atom number in the supercell of nanoribbon and each supercell consists of ~ 75 atoms) for a single case in each item in Table 4.2. Instead of doing the tons of calculations, Hinnemann *et al.*[27] reported that zero point energy contribution together with $T\Delta S_H$ is 0.29 eV for MoS_2 . We take this value as same for all the cases in other MX_2 structures since it depends mostly on the vibration frequencies of adsorbed H atom on similar chalcogen atoms. This means that $\Delta G_H^0 = \Delta E_H + 0.29$ eV. When energy values in Table 4.2 is carefully examined, gibbs free energy of first H atom adsorption to MoSe_2 and second H atom adsorption to MoS_2 results in energy values close to 0 eV. If gibbs free energy is negative or close to 0

eV, it can be said that the reaction is spontaneous and happens by itself. In this manner, not only MoS_2 , but also MoSe_2 can be a good candidate for HER.

4.6 Discussions

The unusual properties of graphene, single layer BN and MoS_2 discovered from recent studies have motivated us to explore 2D single layer structures of transition metal oxides and dichalcogenides, MX_2 compounds in honeycomb like structure. Three-dimensional crystals of these MX_2 compounds display diversity of properties, which have been the subject of several studies in the past. Recent studies have shown that 2D flakes of some of those MX_2 compounds synthesized by various techniques have properties, which can be of interest for various nanotechnology applications. MX_2 compounds has a large manifold, some members of it have layered crystals like graphite, which may allow exfoliation of single layers. We addressed the question which compounds among those large manifold can form stable and suspended single layer structures. We, in particular, were interested in two honeycomb like structures, namely H- and T-structures. We predicted 52 different individual components, which are stable in either H- and/or T-structures. Namely that these compounds can remain stable as free standing, once they are synthesized in one of these single layer structures. Our results are summarized in Fig. 4.10. Our predictions are based on state-of-the art first-principles calculations of structure optimization, phonon frequency, molecular dynamics and mechanical properties. Further to the extensive stability analysis, we investigated the electronic, magnetic and mechanical properties of those stable compounds. In addition to the optimized lattice constants and internal parameters we also calculated cohesive energies E_C , formation energies E_f , magnetic moments μ , the effective charges on M and X atoms and in-plane stiffness C . We noted various trends; generally not only band gap, but also cohesive energies, in-plane stiffness (also surface polarities of semiconductors due to charge transfers from M to X) which increase with decreasing row number of X. The lattice constants exhibit a reverse trend. Finally, we designate that WO_2 having highest cohesive energy, highest charge transfer from M to X, highest in-plane stiffness among MX_2 in this

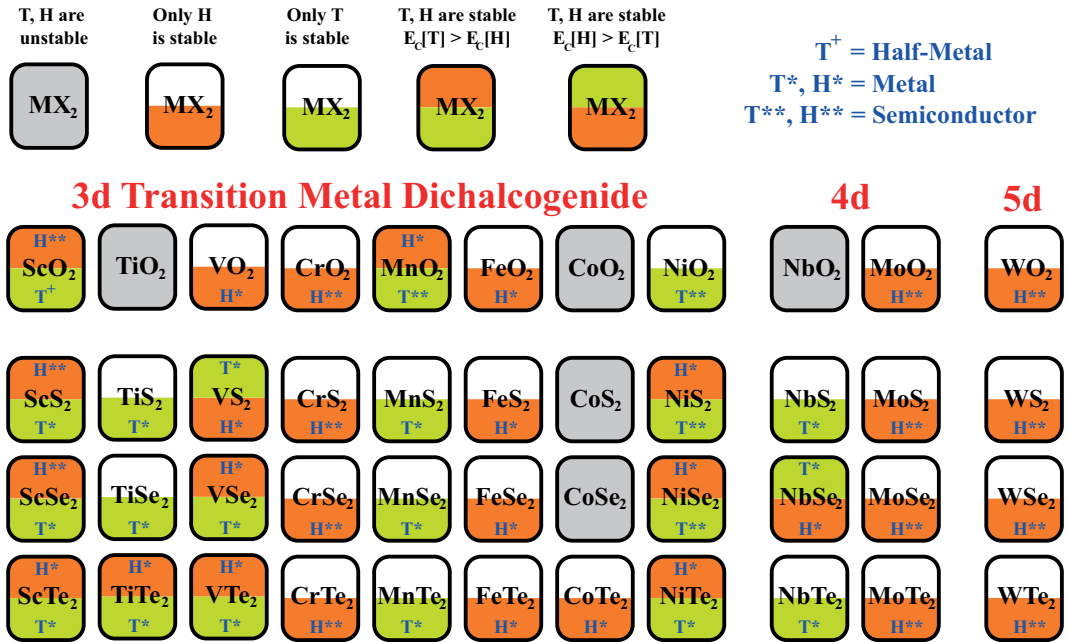


Figure 4.10: Summary of the results of our stability analysis comprising 44 different MX_2 compounds, which may form stable, 2D single layer H- and/or T-structures. Transition metal atoms indicated by M are divided into 3d, 4d and 5d groups. MX_2 compounds shaded light blue (gray) form neither stable H- nor T-structure. In each box the lower lying structure (H or T) has the ground state. The resulting structures (T or H) can be half-metallic (if specified by '+'), metallic (if specified by '*') or semiconductor (if specified by '**').

study heralds an important single layer material for future studies.

Chapter 5

Splitting of H₂O at the Vacancies of Single Layer MoS₂

5.1 Preliminary Information

The utilization of hydrogen as a clean and sustainable energy source critically depends on the efficient production of H₂ molecules. Since the reserves of free H₂ cannot occur in nature, hydrogen has been used as an energy carrier. Despite recent advances in developing high-capacity and safe hydrogen storage mediums using carbon based nanostructures based on Dewar-Kubas interactions[12, 238, 15, 8], the production of H₂ is still a major goal and an active research activity in hydrogen economy. Alkaline metals are also an attractive research field in H₂ storage due to low weight of metal atoms that physisorb H₂. [7, 238] By this way they can achieve higher storage capacities in terms of weight percentage.

After its first synthesis[21] 1H-MoS₂ flakes and nanoribbons have displayed unusual chemical and electronic properties.[5, 6, 1, 239] In particular, it is mechanically a stiff material.[1] In contrast to graphene, it is a semiconductor suitable for nanotransistor fabrication.[30] They can form multilayer structure due to weak van der Waals attraction. Direct-indirect band gap transition with number of layers leads to interesting photoluminescence properties.[24, 21] Because

of high stiffness of MoS₂, the stick-slip process in the sliding of 1H-MoS₂ coated surfaces is suppressed and ultralow friction is attained.[56, 26] Different types of defects, such as Mo-, S-vacancy, MoS- and S₂-divacancy, MoS₂-triple vacancy and reconstructed armchair and zigzag edges can occur in 1H-MoS₂. [5, 6] In Section 3.6.2, the calculated formation energies are high and one can expect very low concentrations. However, vacancy defects can still be generated by the recently developed new techniques.[153, 154, 155].

Active edges of MoS₂ nanoparticles were the subject of many studies.[240, 87, 96] This is because MoS₂ plays an important role in hydrogen evolution reaction (HER).[27] This reaction covers formation of H₂ molecule from positively charged H atoms. In plants, where analogue of HER is catalized by nitrogenase and hydrogenase enzymes. These enzymes include Mo and S atoms at their active sites. Hinnemann *et al.*[27] first carried out density functional theory calculations and predicted that active edges of MoS₂ nanoparticles are good HER candidate. They calculate gibbs free energy of reaction, ~ 0 eV at room temperature and experimented that H₂ molecule can be obtained from protons by transferring charge from MoS₂ active edges. Until then many researchers conducted experiments and theoretical calculations on HER properties of MoS₂. [241, 242, 243, 244, 245, 246, 247, 248]

The most probable production method of H₂ taking into account environmental concerns is using water and the sunlight. Two methods dominated in achieving this goal. First one includes photogeneration cells. In this type of photoelectrochemical reactions, electrolysis of water is taken place, when anode is shined by solar radiation. Semiconductor surfaces or in-solution metal complexes are used as to absorb solar energy and act like an electrode. Expensive platinum based electrodes and corrosion of semiconductor surfaces in contact with water are the down sides of this method.[17, 18] The later method, powder based photocatalytic reactions, offers a more efficient and cheap way of producing H₂. In this type, experimental setup only includes water and the photocatalyst to operate. There are two approaches to achieve H₂ and O₂ from H₂O molecule. First one is to develop a single photocatalyst to achieve the splitting of H₂O. The down side of this type is photocatalysts are generally requires high photon energies in

UV range.[18] (Ga_{1-x}Zn_x)(N_{1-x}O_x) photocatalyst powder,[249] Sr₂M₂O₇ (M = Nb and Ta) photocatalyses[250] are examples of this kind. The other type consists of two catalysts and a mediator. One catalyst is used for oxygen reduction reaction (where O²⁻ is reduced to O₂) and other one is used for HER. A mediator is used to transfer charges between these catalysts. Ru/SrTiO₃ powder for H and BiVO₄, WO₃ powder for O as photocatalyst[251, 252], TaON-based photocatalysts[249] are examples of this kind. Modification to mediator region is also actively studied.[252, 251] This way method is also known as 'Z-scheme photocatalysis'. HER and oxygen reduction reactions are taken place either in single or two photocatalysts. The undesired reformation of H₂O cannot be avoided in this method of H₂ production which lowers the efficiency significantly.

In this chapter, we present our systematic theoretical investigation on the splitting of water molecule to its constituents on vacancy defects of 1H-MoS₂. Here we show that a MoS₂ vacancy in a single layer MoS₂ honeycomb structure (which is specified as 1H-MoS₂) can split the water molecule into constituents O and 2H atoms. This process by itself is exothermic and spontaneous. Two crucial ingredients underlying this catalytic reaction are: (i) The electronegativity of Mo is slightly smaller than that of H (according to Pauling scale 2.16 and 2.20, respectively). (ii) The ionization energy of Mo is almost half of H (684 KJ/mole and 1312 KJ/mole, respectively). Split atoms O and H, in turn, are attached to four folded Mo and two folded S atoms surrounding the vacancy, respectively. The release of H₂ molecules from the surface can then be realized by a photocatalytic reaction taking place within the spectrum of visible light. It should be noted that in the present study H₂ molecule is directly obtained upon the splitting of H₂O without the risk of the reformation of water.

Present study reveals interesting results which enhances the importance of MoS₂ in future nanotechnologic devices. These include: (i) How and why only MoS di- and MoS₂ triple-vacancy defects split the water molecule. (ii) The investigation of the diffusion of hydrogen atom on, in and through 1H-MoS₂. (iii) Formation of H₂ molecule from diffusing two H atoms. (iv) Effects of second H₂O adsorption on MoS₂ triple-vacancy defects. (v) Energy concerns on water splitting. The reactions are spontaneous. Since monolayer of MoS₂ is recently

synthesized,[21] present results are crucial and affordable for further research on sustainable energy production.

5.2 Properties of vacancy defects on 1H-MoS₂

In the third section, it is reported that the vacancy defect in 2D graphene,[143, 144, 145, 146, 147] graphene nanoribbons,[148, 149] 2D graphane[150] and graphane nanoribbons[151] give rise to crucial changes in the electronic and magnetic structure. Recently Ataca *et al.*[5, 6] reported the effects of vacancy defects on monolayer and nanoribbons of MoS₂. They investigated five different types of vacancy defects, namely Mo-, S-vacancy, MoS-, S₂-divacancy and MoS₂-triple vacancy, which are formed in 2D 1H-MoS₂. Magnetically most of the vacancy defects created on 1H-MoS₂ are reported as nonmagnetic.[6] Only MoS₂ vacancy causes significant charge transfer around the vacancy and results in a magnetic moment of 2 μ_B . We carried out the same calculations in (4×4) supercell of 1H-MoS₂ with PBE functional and obtained the same magnetic properties. In addition to these, S₂-divacancy on the same surface of 1H-MoS₂ does not induce any magnetic properties.

5.3 Interaction of H₂O with perfect 1H-MoS₂ surface

According to Bader analysis, the effective charges on oxygen and hydrogen atoms of water molecule are -1.30 e +0.65 e, respectively. The same analysis results in effective charges of +1.0 e and -0.5 e on Mo and S atoms, respectively. In this respect, 1H-MoS₂ can be viewed as positively charged Mo-atomic plane sandwiched between two negatively charged S-planes. As a result, a repulsive interaction sets in between free H₂O and perfect surface of 1H-MoS₂. No matter

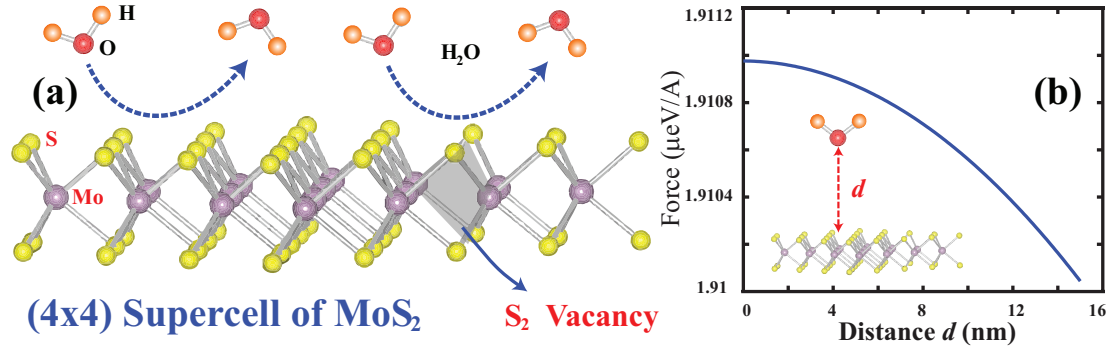


Figure 5.1: (a) Schematic representation of (4x4) supercell of single layer 1H-MoS₂. Purple and yellow balls are Mo and S atoms respectively. 1H-MoS₂ can be assumed as positively charged Mo hexagonal layer sandwiched between negatively charged hexagonal H layers. H₂O molecule is shown with red and orange balls, which are O and H atoms respectively. H₂ molecule does not bind to defectless (left side); S- and Mo- vacancy, S₂ di-vacancy (right side) defects on 1H-MoS₂. The case in S₂ di-vacancy is shown. (b) Plot of variation of repulsive Coulomb force between defectless 1H-MoS₂ and H₂O.

what its initial orientation is, H₂O first rotates so as two H atoms face the negatively charged S-plane and subsequently it is repelled as shown in the left hand side of Fig. 5.1 (a). To prove if this is resulted mainly from Coulomb repulsion, we make simulations by assuming that Mo, S atoms are positively and negatively charged point charges, respectively. Taking into account the Coulomb interaction of neighboring 1500 MoS₂ unitcell, we calculated the force acting on H₂O by varying the distance from 1H-MoS₂ surface. The force versus distance plot is shown in Fig. 5.1 (b). The force is repulsive and as H₂O drifts far away, the repulsive force vanishes. Gauss's Law in Electrodynamics is obeyed at distances in micro meters range.

5.4 Interaction of H₂O at vacancy defects of 1H-MoS₂

5.4.1 S-, Mo- vacancy and S₂- divacancy defects

In order for a water molecule to interact with MoS₂, there must be a gap on the negatively charged S layer region. One can obtain this via creating vacancy defects on 1H-MoS₂. In case of S- and S₂ (*i.e.* Single S atom vacancy at each surface) di-vacancies, Mo atoms neighboring the vacancy have slightly less positive charge. This does not affect the magnetic property. They prefer to give more charge to remaining nearby S atoms. For this reason, the change in the strong negatively charged region on S-layer does not influence much. Single Mo vacancy defects again do not influence significant change in the charge distribution on S layers. More charge is transferred from the neighboring six-fold Mo atoms to compensate the missing bond. In addition to these, there is no atomic discontinuity on S-layer. When a water molecule is placed ~ 2 above S-plane close to the vacancy region, the water molecule still repelled from the surface. The trajectory of the H₂O on the right hand side of Fig. 5.1 (a) does not influence S₂ vacancy defects.

However increasing the S vacancy defect size on the same surface of 1H-MoS₂ can create a region where water molecule can interact with Mo-layer. Even if the vacancy of two adjacent S atoms in the same S-plane allows H₂O to engage in an attractive interaction and to be bound to Mo atom, the configuration of the water molecule remains intact owing to its weak binding of 0.59 eV. In order to check if this binding is strong enough in room temperatures, we carried out molecular dynamics simulations at 300 K. Time step is taken as 1 fsec and the velocities of atoms are normalized in every 40 steps. For 10000 time steps, the water molecule did not release from the S₂ di-vacancy.

5.4.2 MoS- di and MoS_2 triple vacancy defects

The role of Mo in MoS_2 is to supply electrons (according to Bader analysis Mo is +1 electrons positively charged) to S atoms similar to H atoms in water. Electronegativity of Mo and H atoms are very close to each other (2.16 and 2.20 according to Pauling scaling, respectively) in addition, however first ionization energy of Mo is half of that of H (684 and 1312 kJ/mole, respectively). In this manner Mo atom can take the place of H atom when it forms a bond with oxygen. In S and both S_2 vacancies, Mo atoms compensate the vacancy by giving more electrons to nearest S atoms and conserve their positive charge. For this reason, Mo atom does not interact with oxygen of water strongly. However in the case of MoS di- and MoS_2 triple-vacancy, there two Mo atoms having dangling bonds inside the vacancy region. When H_2O molecule is trapped in these vacancies, one expects Mo atoms interacting and supplying electrons to oxygen of water molecule. Hence it can break O-H bonding, which is energetically not favorable any more.

Initially, H_2O molecule is trapped in the vacancy by forming bonds with both four folded Mo atoms each having two dangling bonds due to missing S_2 . Once bound, O atom of H_2O transfers electrons from Mo atom and subsequently one H atom is released to be attached to one of S atoms at the close proximity as described in Figure 1 (b). At the end, the total energy is lowered by 2.85 eV (relative to the energy of free H_2O and 1H- MoS_2 with a MoS_2 vacancy, i.e. relative to Figure 1 (a)) and the effective charge on Mo increases to +1.15 e. This exothermic process occurs spontaneously without an energy barrier and is precursor to other states presented in Fig. 5.2, which lower the total energy further. To verify the spontaneity of the reaction, extra test calculations are carried out. Starting with an initial MoS_2 vacant 1H- MoS_2 and H_2O molecule, in the first method we placed H_2O molecule ~ 3 away from the S-layer of 1H- MoS_2 and carried out geometry optimization. Similar results are obtained. H_2O molecule trapped into the vacancy and splitted. In the second method we carried

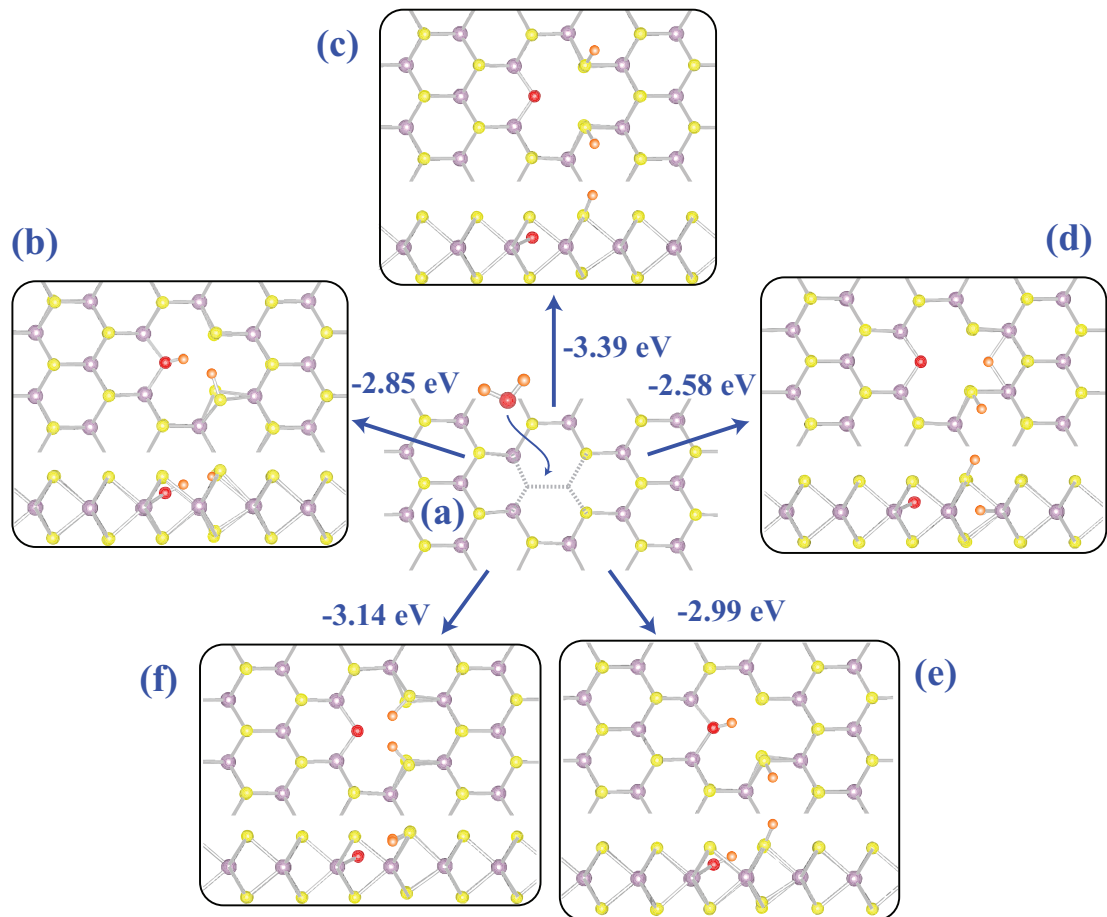


Figure 5.2: Splitting of water molecule trapped in a MoS_2 triple-vacancy of 1H- MoS_2 . (a) A free H_2O is approaching towards the MoS_2 triple-vacancy. Purple, yellow, red and orange balls indicate Mo, S, O and H atoms, respectively. (b) The precursor state occurs upon structure optimization and leads to the spontaneous splitting of H_2O into OH and H in an exothermic process. This state has the total energy, which is -2.85 eV lower relative to (a). (c) The most energetic (lowest energy) state, which occurred through ab-initio MD calculations at $T=1000$ K initiating from (b), where H atom is split from OH and is adsorbed to a two-folded S atom surrounding the vacancy leaving behind O atom adsorbed to two four-folded Mo atoms. This state has -3.39 eV energy relative to (a). (d), (e) and (f) are other intermediate states, which occur in the course of ab-initio MD calculation. Each panel presents both top and side views of atomic configurations.

out molecular dynamics simulations at various temperatures and different time steps. These include T=50 and 300 K, 0.5 fsec as a time step interval. In both calculations in between 10000 time steps, water molecule first came close to the triple-vacancy, trapped in and splitted.

We also carried out ab-initio molecular dynamics (MD) calculations to geometry optimized structure in Fig. 5.2(b) at T=1000 K by normalizing the velocities after every 40 time steps. The simulation temperature is taken high to speed up the statistics. Further to the atomic configuration in Fig. 5.2 (b) attained through the structure optimization based on conjugate gradient, four different binding configurations described in Fig. 5.2 (c)-(f) are revealed at different intermediate stages of MD calculations. These configurations correspond to different minima in Born-Oppenheimer surface. Remarkably, the configuration in Fig. 5.2 (c) corresponds to minimum energy configuration (i.e. $E=-3.39$ eV relative Fig. 5.2 (a)), where H₂O is completely split into O which is adsorbed to two four folded Mo atoms and two H atoms which are adsorbed to two different two folded S atoms in the same S-plane. Transition state calculations finds an energy barriers of 99 meV and 218 meV to split H from OH in Fig. 5.2 (b) and to change to the configuration in Fig. 5.2 (f) and then to settle in Fig. 5.2 (c). Remaining three configurations correspond to water molecule, which is completely split as in Fig. 5.2 (c). In these configurations the Mo-O bond is ionic, where the effective charges on Mo and O +1.25 e and -0.90 e, respectively. As for the S-H bond, which is formed from the combination of *s*-orbital of H and *p_z*- and *p_x*- orbitals of S with transfer of ~ 0.1 e from H to S. A magnetic moment of $2\mu_B$ is attained due to unpaired electrons in these configurations. In addition to the states in Fig. 5.2 (b)-(f), H atoms can be bound also to Mo layer with relatively low binding energy.

5.4.3 Splitting of second H₂O in MoS₂ triple-vacancy

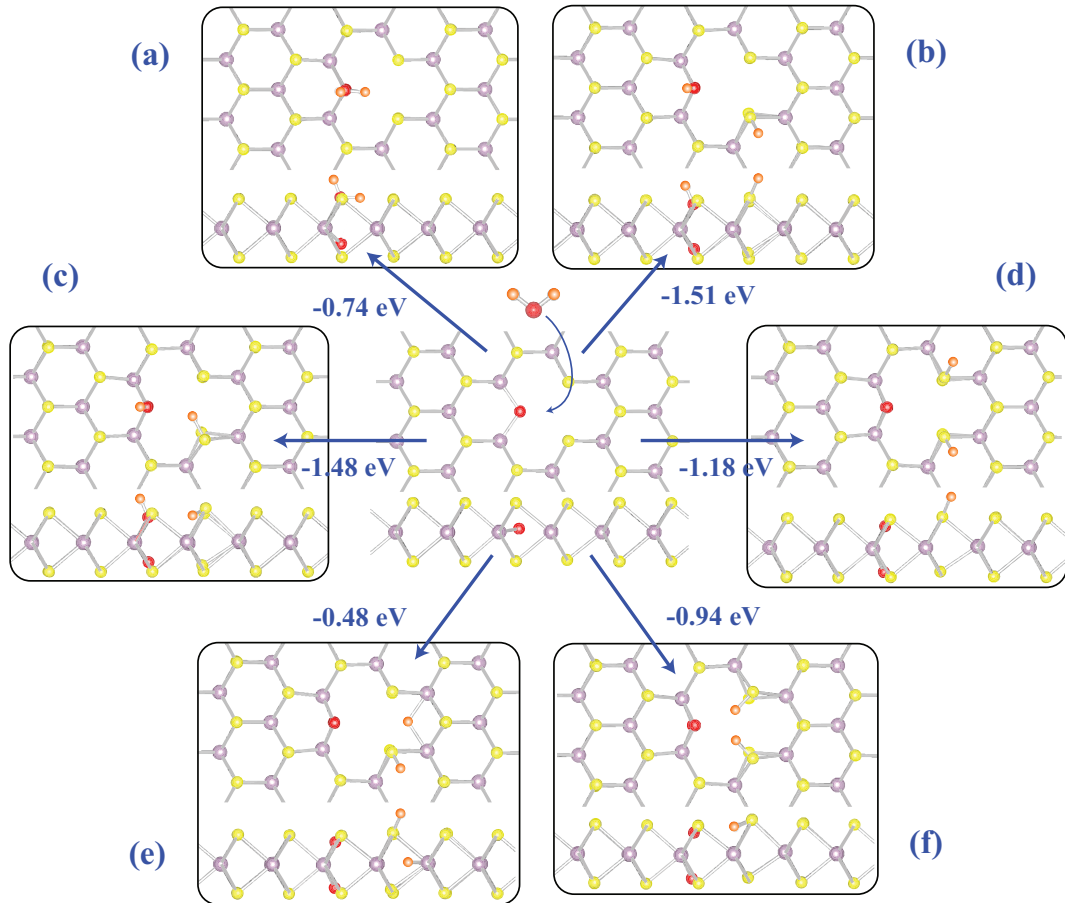


Figure 5.3: Splitting of second water molecule trapped in the same MoS_2 triple-vacancy in monolayer $1H-MoS_2$. In the middle of the hexagon, optimized structure of single O atom in MoS_2 triple-vacancy after the diffusion of two H atoms on $1H-MoS_2$ is shown together with approaching water molecule. Purple, yellow, red and white balls indicate Mo, S, O and H, respectively. When the water molecule is trapped in triple-vacancy, its relaxed geometric structure is indicated in (a). On the corners of hexagon, optimized geometric structures taken from molecular dynamics calculations are indicated. Upper figure in each rectangle is the top view whereas bottom part is the side view of H_2O+MoS_2+O complex. The negative energy values indicate how much energy is released upon trapping of H_2O molecule.

We showed that H₂O molecule can be trapped in MoS di- and MoS₂ triple-vacancy. Hydrogen atoms can then diffuse on 1H-MoS₂, form H₂ molecule and release from the surface which will be treated in the next section. What remains on the vacancy is oxygen atom bonded to the dangling bonds of two Mo atoms. Two molybdenum atoms on the edge of MoS di-vacancy are saturated by binding to five S and single O atoms. However in the case of MoS₂ triple-vacancy, there is still a probability it can be saturated with one more chalcogen atom to make six bonds. When an extra water molecule is placed close to the vacancy region, geometry optimization calculations resulted H₂O molecule is bounded to two Mo atoms with a binding energy of 0.74 eV. The molecular structure of water molecule is not destroyed as shown in Fig. 5.3(a). Even though this structure is energetically favorable, molecular dynamics simulations carried out on this structure at T=300 K and 1 femto second time interval steps for 10000 steps showed that there are few other energetically more favorable structures needed to be considered. This indicates that there is small energy barrier in order for the second H₂O molecule to split into its constituents.

Earlier, we reported that when a single oxygen atom bonded to dangling bonds of two Mo, oxygen atom is negatively charged by -0.9 electrons and each Mo atom is +1.25 electrons positively charged since Mo atoms are also giving electrons to other four neighboring S atoms. In the case of second O adsorption to this geometry, each O and Mo is 1.5 electrons positively and -0.8 electrons negatively charged, respectively according to the Bader charge analysis. The second ionization energy of Mo atom is 1560 kJ/mole which is greater than hydrogen's first ionization (1312 kJ/mole) energy. This time hydrogen atom supplying excess charge to oxygen atoms is energetically more favorable which was the opposite case in the first H₂O adsorption. For this reason in Fig. 5.3 from various geometric structure, the most favorable ones include OH adsorption to dangling bonds of Mo atoms (see Fig. 5.3(b) and (c)). This is also the case in MoS vacancy defect. Instead of 4 S and 2 O atoms are binding to two Mo atoms in the vacancy region, Mo atoms binds 5 S and a single O atom as chalcogen atoms. The binding energy of H to O atom is 3.42 eV which is very high to break. Since splitted single hydrogen atom prefers to bind on S-layer, it can diffuse, combine

with other diffusing hydrogen atoms and release a H₂ molecule.

5.5 Diffusion of H atoms on 1H-MoS₂

5.5.1 Binding of H, O, and OH

In Figure 5.4 we show important charge density counterplots. These are two different adsorption geometries of H adatom, O and OH adsorption to dangling bonds of Mo atoms. Hydrogen adatom can bound to MoS₂ from Mo-Layer and on S-Layer which are already observed in the splitting of H₂). Even though there is a barrier in order for a H atom to adsorb at Mo-Layer which will be discussed in the next subsection, the binding energy is significantly large. The binding energy E_b is calculated as $E_b = -E_{MoS_2+H} + E_{MoS_2} + E_H$ where E_{MoS_2+H} is the total energy of MoS₂ and H adatom system, E_H is the total energy of free H and E_{MoS_2} is the total energy of 1H-MoS₂ calculated in the same supercell dimension. The binding energy of H atom adsorbed at the middle of hexagon (hollow site, HL) in Mo-layer is calculated as $E_b = 0.60$ eV. In Figure 5.4(a), the counterplots are showing strong H-Mo atom bonds. These are mainly contributed from planar d orbitals (d_{xy} and $d_{x^2+y^2}$) of Mo atoms and H s orbitals. In addition to these H adatom transfers excess charge (~ 0.20 electrons) from neighboring Mo atoms, since its electronegativity is greater than that of Mo. The magnetic moment of $1\mu_B$ is contributed not only from H adatom, but also neighboring Mo atoms.

In Figure 5.4(b), the energetically most favorable adsorption geometry of H adatom is indicated. H adatom is close to the top of S perturbed in a direction close to HL site, 1.4 Å away from the nearest sulphur atom, GM site. In this geometric configuration the binding energy is calculated as $E_b = 0.78$ eV. The bonding between S and H atoms are resulted from the combination of H atom's s orbital together with S atoms p_z and p_x orbitals. According to Bader analysis,

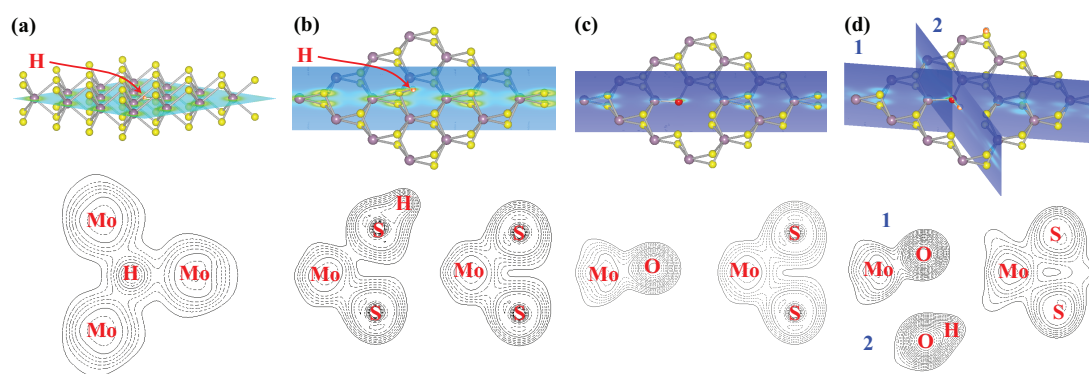


Figure 5.4: Counterplots of total charge density of H, O and OH adsorption geometries. There are two sites where H adatom can be adsorbed with a positive binding energy. (a) Adsorption geometry and counterplot of total charge density on a plane passing through Mo atoms and H adatoms. Hydrogen adatom is adsorbed on Mo-layer. (b) Similar to (a), but the adatom is adsorbed at GM site. (c) Adsorption geometry and counter plot of total charge density of O adatom on MoS₂ tri-vacancy. (d) Adsorption geometry and counter plot of total charge density of OH molecule on MoS₂ tri-vacancy. Counterplots are drawn on two different planes. One covering Mo-O bond and O-H bond. A plane shown in every adsorption geometry indicates in which plane counterplots of total charge density is plotted. Purple, yellow, red and white balls are Mo, S, O and H, respectively.

the charge of H adatom is slightly positive (+0.01 electrons), but the charge fluctuation between neighboring S and Mo atoms result in the magnetic moment of the system. The magnetic moment of $1\mu_B$ arises from H and d_{xz} and d_{z^2} of neighboring Mo atoms. When both adsorption geometries of H adatom compared, one expects that the configuration given in Fig. 5.2(d) must not be the energetically favorable since H adatom prefers to bind at S-layer.

In Figure 5.4(c) and (d), we investigate the binding mechanism of O and OH to dangling bonds of two Mo atoms. When single O binds with neighboring Mo atoms, the charge of O atom is calculated as -0.9 electrons. This charge is transferred from Mo atoms and in this configuration they are positively charged by +1.25 electrons. The strong bond ($E_b = 10.95$ eV per two Mo-O bonds) between O and Mo atoms dominate from the interaction between p_x, p_y orbitals of O and $d_{xy}, d_{x^2+y^2}$ orbitals of Mo atoms. The magnetic moment of $2\mu_B$ still exists and rise from dangling bonds of S atoms and d_{z^2}, d_{xz} and d_{yz} orbitals of Mo atoms on the edges of triple vacancy region. In the case of OH binding as shown in Fig. 5.4(d) Mo atoms supply less excess charge, however H atom supplies extra charge to O. As a result O atom is more negatively charged than previous case. Mo-O bonds consists of $d_{xz}, d_{yz}, d_{x^2+y^2}$ orbitals of Mo and p_x, p_y orbitals of O. O-H bond however dominated by p_z, p_x orbitals of O and s orbital of H atom.

When energetics of different H and O bonds are compared in the view of Fig. 5.2 and Fig. 5.3, one can state that single O binding to the dangling bonds of Mo atoms are energetically more favorable. This is due to the fact that ionization energy of Mo atoms are half of that of H. In other words, electron transfer from H atom is energetically costly when compared with Mo atom. H atoms prefers to be adsorbed on S layer. In the view of these, the energetically most favorable configuration is Fig. 5.2(c) where there are two surface H atoms. In the case of the second H₂O adsorption, the second ionization energy of Mo is higher than first ionization energy of H. For this reason, it is more favorable for O to transfer part of its excess charge of H atoms. Most energetic configuration include OH binding to the remaining dangling bond of Mo atoms, and a release of H atom adsorbed to two-folded S atoms.

5.5.2 Single H diffusion

Since 1H-MoS₂ consists of Mo hexagonal layer sandwiched between two hexagonal S layer and H adatom prefers to bind at both layers, we have three different diffusion routes. In Figure 5.5 we shown the energetics and paths of diffusion for each cases. If hydrogen atom is adsorbed on S layer, it can diffuse on the surface, however if H adatom is bonded to Mo layer, it can either diffuse in between Mo layer or diffuse to surface. In Figure 5.5(a) we show the energetics on adatom adsorption on S-layer. The highly symmetric adsorption geometries include hollow (HL, in the middle of hexagon on S-layer), bridge (B, in the middle of top of Mo-S bond), on top of S and Mo. In these calculations, the x and y coordinates of adatom is kept fixed and its height z together with all atomic positions of 1H-MoS₂ are optimized. The paths we follow include HL to on top of S, on top of S to on top of Mo, on top of Mo to hollow, hollow to bridge and bridge to geometric minimum (GM configuration). On going from HL to S site, we pass over GM site. Mo and HL sites are not energetically favorable and bridge site is the most favorable geometry for a hydrogen atom to pass through neighboring hexagons. There is a barrier along the path between HL and T=Mo of energy $\Delta Q_1 = 0.31$ eV. Hence, an open path, on which H atom can migrate for a long distance has to overcome ΔQ_1 by not passing from nearest bridge sites. Note that a slightly lower barrier of $\Delta Q_2 = 0.25$ eV supports only a closed path, which can circulate only among adjacent hexagons. In the middle of Fig. 5.5(a), we indicate the diffusion path of H atom initially at GM site to GM site in the neighboring hexagon.

In Figure 5.5(b) we modeled the diffusion of H initially adsorbed at Mo-layer to GM site on S-layer. In these calculations, height z of adatom is fixed whereas x and y coordinates of adatom together with atoms of 1H-MoS₂ is relaxed. Upon going from Mo-layer to S-layer, H adatom can be trapped in a local minima, where H adatom sits in between neighboring Mo and S atoms and makes bonding with them. The geometric structure is indicated in Fig. 5.5(b). In order for a hydrogen

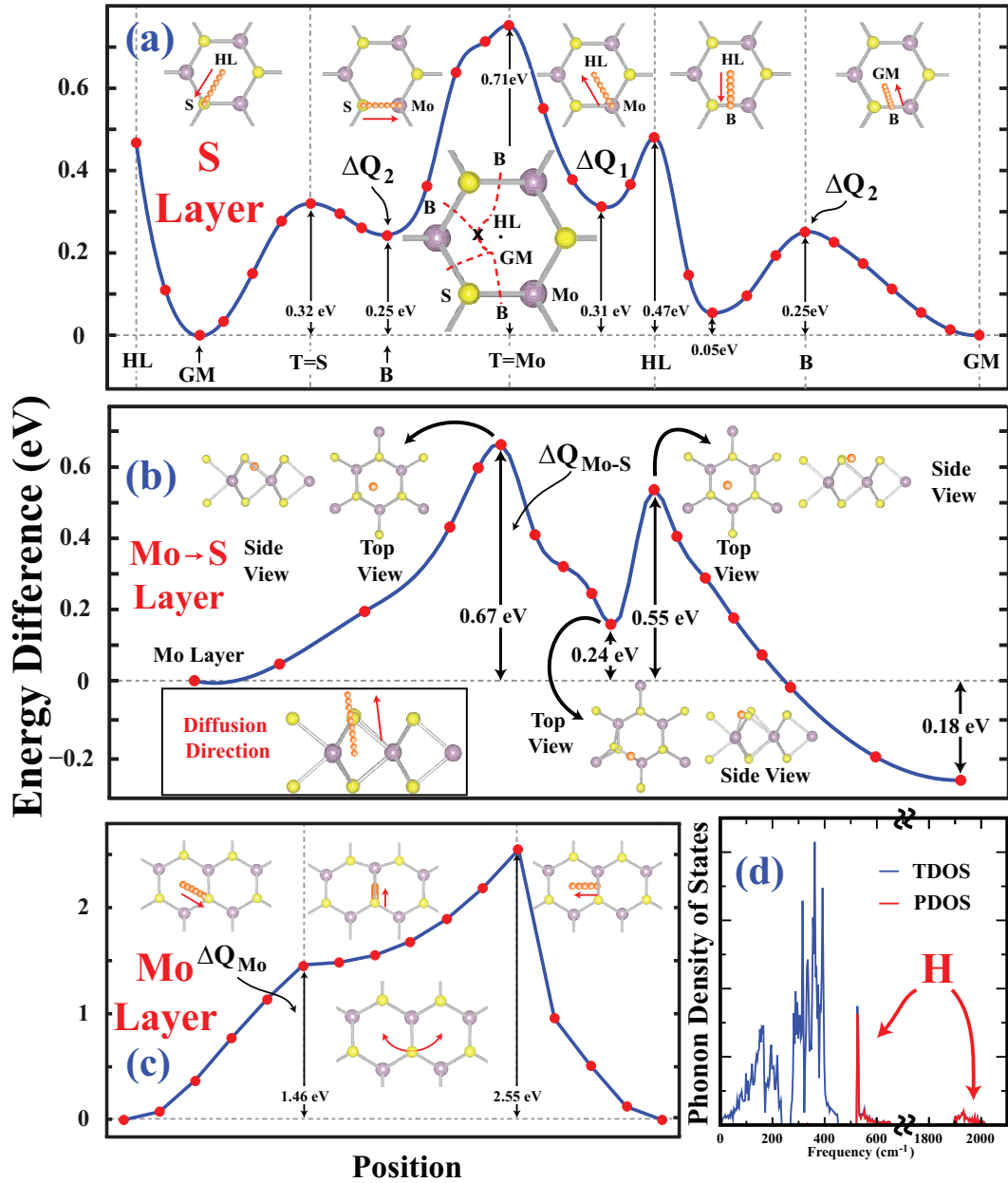


Figure 5.5: Energy variation of a single isolated hydrogen adatom, H, moving along the special directions of 1H-MoS₂ honeycomb structure. (a) Each red dot corresponds to the minimum total energy of H on 1H-MoS₂ surface at a fixed x- and y-lateral position, but its height z together with all atomic positions of 1H-MoS₂ are optimized. B, T, HL and GM indicate bridge, top (of S and Mo), hollow and geometric minimum sites, respectively. The migration path of a single H is shown by dashed red lines on honeycomb. Relevant energy barriers are indicated by ΔQ_1 (occurs between HL-T=Mo indicated by 'x') and ΔQ_2 (occurs at B sites). (b) Similar to (a), but the diffusion direction is from Mo layer to S layer. Calculations are done in fixed z coordinate of H adatom whereas x- and y- coordinates of H together with all atoms of 1H-MoS₂ are relaxed. (c) Similar to (b), but the diffusion direction of H adatom is calculated on Mo layer of 1H-MoS₂. Purple, yellow and white balls indicate Mo, S and H atoms, respectively. (d) Total (TDOS) density of states of phonon frequencies of single H adsorbed on 1H-MoS₂. The density of states which is projected to the modes of H atom (PDOS).

adatom to diffuse from Mo layer to GM site at S layer, it has to pass over an energy barrier of 0.67 eV. However for vice versa, the diffusion barrier is 0.85 eV. Hydrogen adsorption on GM site on S-layer is energetically more favorable by 0.18 eV than that of in Mo-layer. In Figure 5.5(c) we modeled the diffusion of H adatom in Mo-layer. The highly symmetric paths we follow include hollow to S site, S site to bridge and bridge to hollow site in Mo layer. In order for a hydrogen atom diffuse between two HL sites in Mo layer, it prefers to pass from S site in Mo-layer with a barrier height of 1.46 eV. Diffusion of H atoms in Mo-layer is unlikely. To sum up all, H atoms prefer to diffuse on S-layer, however if they are trapped in Mo-layer, they will move up or down to either S-layers in order to diffuse. The energy barrier in diffusion at Mo-layer much higher than others.

We now focus ourself to the most likely process of diffusion on the outer S-plane and estimate the characteristic jump frequency ν from phonon calculations. Using the density of phonon states, which are projected to the modes of H atoms in Fig. 5.5 (d) we estimate $\nu \sim 600 \text{ cm}^{-1}$. Then, the diffusion constant $D = \nu a^2 \exp(-\Delta Q/k_B T)$ on the S-plane is obtained to be $1.21 \times 10^{-7} (4.55 \times 10^{-5}) \text{ cm}^2/\text{sec}$, which indicates a high diffusion rate even at room temperature (600 K).

5.5.3 Interaction of two hydrogen on 1H-MoS₂ surface

On 1H-MoS₂ surface, H₂ molecule can not bind. Even when one places hydrogen molecule ~ 2 close to S-layer, upon geometry relaxation, molecule is repelled from the surface. In the previous subsection we also show that the minimum diffusion barrier of hydrogen atom occurs on S-layer and is 0.31 eV. In this subsection we carried out calculations and tried to model what happens when two separate hydrogen atoms diffuse and come closer to each other. In Figure 5.6 balls shown with orange color indicate hydrogen atoms relaxed only in z- direction. Blue ball is the second hydrogen atom, but together with all 1H-MoS₂ atoms, it is fully relaxed. Up to a threshold distance, orange and blue hydrogen atoms do not interact in the geometry optimization calculations in (4×4) supercell. Diffusion barrier passing from bridge site and neighboring GM sites are calculated as 0.25

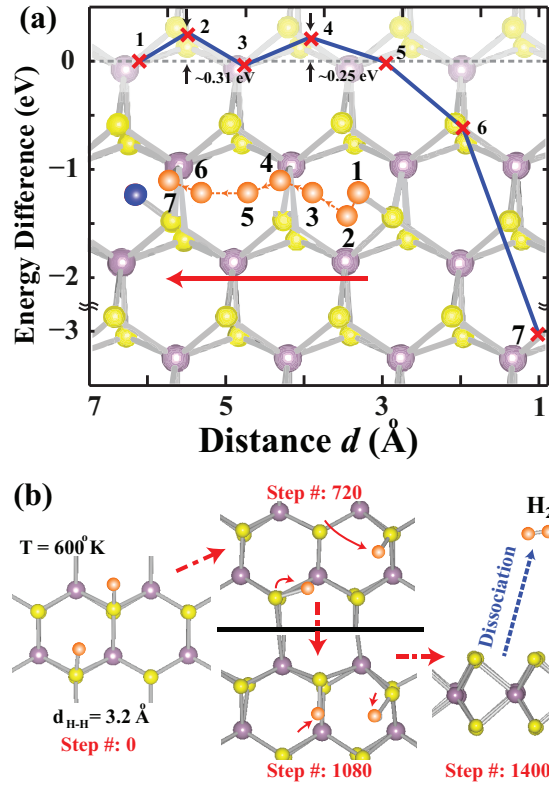


Figure 5.6: (a) The interaction energy between two hydrogen adatoms on 1H-MoS₂; one is initially adsorbed at GM site (shown by blue ball) on the surface, the other (shown by an orange ball) moves on the path of minimum energy barrier. Within the adatom-adatom distance of 1.97 Å H adatoms begin to interact. At the end both adatoms on 1H-MoS₂ form H₂ molecule and release from the surface. Purple and yellow balls are Mo and S atoms, respectively. (b) Relevant atomic structures corresponding to some intermediate steps of ab-initio molecular dynamics calculations at $T = 600$ K. Initial distance between hydrogen atoms is taken as $d_{H-H} = 3.2$ Å longer than the threshold distance.

and 0.31 eV, respectively. When the distance between H atoms are smaller than ~ 2 , they begin to interact with each other and if the distance further decrease, both H form hydrogen molecule and are released from 1H- MoS_2 surface. In this case, the system is energetically 2.90 eV favorable than two hydrogen atoms adsorbed on 1H- MoS_2 having distance greater than the threshold value. To check if the energy value we obtain is correct, we also calculate the cohesive energy of H_2 as 4.46 eV. The binding of H to S-layer is 0.78 eV. In order to break H-H bond in vacuum we have to supply 4.46 eV, but when both H atoms adsorbed on 1H- MoS_2 surface, they will release 1.56 eV. As a result the energy difference between the initial and final states is 2.90 eV which is the same as what we calculated with other method. In addition to these, we carried out molecular dynamics simulations at $T=600$ K and $T=1000$ K with 1 fsec time step. In both cases even initial H-H distance is ~ 3 which is greater than the threshold value, both H atoms diffused on the 1H- MoS_2 surface, made a hydrogen molecule and released from the surface. Geometric structures of some middle steps are indicated in Fig. 5.6(b). These indicate that two hydrogen atoms on the most favorable H_2O adsorbed geometry, i.e. Fig. 5.2(a), can diffuse on 1H- MoS_2 and form H_2 molecule without any need for additional catalytic reaction. These reactions are spontaneous and release ~ 1.50 eV of energy after each H_2 formation.

5.5.4 Can Hydrogen Tunnel between neighboring hexagons of 1H- MoS_2

Hydrogen atom can be treated as a quantum particle.[253] In this section we analytically solved the Schrodinger equation for the potential barrier found in the previous section. We took the mass of the particle as the mass of hydrogen atom. Even in particle in a box problem, where walls of the box assumed have infinite potential, the energy levels are inversely proportional with mass. Since mass of hydrogen is $\sim 10^4$ larger than that of electron's, one can expect many states in small energy levels. In Figure 5.7(a), we assumed that hydrogen atom diffuses

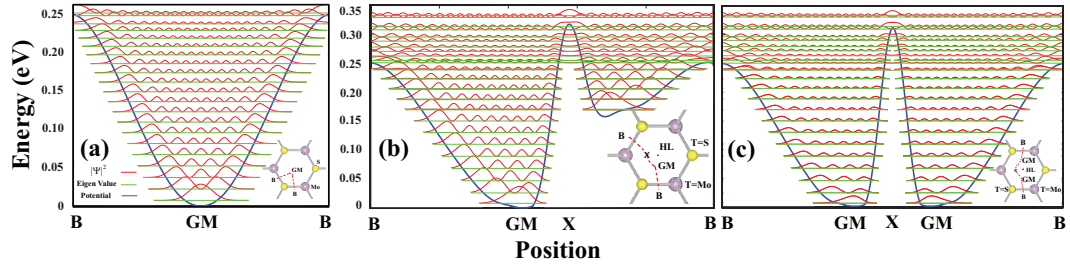


Figure 5.7: Analytical solution to periodic Schrodinger equation with a potential term taken as the diffusion barrier indicated in Fig. 5.5(a) In (a) the particle (proton) is assumed to be diffusing between the nearest bridge (B) sites and making cyclic motion around S atom. On (b) and (c) the most probable diffusion paths of H atom are considered and passing over the diffusion barrier occurring in between HL and T=Mo cites. The diffusion paths for each case are indicated on honeycombs at lower right corners, respectively. The white regions indicate the vanishing of $|\phi|^2$.

only through consecutive bridge cites and makes cyclic motion. Diffusion path considered is shown on lower right corner of Fig. 5.7(a). Tunneling of hydrogen atom around 0.25 eV potential barrier is only probable if one supplies ~ 0.24 eV to hydrogen atom. Otherwise the wave functions always vanish around the bridge cite.

In Figure 5.7(b) and (c) the most probable diffusion paths of H atom are considered and passing over the diffusion barrier of height 0.31 eV. A diffusing H enters the hexagon of MoS_2 from the bridge cite. Following the energy minimum path, it passes from GM cite. In order to diffuse in certain direction, it passes the energy minima in between HL and T=Mo sites, indicated as 'X' in Fig. 5.7 (b) and (c). At this point it can follow two different ways, one is to diffuse to the nearest bridge cite (the path shown lower right corner in Fig. 5.7 (b)) or to the nearest GM cite (the path shown lower right corner in Fig. 5.7 (c)). In the latter case the movement of H atom is symmetric around 'X' cite. Since the energy barrier ΔQ_1 is narrow, the probability of tunneling increases. As in the case in Fig. 5.7 (b) and (c), a H atom excited by 0.25 eV can diffuse from this barrier. Since the potential barrier between GM and bridge cites is wide, the tunneling probability decreases. In the case of diffusion, H atom having ~ 0.25 eV excess energy can diffuse over the bridge cite (passes from ΔQ_2) and tunnels over ΔQ_1

barrier.

In concluding this section we show that desorption of adsorbed H atoms from 1H-MoS₂ may follow different reaction paths: (i) Hydrogen atoms can desorb by the breaking of the S-H bonds from two folded S atoms surrounding the vacancy and eventually form H₂. In this photochemical process one needs photon energies $h\nu=2.90$ eV-3.08 eV, which lie at the maximum intensity range of visible light spectrum. (ii) While the S-H bonds surrounding the vacancy are broken (with a binding energy of 3.18 eV as in the case of H binding geometry in Fig. 5.2(c)), H atoms can be adsorbed to GM-site (i.e. geometric minimum site near the center of hexagon as shown in Fig. 5.5) with relatively weaker binding energy of 0.78 eV. Subsequently, these adsorbed H atoms diffuse readily on the surface of 1H-MoS₂. An attractive interaction sets in between two H atoms when they are within a threshold distance. Eventually these two H atoms form H₂ molecule by releasing 2.90 eV energy to the system. Owing to the weak repulsive interaction H₂ molecules are forced to escape from the surface. Through concerted processes this reaction path may require lower photon energy in the range $h\nu=2.12$ -2.30 eV which is also in the visible light range.

5.6 H₂O splitting on MoS₂ Nanoribbons and Other Transition Metal Dichalcogenides

Up to now our results are obtained from two dimensional infinite MoS₂ sheet. In reality, the reactions may take place on flakes and nanoribbons. The difference between infinite sheet and finite size MoS₂ sheets and nanoribbons are the edges which may inhibit or activate effects on the reaction. The active edges of MoS₂ flakes were the subject of interest[240, 87, 96] since it is reported that active edges play the crucial role in evolution reaction (HER).[27] The active edges are like Mo edges of zigzag nanoribbons[5] and extra S atom is adsorbed to Mo to form a bridge between consecutive edge atoms.

In order to model the effects of dimensionality in splitting of H₂O into its

constituents, we consider a zigzag nanoribbon consisting of 12 MoS₂ basis in the unitcell. As reported earlier by Ataca *et al.*[5], we take into consideration of reconstruction of S dominated edges by making calculations on supercell consisting of 4 unitcell in the direction of the nanoribbon. The structure of zigzag nanoribbon is shown in Fig. 5.8. The calculations carried out in the middle of the nanoribbon resulted that this part of the ribbon behaves similar to 1H-MoS₂. It repels H₂ and H₂O molecules as indicated in left side of Fig. 5.8. In the case of S, S₂, Mo vacancies, H₂O molecule does not split into its constituents and is repelled from the surface. MoS and MoS₂ vacancy defects result in the splitting of the water molecule similar to the geometries indicated in Fig. 5.2. The reconstructed edge consisting of S atoms does not play any role in HER and it is not an active and observed edge structure for flakes. For this reason they are not taken into consideration. Active edge structures a S atom forming bonds with two adjacent Mo atoms at the edge repel H₂O molecule as shown in Fig. 5.8. This is due to the fact that H₂O molecule can not make significant charge transfer from edge S atoms. In order for H₂O to make charge transfer with Mo atoms, we created a single S vacancy on S saturated Mo edge of the nanoribbon. In this case water molecule make a weak binding to the five-fold Mo atoms on the edge with a binding energy of 0.54 eV. In the case of bare edge where all the edge atoms are four folded Mo, the splitting of water does not take place. The dangling bonds of S atoms near the vacancy region in 1H-MoS₂ which create attractive field for H atom to help breaking strong OH bonds in water are absent in the edges of nanoribbons. Instead of splitting, water molecule tends to bind to the dangling bonds of Mo atoms from O edge. To sum up all, middle of the nanoribbon shows similar chemical atmosphere as 1H-MoS₂. The active edge structures in Mo dominated zigzag nanoribbons repel the water molecule, but bare edges results in the binding of water molecule from O edge to dangling bonds of four-folded Mo atoms.

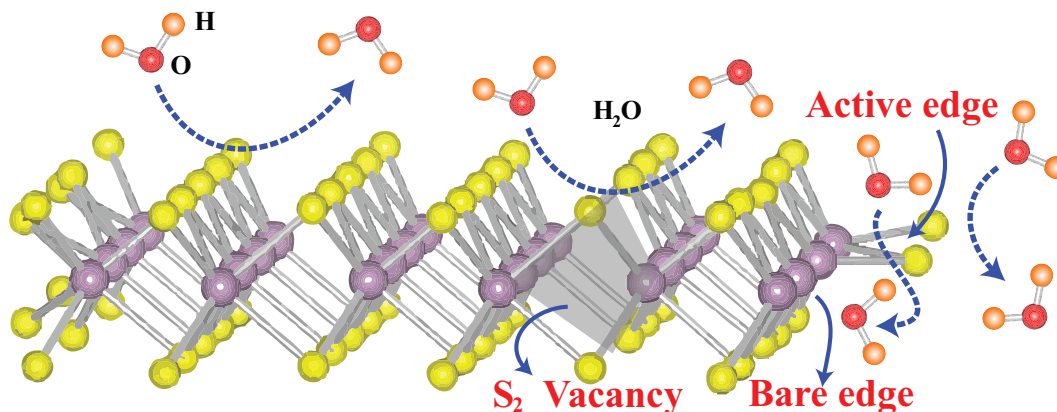


Figure 5.8: Zigzag edge MoS_2 nanoribbon with 12 MoS_2 basis in the unitcell. S edge reconstructions are allowed and the calculations are done in supercell consisting of 4 unitcells in the direction of the nanoribbon. On the right hand side, bare and active edge structures are indicated. H_2O molecule is repelled from the defectless, S, S_2 and Mo vacant regions in the middle and active edges of MoS_2 nanoribbon. MoS, MoS_2 vacancy defects result in splitting of water, bare Mo edge results in the binding of H_2O without splitting. Purple, yellow, red and orange balls are Mo, S, O and H atoms, respectively.

Theoretical investigations of Ataca *et al.*[239] predicting 52 stable honeycomb-like transition metal dichalcogenides let us think of whether there are other structures suitable for splitting of water. When work by Ataca *et al.*[239] is carefully examined, electronic, magnetic, elastic, structural and vibrational properties of MoS_2 are very similar with MX_2 (where M:Cr, Mo, W (transition metal); and X:S, Se, Te(chalcogen)). Having the same transition metal atom, but different chalcogen atom (increasing atomic number) result in a less charge transfer between transition metal and chalcogen atom. Similarly same chalcogen atom with different transition metal atom in the same group (increasing atomic number) results in a higher charge transfer in the bonding. In view of our findings in previous sections, if we can find a compound having first and second ionization energies comparable or smaller than Mo, and charge transfer in the M-X bond smaller than Mo-S bond (transition metal atom will supply excess electrons to O of H_2O), it would be more favorable to split water in the vacancies. In Table 5.1 we include the first and second ionization energies, electronegativity and electron affinity of H, O, Cr, Mo,W, S, Se. Among CrX_2 , MoX_2 and WX_2 , one can expect that Cr and Mo based structures will show similar effects on water splitting and

Table 5.1: First and second ionization energies, electronegativity and electron affinity of H, O, Cr, Mo, W, S, Se and Te for the search of other possible candidate structures of H₂O splitting.

Atom	1 st Ionization Energy kJ/mole	2 nd Ionization Energy kJ/mole	Electronegativity (Pauling Scale)	Electron Affinity kJ/mole
H	1312	-	2.20	72.8
O	1313.9	3388.3	3.44	141
S	999.6	2252	2.58	200
Se	941	2045	2.55	195
Te	869.3	1790	2.1	190.2
Cr	652.9	1590.6	1.66	64.3
Mo	684.3	1560	2.16	71.9
W	770	1700	2.36	78.6

are more favorable since ionization energies of W and charge transfer in W-X bond are higher. Since three dimensional structure of CrX₂ based compounds do not have hexagonal structure and two dimensional analogues are not synthesized, one has to wait for the experimental justification of these structures. Mo based few layer structures are recently synthesized.[74] It is worth studying water splitting on the vacancies of MoSe₂ and MoTe₂. We carried out calculations on MoSe₂ structure. Even though results of geometry relaxations suggests that H₂O is trapped in the MoSe₂ vacancy, splitting of H₂O does not occurred. Molecular dynamics calculations carried at 600 K presented that H₂O split into constituents as shown similar to Fig. 5.2 (c). The binding energy of H atom to both three folded and two folded Se atoms are smaller than those of S, which results in a smaller photon energy (~ 0.5 eV) requirement for the dissociation of H₂ molecule. Our work on the splitting of H₂O at the vacancy of MoSe₂ is in progress.

5.7 Discussions

Recently synthesized[21] and showing promising[30] properties for future nanotechnologic devices, 1H-MoS₂ can be assumed to be material of future and a contender of graphene. In this chapter, we focus our attention on the vacancy

defects on 1H-MoS₂ and their interaction with H₂O molecule. S, S₂-divacancy (each S vacancy is on each S-layer) repel water molecule due to negatively charged regions on S-layers. The water molecule can bind on the surface if there is S₂-divacancy formed from the absence of neighboring S atoms in the same S-layer. We demonstrated that a free water molecule is attracted by a MoS₂ vacancy of 1H-MoS₂ and is trapped in the hole. Concomitantly, H₂O is split into constituent atoms. While O remains to be bonded to the dangling bonds of Mo atoms around vacancy, H atoms are preferably attached to two folded S-atoms surrounding the vacancy. Another H₂O can also be trapped in the vacancy region. However splitting of H₂O to OH and H is observed due to less charge transfer from five-fold Mo atoms to O of H₂O. This is the case in H₂O trapping and splitting in MoS vacancy defects.

Subsequent to the splitting, H atoms bound to two folded S atoms can be transferred to GM-sites by photocatalytic reaction. Owing to a small energy barrier these H atoms diffuse readily and form H₂ molecule spontaneously. That the ionization energy of Mo is smaller than that of H, so that it donates electrons to O to free H atoms is crucial for the spontaneous splitting of water molecule. Tunneling of H atom is analytically analyzed. Since H is $\sim 10^4$ times heavier than electron, tunneling of H atom is only possible for very narrow energy barriers. Figure 5.9 summarizes all of the steps observed in splitting of H₂ in the vacancy defects of 1H-MoS₂

While advances in nanotechnology can provides us 1H-MoS₂ with high vacancy concentration, the removal of O bound to Mo through charging or other means can allow us to recyclable use of the same system. Because of exceptional properties similar to one revealed in this thesis, single layer MoS₂ honeycomb structure has been considered as the contender of graphene. As revealed from a recent study, several transition metal dichalcogenides form similar stable single layer honeycomb structures[239] and are potential candidates for similar catalytic reactions. The kinetics in the process above can be monitored by applied potential

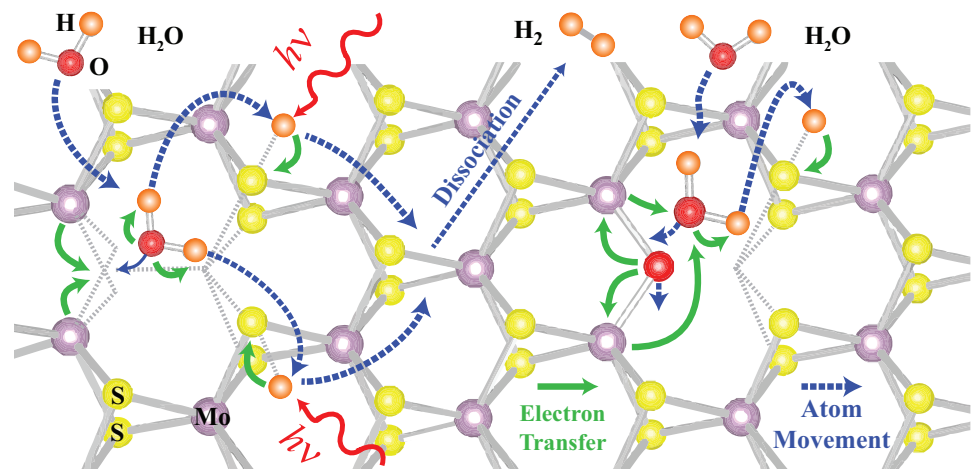


Figure 5.9: Schematic representation of H_2O splitting in the MoS_2 vacancy defects of 1H- MoS_2 . A H_2O is trapped and split in the vacancy defect. H atoms prefer to bind to two folded S atoms, where as O atom is strongly bind to four folded Mo atoms. By photon absorption, H atoms either releases or diffuses on 1H- MoS_2 surface. When H atoms are closer to each other than a threshold value, they combined and dissociated from 1H- MoS_2 surface. A second H_2O can also be trapped in the vacancy region. This time single H atom is released from H_2O molecule due to less charge transfer from five fold Mo atoms. Dissociation of H_2 is similar to previous case. Purple, yellow, red and orange balls are Mo, S, O and H atoms, respectively.

difference. We believe that the catalytic reaction predicted in this work heralds a sustainable and clean energy resource and will initiate several experimental studies.

Chapter 6

High Capacity H₂ Storage

6.1 Preliminary Information

Realization of fuel cells has been a turning point for a clean and efficient source of energy. Once hydrogen is chosen for a potential fuel of the future devices, one has to consider its reversible storage and discharging mechanisms. H₂ molecule can be stored in various methods. The easiest one is to store in pressured tanks. It takes energy to pump H₂ molecule to high pressure levels and in case of explosion, H₂ is flammable even though the product is water. The other methods include storage in low binding media.

Developing safe and efficient hydrogen storage is essential for hydrogen economy.[254] Recently, much effort has been devoted to engineer carbon based nanostructures[12, 13, 14, 15] which can absorb H₂ molecules with high storage capacity, but can release them easily in the course of consumption in fuel cells. Insufficient storage capacity, slow kinetics, poor reversibility and high dehydrogenation temperatures have been the main difficulties towards acceptable media for hydrogen storage. In this chapter we will present high capacity hydrogen storage on Li and Ca adatom adsorbed on graphene.

6.2 High-capacity hydrogen storage by metallized graphene

Adsorption of a single (isolated) Li atom on the hollow site of graphene (i.e. H1-site above the center of hexagon) is modelled by using (4×4) cell of graphene with 1.70 \AA minimum Li-graphene distance and with a minimum Li-Li distance of 9.77 \AA , resulting in a binding energy of $E_L=1.93 \text{ eV}$. Upon adsorption Li atom donates part of the charge of its $2s$ state to the more electronegative carbon atoms at its proximity. Despite the ambiguities in determining the atomic charge, Löwdin analysis estimates that Li becomes positively charged by donating $q \sim 0.35$ electrons (but $q \sim 0.9$ electrons according to Bader analysis[54]). The energy barrier to the diffusion of a single Li atom on the graphene sheet through top (on-top of carbon atoms) and bridge (above the carbon-carbon bond) sites are calculated to be $\Delta Q=0.35 \text{ eV}$ and 0.14 eV , respectively.

Lithium atoms can form a denser coverage on the graphene with a smaller Li-Li distance of 4.92 \AA forming the (2×2) pattern. Owing to the repulsive interaction between positively charged Li atoms, the binding energy of Li atom is smaller than that of the (4×4) cell. For H1 adsorption site (see Fig. 6.1(a)), the binding energy is calculated to be $E_L=0.86 \text{ eV}$. The binding energies are relatively smaller at the bridge and top sites, and are 0.58 and 0.56 eV , respectively. The binding energy of the second Li for the double sided adsorption with H1+H2 and H1+H3 configurations described in Fig. 6.1 (a), are $E_L=0.82$ and 0.84 eV , respectively. The same binding energies for H1+H2, and H1+H3 geometries on the (4×4) cell are relatively larger due to reduced repulsive Li-Li interaction, namely $E_L=1.40 \text{ eV}$ and 1.67 eV , respectively. The coverage of Li on the (2×2) cell is $\Theta=12.5 \%$ (i.e. one Li for every 8 carbon atoms) for H1 geometry and $\Theta=25 \%$ for either H1+H2 or H1+H3 geometries. Metallic charge accumulated between Li and graphene weakens the interaction between Li atoms which are adsorbed at different sites of graphene. Further increasing one-sided coverage of

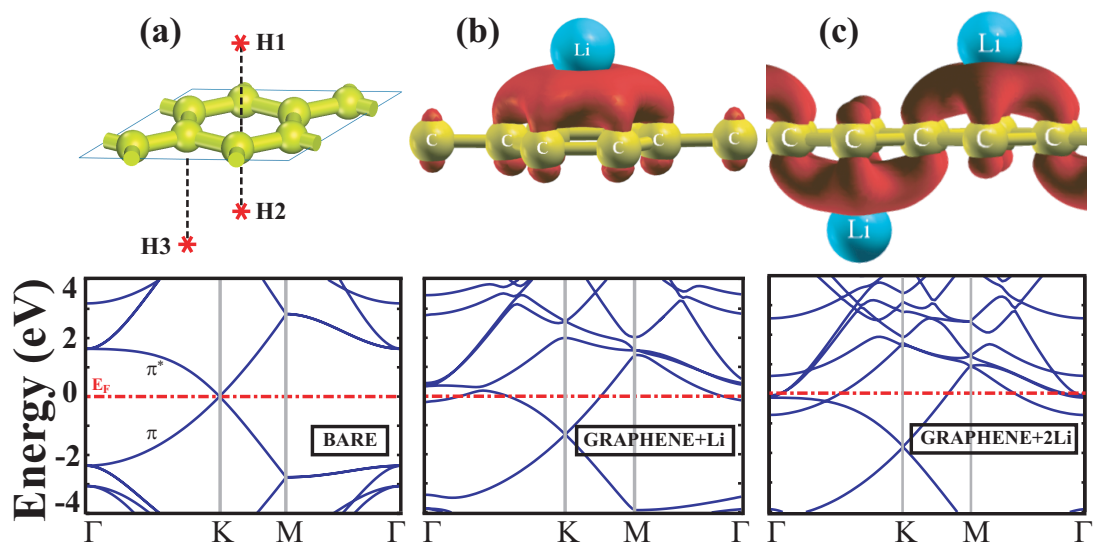


Figure 6.1: (a) Various adsorption sites H1, H2 and H3 on the (2x2) cell (top panel) and energy band structure of bare graphene folded to the (2x2) cell (bottom panel). (b) Charge accumulation, $\Delta\rho^+$, calculated for one Li atom adsorbed to a single site specified as H1 (top) and corresponding band structure. (c) Same as (b) for one Li atom adsorbed to H1-site, second Li adsorbed to H3-site of the (2x2) cell of graphene. Zero of band energy is set to the Fermi energy, E_F . Taken from Ataca *et al.*[7]

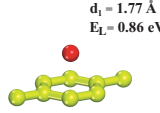
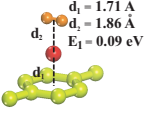
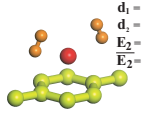
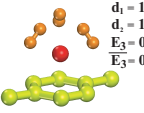
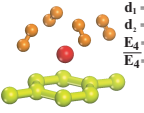
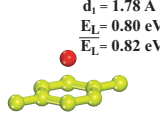
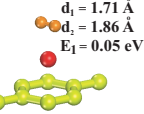
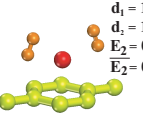
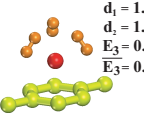
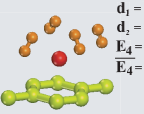
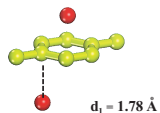
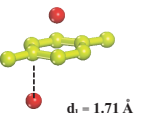
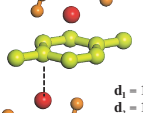
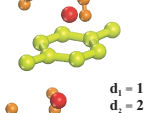
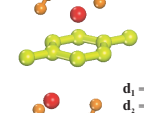
		n # of H ₂ per Li	1	2	3	4
ADSORPTION GEOMETRY	H1	 $d_1 = 1.77 \text{ \AA}$ $E_L = 0.86 \text{ eV}$	 $d_1 = 1.71 \text{ \AA}$ $d_2 = 1.86 \text{ \AA}$ $E_1 = 0.09 \text{ eV}$	 $d_1 = 1.80 \text{ \AA}$ $d_2 = 1.93 \text{ \AA}$ $E_2 = 0.36 \text{ eV}$ $\bar{E}_2 = 0.22 \text{ eV}$	 $d_1 = 1.72 \text{ \AA}$ $d_2 = 1.94 \text{ \AA}$ $E_3 = 0.17 \text{ eV}$ $\bar{E}_3 = 0.21 \text{ eV}$	 $d_1 = 1.72 \text{ \AA}$ $d_2 = 2.12 \text{ \AA}$ $E_4 = 0.18 \text{ eV}$ $\bar{E}_4 = 0.20 \text{ eV}$
	H1 + H2	 $d_1 = 1.78 \text{ \AA}$ $E_L = 0.80 \text{ eV}$ $\bar{E}_L = 0.82 \text{ eV}$	 $d_1 = 1.71 \text{ \AA}$ $d_2 = 1.86 \text{ \AA}$ $E_1 = 0.05 \text{ eV}$	 $d_1 = 1.70 \text{ \AA}$ $d_2 = 1.92 \text{ \AA}$ $E_2 = 0.41 \text{ eV}$ $\bar{E}_2 = 0.23 \text{ eV}$	 $d_1 = 1.74 \text{ \AA}$ $d_2 = 1.98 \text{ \AA}$ $E_3 = 0.18 \text{ eV}$ $\bar{E}_3 = 0.21 \text{ eV}$	 $d_1 = 1.82 \text{ \AA}$ $d_2 = 2.11 \text{ \AA}$ $E_4 = 0.19 \text{ eV}$ $\bar{E}_4 = 0.21 \text{ eV}$ $g_d = 12.8 \text{ wt \%}$
	H1 + H3	 $d_1 = 1.78 \text{ \AA}$ $E_L = 0.81 \text{ eV}$ $\bar{E}_L = 0.84 \text{ eV}$	 $d_1 = 1.71 \text{ \AA}$ $d_2 = 1.86 \text{ \AA}$ $E_1 = 0.07 \text{ eV}$	 $d_1 = 1.71 \text{ \AA}$ $d_2 = 1.90 \text{ \AA}$ $E_2 = 0.41 \text{ eV}$ $\bar{E}_2 = 0.24 \text{ eV}$	 $d_1 = 1.71 \text{ \AA}$ $d_2 = 2.15 \text{ \AA}$ $E_3 = 0.27 \text{ eV}$ $\bar{E}_3 = 0.25 \text{ eV}$	 $d_1 = 1.77 \text{ \AA}$ $E_4 = 0.05 \text{ eV}$ $\bar{E}_4 = 0.20 \text{ eV}$

Figure 6.2: Adsorption sites and energetics of Li adsorbed to the (2×2) cell of graphene and absorption of H₂ molecules by Li atoms. E_L is the binding energy of Li atom adsorbed to H1-site, which is a minimum energy site. For H1+H2 or H1+H3 configuration corresponding to double sided adsorption, E_L is the binding energy of second Li atom and \bar{E}_L is the average binding energy. For H1, H1+H2 and H1+H3 configurations, E_1 is the binding energy of the first H₂ absorbed by each Li atom; E_n ($n=2-4$) is the binding energy of the last n^{th} H₂ molecule absorbed by each Li atom; \bar{E}_n is the average binding energy of n H₂ molecules absorbed by a Li atom. Shaded panel indicates the most favorable H₂ absorption configuration. Taken from Ataca *et al.*[7]

Li to $\Theta=25\%$ with H1 geometry (or two-sided coverage to 50 % with H1+H2 or H1+H3 geometries) appears to be impossible due to strong Coulomb repulsion between adsorbed Li ions and results in a negative binding energy ($E_L \sim -2.5$ eV). On the other hand, the total binding energy of all Li atoms adsorbed on a (2×2) cell with the H1+H2 (H1+H3) geometry corresponding to $\Theta=25\%$ is 3.23 eV (3.12 eV) higher than that of Li atom adsorbed on the (4×4) cell with the same geometry corresponding to $\Theta=6.25\%$. Hence, since the cluster formation is hindered by the repulsive interaction between the adsorbed ions, a stable and uniform Li coverage on both sides of graphene up to $\Theta = 25\%$ can be attained.

The charge accumulation and band structure calculated for the H1 and H1+H3 adsorption geometries are presented in Fig. 6.1 (b) and (c), respectively. Isosurface plots of charge accumulation obtained by subtracting charge densities of Li and bare graphene from that of Li which is adsorbed to graphene, $\Delta\rho^+$, display positive values. As a result of Li adsorption, the charge donated by Li is accumulated between Li and graphene and is accommodated by $2p\pi^*$ -bonds of carbons. The empty π^* - bands become occupied and eventually get distorted. Occupation of distorted graphene- π^* bands gives rise to the metallization of semimetallic graphene sheets. By controlled Li coverage one can monitor the position of Fermi energy in the linear region of bands crossing at the K-point of the Brillouin zone. Metallization is also important for zigzag and armchair graphene nanoribbons, since both are semiconductors with their energy gaps depending strongly on the widths of these ribbons.[135] Segments of these ribbons metallized by Li adsorption may be interesting for their electronic and spintronic applications. For example, a junction of two nanoribbons with and without Li adsorbed segments can serve as a Schottky barrier.

Sodium, a heavier alkali metal, can be bound to graphene with $E_b=1.09$ eV at H1 site. However, the energy difference between top, bridge and H1 sites are minute due to relatively larger radius of Na. Upon adsorption, graphene and graphene nanoribbon are metallized. Nevertheless, Na is not suitable for hydrogen storage because of its heavier mass and very weak binding to H₂ molecules. Two dimensional BN-honeycomb structure, being as a possible alternative to graphene, has very weak binding to Li (~ 0.13 eV) and hence it is not suitable for hydrogen storage.

The absorption of H₂ molecules by Li + graphene in H1, H1+H2 and H1+H3 geometries. A summary of our results about the H₂ absorption are presented in Fig. 6.2. The binding energy of the first absorbed H₂, which prefers to be parallel to graphene, is generally small. However, when two or more H₂ molecules are absorbed by the same Li atom, the binding geometry and mechanism change and result in a relatively higher binding energy. All H₂ molecules are tilted so that one of two H atoms of each absorbed H₂ molecules becomes relatively closer to the Li atom. A weak ionic bond forms through a small amount change (~ 0.1 electrons)

transferred from Li and graphene to nearest H atoms of absorbed H₂ molecules. At the end, H atoms receiving charge from Li becomes negatively charged and the covalent H₂ bond becomes polarized. Weak ionic bond, attractive Coulomb interaction between positively charged Li and negatively charged H and weak van der Waals interaction are responsible for the formation of mixed weak bonding between H₂ molecules and Li+graphene complex. Here the bonding interaction is different from the Dewar-Kubas interaction [255] found in H₂-Ti+C₆₀ or carbon nanotube complexes.[13] As the number of absorbed H₂, n , increases, the positive charge on Li as well as the minimum distance between H₂ and Li slightly increases. No matter what the initial geometry of absorbed H₂ molecules would be, they are relaxed to the same final geometry presented in Fig. 6.2 for any given n . We found no energy barrier for a H₂ molecule approaching the absorbed H₂ when $n \leq 4$. Note that the dissociative absorption of H₂ molecules do not occur in the present system. The energy barrier for the dissociation of H₂ near Li to form Li-H bond is ~ 2 eV.[256] Moreover, dissociation of H₂ to form two C-H bonds at the graphene surface is energetically unfavorable by 0.7 eV.

Maximum number of absorbed H₂ per Li atom is four, and the maximum gravimetric density corresponding to H1+H2 geometry at $\Theta=25$ % coverage is $g_d=12.8$ wt %. This is much higher than the limit ($g_d=6$ wt %) set for the feasible H₂ storage capacity. Note that only for $n = 4$, H1+H2 absorption geometry has slightly lower energy than H1+H3 geometry. This is a remarkable result indicating another application of graphene as a high capacity storage medium. Here Li+graphene complex is superior to Ti+C₆₀ or carbon nanotube complexes since Li is lighter. Even though graphene by itself is stable[19, 257], more stable form is obtained by Li adsorption on graphene due to strong Coulomb repulsion between adsorbed Li atoms. Moreover, Li covered graphene is resistant to clustering of adsorbed Li atoms. Earlier, Durgun *et al.*[15] has predicted that ethylen+Ti complex can store H₂ up to $g_d=14.4$ wt % per molecule. Later, their results have been confirmed experimentally.[258] We believe that hydrogen storage by the Li covered graphene is interesting, since it may not require encapsulating and hence may yield even higher effective g_d .

6.3 Hydrogen storage of calcium atoms adsorbed on graphene

In order to develop an efficient medium of hydrogen storage, carbon based nanostructures functionalized by transition metal atoms have been a subject of active study[256, 259, 238, 15, 7]. Recently, Yoon *et al.*[260] have demonstrated that covering the surface of C_{60} with 32 Ca atoms can store 8.4 wt % hydrogen. Their result, which is crucial for safe and efficient hydrogen storage[254], inspired us to consider graphene as the substrate material for Ca atoms. Graphene is precursor to C_{60} and carbon nanotubes, but being a single atomic plane of graphite its both sides may be suitable for the adsorption of Ca atoms. Graphene by itself has been synthesized showing unusual electronic and magnetic properties[16].

We first consider the adsorption of a single Ca on the graphene as the substrate material. This is modeled by one Ca atom adsorbed on the hollow site (namely H1 site above the center of hexagon) for each (4×4) cell of graphene (namely one Ca atom for every 32 carbon atoms). The Ca-Ca interaction is indeed negligible owing to large distance of $\sim 9.84 \text{ \AA}$ between them. A chemical bonding occurs between Ca and C atoms with a binding energy of 0.99 eV and Ca+graphene distance of 2.10 \AA . Similar to the bonding mechanism of Ca on C_{60} , Ca atom donates part of its charge from 4s-orbital to the π^* -bands of graphene. Due to the formation of an electric field between Ca atom and the graphene layer, part of this charge is then back-donated[260] to the unoccupied 3d-orbitals of Ca through their hybridization with π^* -states. The resulting positive charge of Ca atom is calculated to be ~ 0.96 electrons[54]. The diffusion of the single Ca atom adsorbed on the graphene has to overcome relatively small energy barriers of $Q = 118 \text{ meV}$ and 126 meV to diffuse to the top site (i.e. on top of C atom) and bridge site (on top of the C-C bond), respectively. Ca atom adsorbed on the top or bridge sites becomes less positively charged (~ 0.89 and ~ 0.92 electrons, respectively).

A denser Ca coverage, which is energetically more favorable, is attained, if one Ca is adsorbed on each (2×2) cell of graphene with Ca-Ca distance of 4.92

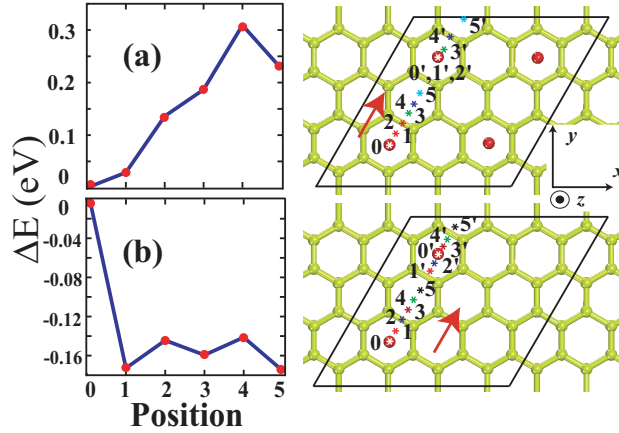


Figure 6.3: (a) Top-right panel: A (4×4) cell of graphene having four Ca atoms. As Ca at the initial position 0 is moved in the direction of the arrow, its z -coordinate is optimized. The remaining three Ca atoms are fully relaxed. Beyond the position 2 of the first Ca, the Coulomb repulsion pushes the second Ca atom in the same direction through positions 3' 4' and 5' to maintain a distance with the first Ca. Top-left: The variation of energy as the first Ca is moves through positions 1-5. (b) Bottom-right panel: Two Ca atoms adsorbed on each (4×4) cell of graphene with their initial positions 0 and 0'. As the first Ca moves from 0 to 1, the second one moves from 0' to 1' having the Ca-Ca distance of 3.74 Å, whereby the energy is lowered by ~ 0.176 meV. Two Ca atoms are prevented from being closer to each other and as the first Ca moves from 1 to 2,3,4 and 5 positions, the second one reverses his direction and moves through 2', 3', 4' and 5' in the same direction as the first Ca atom. Bottom-left: The variation of the energy with the positions of Ca atoms. Taken from Ataca *et al.*[8]

Å. Ca atom adsorbed on the top and bridge sites has a binding energy of 0.86 and 0.89 eV, respectively. However, energetically most favorable adsorption site is found to be the H1 site, which is 2.15 Å above the graphene with a binding energy of 1.14 eV. Here, the Ca-Ca coupling is subtracted from the calculated binding energy. In this dense (2×2) coverage, a stronger electric field is induced between Ca atoms and the graphene layer, which, in turn, leads to a larger back-donation of charge from the graphene layer to 3d-orbitals of Ca atom. Hence by increasing Ca coverage from (4×4) to (2×2), adsorbed Ca atoms become less positively charged, but their binding energy increases. As demonstrated in Fig. 6.3, even if it is energetically more favorable, the clustering of adsorbed Ca atoms is hindered by the Coulomb repulsion.

We next consider the double sided adsorption of Ca. The binding energy of second Ca atom for the double sided adsorption with H1+H2 and H1+H3 configuration indicated in Fig. 6.4 (c), is 1.27 and 1.26 eV, respectively. Since the repulsive Coulomb interaction between Ca atoms on the upper and lower part of the plane is screened by the negative charge around graphene, the binding energy of Ca atom in the double sided adsorption is larger than that in the single sided adsorption. It is also found that $3d$ -orbitals of both Ca atoms have higher occupancies as compared with Ca atom in the single sided adsorption. It is noted, however, that the partial occupancy of $3d$ -orbitals of Ca atom does not cause any magnetic properties in the system. Our results indicate that a stable and uniform Ca coverage up to $\Theta=12.5\%$ ($\Theta=25\%$) can be attained for single sided (double sided with H1+H2 or H1+H3) adsorption forming a (2×2) pattern.

Finite-temperature ab initio molecular dynamics simulations have also been carried out for Ca adsorbed on the (2×2) graphene unit cell for H1 geometry. Simulations are performed by normalizing the velocities of the ions and increasing the temperature of the system gradually from 0 K to 900 K in 300 time steps. The duration of time steps are intentionally taken as 3 fs, which is relatively longer for a MD calculation. If the system is unstable, the geometry of the structure can be destroyed much easier in long time steps. While the bonding between adsorbed Ca atom and the graphene layer is sustained, the adsorbed (2×2) Ca layer begins to diffuse on the graphene layer as the temperature of the system rises over ~ 300 K. However, no structural deformation is observed indicating that the Ca+Graphene system is found to be stable up to 900 K within 300 time steps.

Other alkaline-earth metals, such as beryllium and magnesium do not form strong bonds with graphene. Since Be has ionization potential of 9.32 eV[11] which is much higher than that of Ca atom (6.11 eV), the charge of its $2s$ -orbital cannot easily transferred to the graphene layer. A similar situation occurs also with Mg having an ionization potential of 7.64 eV. Besides, the hybridization of π^* -orbitals of graphene with the d -orbital of Ca atom, which is absent in both

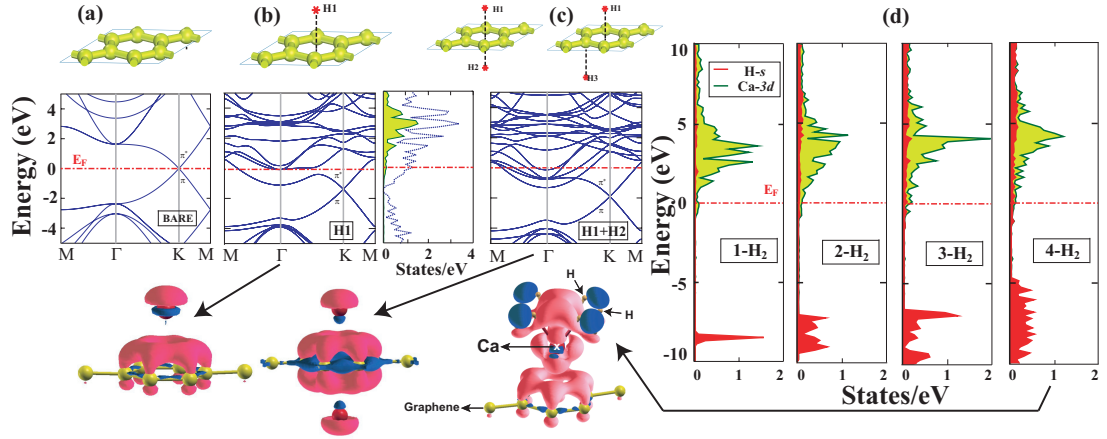


Figure 6.4: (a) The (2×2) cell of graphene lattice and the energy band structure of bare graphene folded to the (2×2) cell. (b) Single Ca atom is adsorbed on the H1 adsorption site of the (2×2) cell of graphene, energy band structure and corresponding total density of states (dotted blue-dark curve) and partial density of states projected to Ca- $3d$ orbitals (green-gray). Isosurfaces of the difference charge density, $\Delta\rho$, with pink (light) and blue (dark) isosurfaces indicating charge accumulation and charge depletion regions. Isosurface charge density is taken to be 0.0038 electrons/ \AA^3 . (c) Similar to (b) (excluding the partial and total density of states), but Ca atoms are adsorbed on both sides of graphene at the H1 and H2 sites. (H1+H3 configuration is also shown.) (d) Partial densities of states on H- s (red-dark) and Ca- $3d$ (green-gray) orbitals for 2, 3, and 4 H₂ absorbed in H1 configuration, and also isosurface of difference charge densities corresponding to $4\text{H}_2 + \text{Ca} + \text{Graphene}$ configuration. Zero of band energy is set to the Fermi energy, E_F . Taken from Ataca *et al.*[8]

Be and Mg plays an essential role in strong binding of Ca to graphene. However, Ti and Co form strong bonds (with binding energies 1.58 and 1.20 eV for the (2×2) adsorption pattern, respectively)[261]. The binding energies of Fe, Cr and Mo are rather weak.

The above arguments related with the binding of Ca to graphene are confirmed by examining the band structure and the charge difference isosurfaces presented in Fig. 6.4. Both H1+H2 and H1+H3 adsorption configurations are included in our calculations because there is a small energy difference (H1+H2 structure is 26 meV more energetic.) between them. Hence, both adsorption

configurations should be observable at room temperature conditions. Charge difference isosurfaces are obtained by subtracting charge densities of Ca and bare graphene from that of Ca+graphene, namely $\Delta\rho = \rho_{Ca+Gr} - \rho_{Ca} - \rho_{Gr}$. It is seen that there is a significant charge accumulation between the adsorbed Ca atom and graphene, which forms the ligand field. Partial occupation of $3d$ -orbitals of Ca can be most clearly demonstrated by the projected density of states in Fig. 6.4 (b). The empty π^* -bands become occupied through charge transfer from $4s$ -orbitals of adsorbed Ca and eventually get distorted due to $3d - \pi^*$ hybridization between $3d$ -orbitals of Ca and the states of π^* -bands as a result of the charge back-donation process. Occupation of distorted graphene π^* -bands gives rise to the metallization of semi-metallic graphene sheets for all adsorption sites. It is also seen that charge density around graphene layer increased significantly as a result of double sided adsorption of Ca. The increase of charge back-donation to $3d$ -orbitals becomes clear by the increased $3d$ -projected density of states below the Fermi level. Changing the adsorption configuration from H1+H2 to H1+H3 does not make any essential changes in the electronic structure. One notes that the position of Fermi energy and hence electron density can be monitored by the controlled doping of Ca atoms. Metallization process is also important for graphene nanoribbons, which form conductive interconnects and spintronic devices in the same nanostructure[261, 135]. It might be an interesting study to investigate the magnetic and electronic properties of Ca adsorption on graphene nanoribbons due to its different bonding mechanism.

We next study the absorption of hydrogen molecules by Ca atoms. A summary of energetics and geometry related with the absorption of molecular H_2 for H1, H1+H2, and H1+H3 sites for the (2×2) and H1 site for the (4×4) coverage are given in Fig. 6.5. The binding mechanism of H_2 invokes not only the adsorbed Ca atom, but also the graphene layer. In the case of single and double H_2 absorption, the absorbed molecules are parallel to graphene and all hydrogen atoms are equidistant from Ca atom. As a result, both hydrogen atom of each absorbed H_2 have the same excess charge of ~ 0.08 electrons. Once the number of H_2 absorbed

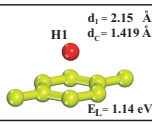
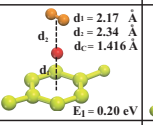
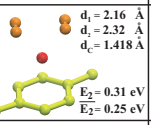
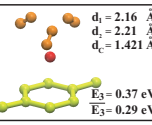
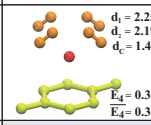
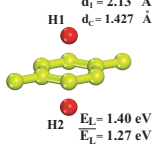
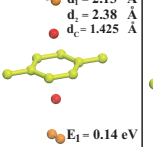
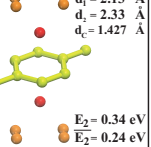
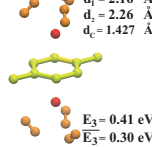
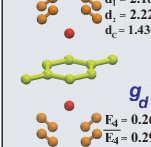
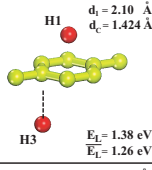
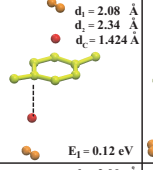
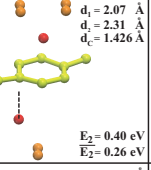
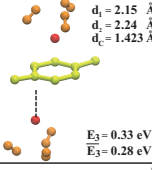
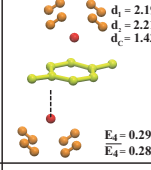
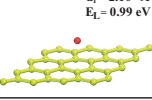
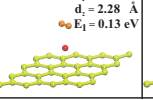
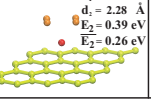
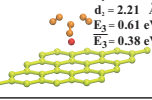
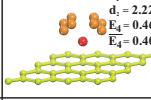
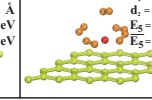
n # of H ₂ per Ca		1	2	3	4	5	
ADSORPTION GEOMETRY (2x2)	H1	 $d_1 = 2.15 \text{ \AA}$ $d_c = 1.419 \text{ \AA}$ $E_L = 1.14 \text{ eV}$	 $d_1 = 2.17 \text{ \AA}$ $d_2 = 2.34 \text{ \AA}$ $d_c = 1.416 \text{ \AA}$ $E_1 = 0.20 \text{ eV}$	 $d_1 = 2.16 \text{ \AA}$ $d_2 = 2.32 \text{ \AA}$ $d_c = 1.418 \text{ \AA}$ $E_2 = 0.31 \text{ eV}$ $\bar{E}_2 = 0.25 \text{ eV}$	 $d_1 = 2.16 \text{ \AA}$ $d_2 = 2.21 \text{ \AA}$ $d_c = 1.421 \text{ \AA}$ $E_3 = 0.37 \text{ eV}$ $\bar{E}_3 = 0.29 \text{ eV}$	 $d_1 = 2.25 \text{ \AA}$ $d_2 = 2.19 \text{ \AA}$ $d_c = 1.422 \text{ \AA}$ $E_4 = 0.35 \text{ eV}$ $\bar{E}_4 = 0.30 \text{ eV}$	—
	H1 + H2	 $d_1 = 2.13 \text{ \AA}$ $d_c = 1.427 \text{ \AA}$ $E_{H1} = 1.40 \text{ eV}$ $\bar{E}_1 = 1.27 \text{ eV}$	 $d_1 = 2.13 \text{ \AA}$ $d_2 = 2.38 \text{ \AA}$ $d_c = 1.425 \text{ \AA}$ $E_1 = 0.14 \text{ eV}$	 $d_1 = 2.13 \text{ \AA}$ $d_2 = 2.33 \text{ \AA}$ $d_c = 1.427 \text{ \AA}$ $E_2 = 0.34 \text{ eV}$ $\bar{E}_2 = 0.24 \text{ eV}$	 $d_1 = 2.16 \text{ \AA}$ $d_2 = 2.26 \text{ \AA}$ $d_c = 1.427 \text{ \AA}$ $E_3 = 0.41 \text{ eV}$ $\bar{E}_3 = 0.30 \text{ eV}$	 $d_1 = 2.18 \text{ \AA}$ $d_2 = 2.22 \text{ \AA}$ $d_c = 1.436 \text{ \AA}$ $E_4 = 0.26 \text{ eV}$ $\bar{E}_4 = 0.29 \text{ eV}$	— $g_d = 8.4 \text{ wt \%}$
	H1 + H3	 $d_1 = 2.10 \text{ \AA}$ $d_c = 1.424 \text{ \AA}$ $E_{H1} = 1.38 \text{ eV}$ $\bar{E}_1 = 1.26 \text{ eV}$	 $d_1 = 2.08 \text{ \AA}$ $d_2 = 2.34 \text{ \AA}$ $d_c = 1.424 \text{ \AA}$ $E_1 = 0.12 \text{ eV}$	 $d_1 = 2.07 \text{ \AA}$ $d_2 = 2.31 \text{ \AA}$ $d_c = 1.426 \text{ \AA}$ $E_2 = 0.40 \text{ eV}$ $\bar{E}_2 = 0.26 \text{ eV}$	 $d_1 = 2.15 \text{ \AA}$ $d_2 = 2.24 \text{ \AA}$ $d_c = 1.423 \text{ \AA}$ $E_3 = 0.33 \text{ eV}$ $\bar{E}_3 = 0.28 \text{ eV}$	 $d_1 = 2.19 \text{ \AA}$ $d_2 = 2.21 \text{ \AA}$ $d_c = 1.430 \text{ \AA}$ $E_4 = 0.29 \text{ eV}$ $\bar{E}_4 = 0.28 \text{ eV}$	—
(4x4)	H1	 $d_1 = 2.10 \text{ \AA}$ $E_L = 0.99 \text{ eV}$	 $d_1 = 2.00 \text{ \AA}$ $d_2 = 2.28 \text{ \AA}$ $E_1 = 0.13 \text{ eV}$	 $d_1 = 2.12 \text{ \AA}$ $d_2 = 2.28 \text{ \AA}$ $E_2 = 0.39 \text{ eV}$ $\bar{E}_2 = 0.26 \text{ eV}$	 $d_1 = 2.23 \text{ \AA}$ $d_2 = 2.21 \text{ \AA}$ $E_3 = 0.61 \text{ eV}$ $\bar{E}_3 = 0.38 \text{ eV}$	 $d_1 = 2.26 \text{ \AA}$ $d_2 = 2.22 \text{ \AA}$ $E_4 = 0.46 \text{ eV}$ $\bar{E}_4 = 0.40 \text{ eV}$	 $d_1 = 2.25 \text{ \AA}$ $d_2 = 2.22 \text{ \AA}$ $E_5 = 0.56 \text{ eV}$ $\bar{E}_5 = 0.43 \text{ eV}$

Figure 6.5: Sites and energetics of Ca adsorbed on graphene with the (2×2) coverage and absorption of H₂ molecules by Ca atoms. d_c is the average C-C distance in the graphene layer. E_L is the binding energy of Ca atom adsorbed on H1-site, which is a minimum energy site. For H1+H2 or H1+H3 configurations corresponding to double sided adsorption, E_L is the binding energy of the second Ca atom and \bar{E}_L is the average binding energy. For H1, H1+H2 and H1+H3 configurations, E_1 is the binding energy of the first H₂ absorbed by each Ca atom; E_n ($n=2-5$) is the binding energy of the last n^{th} H₂ molecule absorbed by each Ca atom; \bar{E}_n is the average binding energy of n H₂ molecules absorbed by a Ca atom. Last row indicates the sites and energetics of one Ca atom adsorbed on each (4×4) cell of graphene and absorption of H₂ molecules by each Ca atom. Only the (4×4) coverage can absorb 5 H₂ molecules. The shaded panel indicates energetically the most favorable H₂ absorption configuration. Taken from Ataca *et al.*[8]

by each Ca atom exceeded two, absorbed H₂ molecules tend to tilt towards Ca atom because of increased positive charge of Ca atom and the symmetry of the bonding configuration of H₂ molecules. The charge of Ca, H atom closer to Ca, H atom farther from Ca and graphene are calculated for 8H₂+2Ca+Graphene system corresponding to H1+H2 configuration in Fig. 6.5 to be $\sim +1.29$, ~ -0.06 , ~ -0.11 and ~ -1.23 electrons. One hydrogen atom of tilted H₂, which is closer to Ca has more excess charge than the other one. It is important to note that charges transferred to absorbed H₂ are not only from Ca atom. Graphene atoms at close proximity also supply charge through back-donation process. At the end, ionic bonding through attractive Coulomb interaction between positively charged Ca and negatively charged H and weak van der Waals interaction are responsible for the formation of mixed bonding between H₂ molecules and Ca adsorbed on graphene. The above discussion is substantiated by the partial density of states in Fig. 6.5(d). The excess charge on H-s and Ca-3d orbitals and their contribution to the states below the Fermi level increase with increasing number of H₂ molecules. Broadening of the molecular level of H₂ at ~ -9 eV indicates significant H₂-H₂ interaction, that in turn increases the binding energy. In fact, the binding energy of the first H₂ molecule to Ca atom which prefers to be parallel to the graphene layer is generally small. Whereas the average binding energy for two H₂ molecules which are again located parallel to the graphene layer, and for three or more H₂ molecules which are tilted around Ca atom are larger. We note that the adsorption of Ca atoms and also H₂ molecules slightly affect the underlying graphene lattice and C-C distance. The average C-C distance of bare graphene is increased from 1.41 Å upon adsorption of Ca and absorption of H₂ to d_c values indicated in all (2×2) structures in Fig. 6.5. Since Ca-Ca interaction is negligible in (4×4) structures, there is no variation in average C-C distance.

Maximum number of absorbed H₂ per adsorbed Ca atom is four for the (2×2) coverage yielding a H₂ storage capacity of 8.4 wt % and five for the (4×4) coverage of graphene. The reason why we include the (4×4) coverage even if the resulting gravimetric density is very low (~ 2.3 wt %), is to mimic the Ca-H₂ interaction in the absence of H₂-H₂ interaction occurring in the (2×2) coverage. Fifth H₂ molecule can be bound to the top of Ca atom in the (4×4) coverage with a

significantly high binding energy. Other 4 H₂ molecules remain in quadrilateral positions around Ca. When we compare graphene with C₆₀[260], we can conclude that C₆₀ with a single Ca adsorbed on the surface yields similar results with the (4×4) coverage on graphene. However, increasing Ca coverage adsorption results in lower binding energies of adsorbed H₂ molecules in the present case. Unfortunately, we cannot comment on the case of high Ca coverage of C₆₀, since Yoon *et al.*[260] did not give details on the energetics of H₂ molecules in denser Ca adsorption. They have just emphasized that adsorption of 32 Ca results in full coverage of C₆₀ surface and this structure can absorb up to 92 H₂ molecules with binding energy of ~ 0.4 eV. Under these circumstances, single Ca atom can hold only 3 H₂ molecules. In graphene structures, while the charge on (ie. charge depletion or positive charge) Ca increases with increased number of the adsorbed H₂ molecules, the electric field around Ca increases. This, in turn, results in a decrement in the distance between adsorbed Ca and polarized H₂ molecules. The charge on graphene decreases, as well.

Chapter 7

Conclusions

My thesis work is dedicated to the design of nanomaterials for hydrogen economy using first-principles calculations. Some of these materials are found to be suitable for obtaining H₂ by splitting the water molecule, others convenient for high capacity hydrogen storage. We predicted MoS₂ triple vacancies in the single layer MoS₂ honeycomb structure can split H₂O. Graphene functionalized by Li and Ca atoms can store hydrogen molecule with a storage capacity larger than the limit set by US Department of Energy.

Recently synthesized single layer 1H-MoS₂[21] is now considered as the material of future[30] and the contender of graphene. We first studied the electronic, magnetic, mechanical and vibrational properties of single layer MoS₂ taking into account the dimensionality effects. Having predicted several properties and revealed their relations with the structural parameters of 1H-MoS₂, we addressed the question whether single layers of other transition metal dichalcogenides can exist in free standing form. We carried out extensive stability analysis of several MX₂ compounds and found out a large number of them can be stable in 1H-MX₂ structure.

In case of vacancy defects of 1H-MoS₂, we focused on their interaction with H₂O molecule. S, S₂-divacancy repel water molecule due to negatively charged regions on S-layers. We demonstrated that a free H₂O is attracted by a MoS₂

vacancy and is trapped in the hole. Concomitantly, H_2O is split into constituent atoms. H atoms of H_2O are preferably attached to two folded S-atoms surrounding the vacancy, while O remains to be bonded to the dangling bonds of Mo atoms around vacancy. This process by itself is exothermic and spontaneous. Two crucial ingredients underlying this catalytic reaction are: (i) The electronegativity of Mo is slightly smaller than that of H. (ii) The ionization energy of Mo is almost half of H. Another H_2O can also be trapped in the vacancy region. However splitting of H_2O to OH and H is observed due to less charge transfer from five-fold Mo atoms to O of H_2O . Desorption of adsorbed H atoms from 1H-MoS₂ may follow different reaction paths: (i) Hydrogen atoms can desorb by the breaking of the S-H bonds from two folded S atoms surrounding the vacancy and eventually form H_2 . In this photochemical process one needs photon energies $h\nu=2.90\text{-}3.08$ eV, which lie at the maximum intensity range of visible light spectrum. (ii) While the S-H bonds surrounding the vacancy are broken, H atoms can be adsorbed on 1H-MoS₂ with relatively weaker binding energies. Subsequently, owing to a small energy barrier these H atoms diffuse readily and form H_2 molecule spontaneously when they are within a threshold distance. Through concerted processes this reaction path may require lower photon energy in the range of $h\nu=2.12\text{-}2.30$ eV.

While advances in nanotechnology can provides us 1H-MoS₂ with high vacancy concentration, the removal of O bound to Mo through charging or other means can allow us to recyclable use of the same system. Because of exceptional properties similar to one revealed, single layer MoS₂ honeycomb structure has been considered as the contender of graphene. We believe that the catalytic reaction predicted in this thesis heralds a sustainable and clean energy resource and will initiate several experimental studies. As revealed in this thesis, several transition metal dichalcogenides form similar stable single layer honeycomb structures and are potential candidates for similar catalytic reactions. Not only for H_2O splitting, each stable structure requires detailed investigation both experimentally and theoretically. Hopefully this thesis will be a seminal study in the research on single layer transition metal dichalcogenides.

The advantage of graphene over transition metal dichalcogenides emerges in the case of high capacity hydrogen storage. The mass of graphene per unit area

is much smaller than those of transition metal dichalcogenides. For this fact, graphene can be used as a high capacity hydrogen storage medium upon adsorption of adatoms which can physisorb H_2 molecules. For sustainable energy of the future, not only production but also storage of H_2 will take place in nanostructures. In this thesis we showed that upon Li and Ca adatom adsorption, graphene surface can be functionalized to physisorb H_2 molecules with 12.8 and 8.4 % weight percentage. These results are much higher than what Department of Energy (DOE) in US targeted for hydrogen capacity research (6 % wt.). Synthesis of free standing graphene and MoS_2 were achieved recently.

Finally, we hope that our predictions in this thesis regarding to two dimensional nanostructures and their functionalization will be realized by experimentalist in the near future and will contribute to the efforts discovering sustainable and clean energy resources

Bibliography

- [1] C. Ataca, M. Topsakal, E. Akturk, and S. Ciraci. A Comparative Study of Lattice Dynamics of Three- and Two-Dimensional MoS(2). *JOURNAL OF PHYSICAL CHEMISTRY C*, 115(33):16354–16361, AUG 25 2011.
- [2] N. Wakabayashi, H. G. Smith, and R. M. Nicklow. Lattice dynamics of hexagonal mos₂ studied by neutron scattering. *PHYSICAL REVIEW B*, 12(2):659–663, Jul 1975.
- [3] H. S. S. Ramakrishna Matte, A. Gomathi, Arun K. Manna, Dattatray J. Late, Ranjan Datta, Swapan K. Pati, and C. N. R. Rao. MoS₂ and WS₂ Analogues of Graphene. *ANGEWANDTE CHEMIE-INTERNATIONAL EDITION*, 49(24):4059–4062, 2010.
- [4] JM Soler, E Artacho, JD Gale, A Garcia, J Junquera, P Ordejon, and D Sanchez-Portal. The SIESTA method for ab initio order-N materials simulation. *JOURNAL OF PHYSICS-CONDENSED MATTER*, 14(11):2745–2779, MAR 25 2002.
- [5] C. Ataca, H. Sahin, E. Akturk, and S. Ciraci. Mechanical and Electronic Properties of MoS(2) Nanoribbons and Their Defects. *JOURNAL OF PHYSICAL CHEMISTRY C*, 115(10):3934–3941, MAR 17 2011.
- [6] C. Ataca and S. Ciraci. Functionalization of Single-Layer MoS(2) Honeycomb Structures. *JOURNAL OF PHYSICAL CHEMISTRY C*, 115(27):13303–13311, JUL 14 2011.

- [7] C. Ataca, E. Akturk, S. Ciraci, and H. Ustunel. High-capacity hydrogen storage by metallized graphene. *APPLIED PHYSICS LETTERS*, 93(4):043123, JUL 28 2008.
- [8] C. Ataca, E. Akturk, and S. Ciraci. Hydrogen storage of calcium atoms adsorbed on graphene: First-principles plane wave calculations. *PHYSICAL REVIEW B*, 79(4):041406, JAN 2009.
- [9] P JOENSEN, ED CROZIER, N ALBERDING, and RF FRINDT. A STUDY OF SINGLE-LAYER AND RESTACKED MOS2 BY X-RAY-DIFFRACTION AND X-RAY ABSORPTION-SPECTROSCOPY. *JOURNAL OF PHYSICS C-SOLID STATE PHYSICS*, 20(26):4043–4053, SEP 20 1987.
- [10] D YANG, SJ SANDOVAL, WMR DIVIGALPITIYA, JC IRWIN, and RF FRINDT. STRUCTURE OF SINGLE-MOLECULAR-LAYER MOS2. *PHYSICAL REVIEW B*, 43(14):12053–12056, MAY 15 1991.
- [11] Charles Kittel. Introduction to solid state physics, 1995.
- [12] S. Dag, Y. Ozturk, S. Ciraci, and T. Yildirim. Adsorption and dissociation of hydrogen molecules on bare and functionalized carbon nanotubes. *Physical Review B*, 72:155404, Oct 2005.
- [13] T. Yildirim and S. Ciraci. Titanium-decorated carbon nanotubes as a potential high-capacity hydrogen storage medium. *Physical Review Letters*, 94:175501, May 2005.
- [14] Yufeng Zhao, Yong-Hyun Kim, A. C. Dillon, M. J. Heben, and S. B. Zhang. Hydrogen storage in novel organometallic buckyballs. *Phys. Rev. Lett.*, 94:155504, Apr 2005.
- [15] E. Durgun, S. Ciraci, W. Zhou, and T. Yildirim. Transition-metal-ethylene complexes as high-capacity hydrogen-storage media. *Physical Review Letters*, 97:226102, Nov 2006.

- [16] KS Novoselov, AK Geim, SV Morozov, D Jiang, Y Zhang, SV Dubonos, IV Grigorieva, and AA Firsov. Electric field effect in atomically thin carbon films. *SCIENCE*, 306(5696):666–669, OCT 22 2004.
- [17] Adam Heller. Hydrogen-evolving solar cells. *Science*, 223(4641):1141–1148, 1984.
- [18] Akihiko and Kudo. Recent progress in the development of visible light-driven powdered photocatalysts for water splitting. *International Journal of Hydrogen Energy*, 32(14):2673 – 2678, 2007. <ce:title>International Conference on Materials for Hydrogen Energy: Solar Hydrogen (ICMHE 2004)</ce:title>.
- [19] A. K. Geim and K. S. Novoselov. The rise of graphene. *NATURE MATERIALS*, 6(3):183–191, MAR 2007.
- [20] Chuanhong Jin, Fang Lin, Kazu Suenaga, and Sumio Iijima. Fabrication of a Freestanding Boron Nitride Single Layer and Its Defect Assignments. *PHYSICAL REVIEW LETTERS*, 102(19):195505, MAY 15 2009.
- [21] Kin Fai Mak, Changgu Lee, James Hone, Jie Shan, and Tony F. Heinz. Atomically Thin MoS(2): A New Direct-Gap Semiconductor. *PHYSICAL REVIEW LETTERS*, 105(13):136805, SEP 24 2010.
- [22] Zhiyong Wang, Keke Zhao, Hong Li, Zheng Liu, Zujin Shi, Jing Lu, Kazu Suenaga, Soon-Kil Joung, Toshiya Okazaki, Zhaoxia Jin, Zhennan Gu, Zhengxiang Gao, and Sumio Iijima. Ultra-narrow WS(2) nanoribbons encapsulated in carbon nanotubes. *JOURNAL OF MATERIALS CHEMISTRY*, 21(1):171–180, 2011.
- [23] Yafei Li, Zhen Zhou, Shengbai Zhang, and Zhongfang Chen. MoS(2) Nanoribbons: High Stability and Unusual Electronic and Magnetic Properties. *JOURNAL OF THE AMERICAN CHEMICAL SOCIETY*, 130(49):16739–16744, DEC 10 2008.
- [24] Andrea Splendiani, Liang Sun, Yuanbo Zhang, Tianshu Li, Jonghwan Kim, Chi-Yung Chim, Giulia Galli, and Feng Wang. Emerging Photoluminescence in Monolayer MoS₂. *NANO LETTERS*, 10(4):1271–1275, APR 2010.

- [25] Changgu Lee, Huguen Yan, Louis E. Brus, Tony F. Heinz, James Hone, and Sunmin Ryu. Anomalous Lattice Vibrations of Single- and Few-Layer MoS(2). *ACS NANO*, 4(5):2695–2700, MAY 2010.
- [26] Changgu Lee, Qunyang Li, William Kalb, Xin-Zhou Liu, Helmuth Berger, Robert W. Carpick, and James Hone. Frictional Characteristics of Atomically Thin Sheets. *SCIENCE*, 328(5974):76–80, APR 2 2010.
- [27] B Hinnemann, PG Moses, J Bonde, KP Jorgensen, JH Nielsen, S Horch, I Chorkendorff, and JK Norskov. Biornimetic hydrogen evolution: MoS2 nanoparticles as catalyst for hydrogen evolution. *JOURNAL OF THE AMERICAN CHEMICAL SOCIETY*, 127(15):5308–5309, APR 20 2005.
- [28] Poul Georg Moses, Berit Hinnemann, Henrik Topsøe, and Jens K. Norskov. The hydrogenation and direct desulfurization reaction pathway in thiophene hydrodesulfurization over MoS(2) catalysts at realistic conditions: A density functional study. *JOURNAL OF CATALYSIS*, 248(2):188–203, JUN 10 2007.
- [29] G KLINE, KK KAM, R ZIEGLER, and BA PARKINSON. FURTHER-STUDIES OF THE PHOTO-ELECTROCHEMICAL PROPERTIES OF THE GROUP-VI TRANSITION-METAL DICHALCOGENIDES. *SOLAR ENERGY MATERIALS*, 6(3):337–350, 1982.
- [30] B. Radisavljevic, A. Radenovic, J. Brivio, V. Giacometti, and A. Kis. Single-layer MoS2 transistors. *NATURE NANOTECHNOLOGY*, 6(3):147–150, MAR 2011.
- [31] M. C. Payne, M. P. Teter, D. C. Allan, T. A. Arias, and J. D. Joannopoulos. Iterative minimization techniques for *ab initio* total-energy calculations: molecular dynamics and conjugate gradients. *Rev. Mod. Phys.*, 64:1045–1097, Oct 1992.
- [32] John P. Perdew, Robert G. Parr, Mel Levy, and Jose L. Balduz. Density-functional theory for fractional particle number: Derivative discontinuities of the energy. *Phys. Rev. Lett.*, 49:1691–1694, Dec 1982.

- [33] L. W. Bruch, R. D. Diehl, and J. A. Venables. Progress in the measurement and modeling of physisorbed layers. *Rev. Mod. Phys.*, 79:1381–1454, Nov 2007.
- [34] Paul C. Rusu, Gianluca Giovannetti, Christ Weijtens, Reinder Coehoorn, and Geert Brocks. First-principles study of the dipole layer formation at metal-organic interfaces. *Phys. Rev. B*, 81:125403, Mar 2010.
- [35] S. A. Shevlin and Z. X. Guo. High-capacity room-temperature hydrogen storage in carbon nanotubes via defect-modulated titanium doping. *The Journal of Physical Chemistry C*, 112(44):17456–17464, 2008.
- [36] Yi Gao and X C Zeng. Ab initio study of hydrogen adsorption on benzenoid linkers in metal organic framework materials. *Journal of Physics: Condensed Matter*, 19(38):386220, 2007.
- [37] A. L. Aguiar, S. B. Fagan, L. B. da Silva, J. Mendes Filho, and A. G. Souza Filho. Benzonitrile adsorption on fe-doped carbon nanostructures. *The Journal of Physical Chemistry C*, 114(24):10790–10795, 2010.
- [38] Xiaoqing Tian, Jianbin Xu, and Xiaomu Wang. Band gap opening of bilayer graphene by f4-tcnq molecular doping and externally applied electric field. *The Journal of Physical Chemistry B*, 114(35):11377–11381, 2010.
- [39] X. Q. Tian, J. B. Xu, and X. M. Wang. Self-assembly of ptcda ultrathin films on graphene: Structural phase transition and charge transfer saturation. *The Journal of Physical Chemistry C*, 114(49):20917–20924, 2010.
- [40] L. A. Girifalco and Miroslav Hodak. Van der waals binding energies in graphitic structures. *Phys. Rev. B*, 65:125404, Feb 2002.
- [41] J. S. Arellano, L. M. Molina, A. Rubio, and J. A. Alonso. Density functional study of adsorption of molecular hydrogen on graphene layers. *The Journal of Chemical Physics*, 112(18):8114–8119, 2000.
- [42] ZhiGang Wang, MingGuang Yao, ShouFu Pan, MingXing Jin, BingBing Liu, and HongXing Zhang. A barrierless process from physisorption to

- chemisorption of h₂ molecules on light-element-doped fullerenes. *The Journal of Physical Chemistry C*, 111(11):4473–4476, 2007.
- [43] Oleksandr Voznyy and Jan J. Dubowski. Adsorption kinetics of hydrogen sulfide and thiols on gaas (001) surfaces in a vacuum. *The Journal of Physical Chemistry C*, 112(10):3726–3733, 2008.
- [44] Stefan Grimme. Semiempirical GGA-type density functional constructed with a long-range dispersion correction. *JOURNAL OF COMPUTATIONAL CHEMISTRY*, 27(15):1787–1799, NOV 30 2006.
- [45] S. Hufner. Electronic structure of nio and related 3d transition metal compounds. *Advances in Physics*, 43(2):183–356, 1994.
- [46] Hendrik J. Monkhorst and James D. Pack. Special points for brillouin-zone integrations. *PHYSICAL REVIEW B*, 13(12):5188–5192, Jun 1976.
- [47] D VANDERBILT. SOFT SELF-CONSISTENT PSEUDOPOTENTIALS IN A GENERALIZED EIGENVALUE FORMALISM. *PHYSICAL REVIEW B*, 41(11):7892–7895, APR 15 1990.
- [48] PE BLOCHL. PROJECTOR AUGMENTED-WAVE METHOD. *PHYSICAL REVIEW B*, 50(24):17953–17979, DEC 15 1994.
- [49] G KRESSE and J HAFNER. ABINITIO MOLECULAR-DYNAMICS FOR LIQUID-METALS. *PHYSICAL REVIEW B*, 47(1):558–561, JAN 1 1993.
- [50] G Kresse and J Furthmuller. Efficient iterative schemes for ab initio total-energy calculations using a plane-wave basis set. *PHYSICAL REVIEW B*, 54(16):11169–11186, OCT 15 1996.
- [51] QUANTUM-ESPRESSO is a community project for high-quality quantum-simulation software, based on density-functional theory, and coordinated by Paolo Giannozzi. See <http://www.quantum-espresso.org> and <http://www.pwscf.org>.
- [52] SL Dudarev, GA Botton, SY Savrasov, CJ Humphreys, and AP Sutton. Electron-energy-loss spectra and the structural stability of nickel oxide: An LSDA+U study. *PHYSICAL REVIEW B*, 57(3):1505–1509, JAN 15 1998.

- [53] Hendrik J. Monkhorst and James D. Pack. Special points for brillouin-zone integrations. *Phys. Rev. B*, 13:5188–5192, Jun 1976.
- [54] G Henkelman, A Arnaldsson, and H Jonsson. A fast and robust algorithm for Bader decomposition of charge density. *COMPUTATIONAL MATERIALS SCIENCE*, 36(3):354–360, JUN 2006.
- [55] M. Shishkin and G. Kresse. Implementation and performance of the frequency-dependent GW method within the PAW framework. *PHYSICAL REVIEW B*, 74(3):035101, JUL 2006.
- [56] S. Cahangirov, M. Topsakal, E. Akturk, H. Sahin, and S. Ciraci. Two- and One-Dimensional Honeycomb Structures of Silicon and Germanium. *PHYSICAL REVIEW LETTERS*, 102(23):236804, JUN 12 2009.
- [57] Dario Alfe. PHON: A program to calculate phonons using the small displacement method. *COMPUTER PHYSICS COMMUNICATIONS*, 180(12):2622–2633, DEC 2009.
- [58] R. S. Title and M. W. Shafer. Electron-paramagnetic-resonance studies on arsenic acceptors in natural ($2h$) and synthetic ($3r$) mos_2 crystals. *Phys. Rev. B*, 8(2):615–620, Jul 1973.
- [59] T. J. Wieting and J. L. Verble. Infrared and raman studies of long-wavelength optical phonons in hexagonal mos_2 . *PHYSICAL REVIEW B*, 3(12):4286–4292, Jun 1971.
- [60] J. L. Verble and T. J. Wieting. Lattice mode degeneracy in mos_2 and other layer compounds. *Phys. Rev. Lett.*, 25(6):362–365, Aug 1970.
- [61] R. V. Kasowski. Band structure of mos_2 and nbs_2 . *PHYSICAL REVIEW LETTERS*, 30(23):1175–1178, Jun 1973.
- [62] L. F. Mattheiss. Energy bands for $2h - nbse_2$ and $2h - mos_2$. *PHYSICAL REVIEW LETTERS*, 30(17):784–787, Apr 1973.
- [63] R COEHOORN, C HAAS, J DIJKSTRA, CJF FLIPSE, RA DEGROOT, and A WOLD. ELECTRONIC-STRUCTURE OF MOSE2,

- MOS₂, AND WSE₂. 1. BAND-STRUCTURE CALCULATIONS AND PHOTOELECTRON-SPECTROSCOPY. *PHYSICAL REVIEW B*, 35(12):6195–6202, APR 15 1987.
- [64] K KOBAYASHI and J YAMAUCHI. ELECTRONIC-STRUCTURE AND SCANNING-TUNNELING-MICROSCOPY IMAGE OF MOLYBDENUM DICHALCOGENIDE SURFACES. *PHYSICAL REVIEW B*, 51(23):17085–17095, JUN 15 1995.
- [65] GL Frey, R Tenne, MJ Matthews, MS Dresselhaus, and G Dresselhaus. Raman and resonance Raman investigation of MoS₂ nanoparticles. *PHYSICAL REVIEW B*, 60(4):2883–2892, JUL 15 1999.
- [66] T Boker, R Severin, A Muller, C Janowitz, R Manzke, D Voss, P Kruger, A Mazur, and J Pollmann. Band structure of MoS₂, MoSe₂, and alpha-MoTe₂: Angle-resolved photoelectron spectroscopy and ab initio calculations. *PHYSICAL REVIEW B*, 64(23):235305, DEC 15 2001.
- [67] H Rydberg, M Dion, N Jacobson, E Schroder, P Hyldgaard, SI Simak, DC Langreth, and BI Lundqvist. Van der Waals density functional for layered structures. *PHYSICAL REVIEW LETTERS*, 91(12):126402, SEP 19 2003.
- [68] JD Fuhr, A Saul, and JO Sofo. Scanning tunneling microscopy chemical signature of point defects on the MoS₂(0001) surface. *PHYSICAL REVIEW LETTERS*, 92(2):026802, JAN 16 2004.
- [69] Viktoria V. Ivanovskaya, Alberto Zobelli, Alexandre Gloter, Nathalie Brun, Virginie Serin, and Christian Colliex. Ab initio study of bilateral doping within the MoS₂-NbS₂ system. *PHYSICAL REVIEW B*, 78(13):134104, OCT 2008.
- [70] Min Huang and Kyeongjae Cho. Density Functional Theory Study of CO Hydrogenation on a MoS₂ Surface. *JOURNAL OF PHYSICAL CHEMISTRY C*, 113(13):5238–5243, APR 2 2009.

- [71] Poul Georg Moses, Jens J. Mortensen, Bengt I. Lundqvist, and Jens K. Nørskov. Density functional study of the adsorption and van der Waals binding of aromatic and conjugated compounds on the basal plane of MoS₂. *JOURNAL OF CHEMICAL PHYSICS*, 130(10):104709, MAR 14 2009.
- [72] A. R. Botello-Mendez, F. Lopez-Urias, M. Terrones, and H. Terrones. Metallic and ferromagnetic edges in molybdenum disulfide nanoribbons. *NANOTECHNOLOGY*, 20(32):325703, AUG 12 2009.
- [73] Q. C. Sun, X. S. Xu, L. I. Vergara, R. Rosentsveig, and J. L. Musfeldt. Dynamical charge and structural strain in inorganic fullerene-like MoS₂ nanoparticles. *PHYSICAL REVIEW B*, 79(20):205405, MAY 2009.
- [74] Jonathan N. Coleman, Mustafa Lotya, Arlene O'Neill, Shane D. Bergin, Paul J. King, Umar Khan, Karen Young, Alexandre Gaucher, Sukanta De, Ronan J. Smith, Igor V. Shvets, Sunil K. Arora, George Stanton, Hye-Young Kim, Kangho Lee, Gyu Tae Kim, Georg S. Duesberg, Toby Hallam, John J. Boland, Jing Jing Wang, John F. Donegan, Jaime C. Grunlan, Gregory Moriarty, Aleksey Shmeliov, Rebecca J. Nicholls, James M. Perkins, Eleanor M. Grievson, Koenraad Theuvsissen, David W. McComb, Peter D. Nellist, and Valeria Nicolosi. Two-dimensional nanosheets produced by liquid exfoliation of layered materials. *Science*, 331(6017):568–571, 2011.
- [75] P JOENSEN, RF FRINDT, and SR MORRISON. SINGLE-LAYER MOS₂. *MATERIALS RESEARCH BULLETIN*, 21(4):457–461, APR 1986.
- [76] KS Novoselov, D Jiang, F Schedin, TJ Booth, VV Khotkevich, SV Morozov, and AK Geim. Two-dimensional atomic crystals. *PROCEEDINGS OF THE NATIONAL ACADEMY OF SCIENCES OF THE UNITED STATES OF AMERICA*, 102(30):10451–10453, JUL 26 2005.
- [77] Kin Fai Mak, Changgu Lee, James Hone, Jie Shan, and Tony F. Heinz. Atomically Thin MoS₂: A New Direct-Gap Semiconductor. *PHYSICAL REVIEW LETTERS*, 105(13):136805, SEP 24 2010.

- [78] Changgu Lee, Hugen Yan, Louis E. Brus, Tony F. Heinz, James Hone, and Sunmin Ryu. Anomalous Lattice Vibrations of Single- and Few-Layer MoS₂. *ACS NANO*, 4(5):2695–2700, MAY 2010.
- [79] S Helveg, JV Lauritsen, E Laegsgaard, I Stensgaard, JK Norskov, BS Clausen, H Topsøe, and F Besenbacher. Atomic-scale structure of single-layer MoS₂ nanoclusters. *PHYSICAL REVIEW LETTERS*, 84(5):951–954, JAN 31 2000.
- [80] PA BERTRAND. SURFACE-PHONON DISPERSION OF MOS₂. *PHYSICAL REVIEW B*, 44(11):5745–5749, SEP 15 1991.
- [81] SJ SANDOVAL, D YANG, RF FRINDT, and JC IRWIN. RAMAN-STUDY AND LATTICE-DYNAMICS OF SINGLE MOLECULAR LAYERS OF MOS₂. *PHYSICAL REVIEW B*, 44(8):3955–3962, AUG 15 1991.
- [82] G Seifert, H Terrones, M Terrones, G Jungnickel, and T Frauenheim. Structure and electronic properties of MoS₂ nanotubes. *PHYSICAL REVIEW LETTERS*, 85(1):146–149, JUL 3 2000.
- [83] Yafei Li, Zhen Zhou, Shengbai Zhang, and Zhongfang Chen. MoS₂ Nanoribbons: High Stability and Unusual Electronic and Magnetic Properties. *JOURNAL OF THE AMERICAN CHEMICAL SOCIETY*, 130(49):16739–16744, DEC 10 2008.
- [84] S. Lebegue and O. Eriksson. Electronic structure of two-dimensional crystals from ab initio theory. *PHYSICAL REVIEW B*, 79(11):115409, MAR 2009.
- [85] MV Bollinger, JV Lauritsen, KW Jacobsen, JK Norskov, S Helveg, and F Besenbacher. One-dimensional metallic edge states in MoS₂. *PHYSICAL REVIEW LETTERS*, 87(19):196803, NOV 5 2001.
- [86] L Rapoport, Y Bilik, Y Feldman, M Homyonfer, SR Cohen, and R Tenne. Hollow nanoparticles of WS₂ as potential solid-state lubricants. *NATURE*, 387(6635):791–793, JUN 19 1997.

- [87] Thomas F. Jaramillo, Kristina P. Jorgensen, Jacob Bonde, Jane H. Nielsen, Sebastian Horch, and Ib Chorkendorff. Identification of active edge sites for electrochemical H₂ evolution from MoS₂ nanocatalysts. *SCIENCE*, 317(5834):100–102, JUL 6 2007.
- [88] MY Sun, AE Nelson, and J Adjaye. On the incorporation of nickel and cobalt into MoS₂-edge structures. *JOURNAL OF CATALYSIS*, 226(1):32–40, AUG 15 2004.
- [89] P Raybaud, J Hafner, G Kresse, S Kasztelan, and H Toulhoat. Ab initio study of the H₂-H₂S/MoS₂ gas-solid interface: The nature of the catalytically active sites. *JOURNAL OF CATALYSIS*, 189(1):129–146, JAN 1 2000.
- [90] Poul Georg Moses, Berit Hinnemann, Henrik Topsoe, and Jens K. Nørskov. The hydrogenation and direct desulfurization reaction pathway in thiophene hydrodesulfurization over MoS₂ catalysts at realistic conditions: A density functional study. *JOURNAL OF CATALYSIS*, 248(2):188–203, JUN 10 2007.
- [91] Jeppe V. Lauritsen, Jakob Kibsgaard, Georg H. Olesen, Poul G. Moses, Berit Hinnemann, Stig Helveg, Jens K. Nørskov, Bjerne S. Clausen, Henrik Topsoe, Erik Laegsgaard, and Flemming Besenbacher. Location and coordination of promoter atoms in Co- and Ni-promoted MoS₂-based hydrotreating catalysts. *JOURNAL OF CATALYSIS*, 249(2):220–233, JUL 25 2007.
- [92] JV Lauritsen, MV Bollinger, E Laegsgaard, KW Jacobsen, JK Nørskov, BS Clausen, H Topsoe, and F Besenbacher. Atomic-scale insight into structure and morphology changes of MoS₂ nanoclusters in hydrotreating catalysts. *JOURNAL OF CATALYSIS*, 221(2):510–522, JAN 25 2004.
- [93] JV Lauritsen, S Helveg, E Laegsgaard, I Stensgaard, BS Clausen, H Topsoe, and E Besenbacher. Atomic-scale structure of Co-Mo-S nanoclusters in hydrotreating catalysts. *JOURNAL OF CATALYSIS*, 197(1):1–5, JAN 1 2001.

- [94] Teodora Todorova, Roel Prins, and Thomas Weber. A density functional theory study of the hydrogenolysis and elimination reactions of C₂H₅SH on the catalytically active (100) edge of 2H-MoS₂. *JOURNAL OF CATALYSIS*, 246(1):109–117, FEB 15 2007.
- [95] JP Wilcoxon, TR Thurston, and JE Martin. Applications of metal and semiconductor nanoclusters as thermal and photo-catalysts. *NANOSTRUCTURED MATERIALS*, 12(5-8, Part B Sp. Iss. SI):993–997, JUL 1999. 4th International Conference on Nanostructured Materials (NANO 98), STOCKHOLM, SWEDEN, JUN 14-19, 1998.
- [96] Jeppe V. Lauritsen, Jakob Kibsgaard, Stig Helveg, Henrik Topsøe, Bjerne S. Clausen, Erik Laegsgaard, and Flemming Besenbacher. Size-dependent structure of MoS₂ nanocrystals. *NATURE NANOTECHNOLOGY*, 2(1):53–58, JAN 2007.
- [97] P Raybaud, J Hafner, G Kresse, and H Toulhoat. Adsorption of thiophene on the catalytically active surface of MoS₂: An ab initio local-density-functional study. *PHYSICAL REVIEW LETTERS*, 80(7):1481–1484, FEB 16 1998.
- [98] Jiangang He, Kechen Wu, Rongjian Sa, Qiaohong Li, and Yongqin Wei. Magnetic properties of nonmetal atoms absorbed MoS₂ monolayers. *APPLIED PHYSICS LETTERS*, 96(8):082504, FEB 22 2010.
- [99] Stefan Grimme. Semiempirical GGA-type density functional constructed with a long-range dispersion correction. *JOURNAL OF COMPUTATIONAL CHEMISTRY*, 27(15):1787–1799, NOV 30 2006.
- [100] M. Dion, H. Rydberg, E. Schröder, D. C. Langreth, and B. I. Lundqvist. Van der waals density functional for general geometries. *Phys. Rev. Lett.*, 92(24):246401, Jun 2004.
- [101] JS Arellano, LM Molina, A Rubio, and JA Alonso. Density functional study of adsorption of molecular hydrogen on graphene layers. *JOURNAL OF CHEMICAL PHYSICS*, 112(18):8114–8119, MAY 8 2000.

- [102] LA Girifalco and M Hodak. Van der Waals binding energies in graphitic structures. *PHYSICAL REVIEW B*, 65(12):125404, MAR 15 2002.
- [103] Y. Baskin and L. Meyer. Lattice constants of graphite at low temperatures. *Phys. Rev.*, 100(2):544, Oct 1955.
- [104] Peter Trucano and Ruey Chen. *Nature (London)*, 258:136, 1975.
- [105] You Xiang Zhao and Ian L. Spain. X-ray diffraction data for graphite to 20 gpa. *Phys. Rev. B*, 40(2):993–997, Jul 1989.
- [106] Alexey Bosak, Michael Krisch, Marcel Mohr, Janina Maultzsch, and Christian Thomsen. Elasticity of single-crystalline graphite: Inelastic x-ray scattering study. *Phys. Rev. B*, 75(15):153408, Apr 2007.
- [107] M. Hanfland, H. Beister, and K. Syassen. Graphite under pressure: Equation of state and first-order raman modes. *Phys. Rev. B*, 39(17):12598–12603, Jun 1989.
- [108] KK KAM and BA PARKINSON. DETAILED PHOTOCURRENT SPECTROSCOPY OF THE SEMICONDUCTING GROUP-VI TRANSITION-METAL DICHALCOGENIDES. *JOURNAL OF PHYSICAL CHEMISTRY*, 86(4):463–467, 1982.
- [109] KT Park, M RichardsBabb, MS Freund, J Weiss, and K Klier. Surface structure of single-crystal MoS₂(0002) and Cs/MoS₂(0002) by X-ray photoelectron diffraction. *JOURNAL OF PHYSICAL CHEMISTRY*, 100(25):10739–10745, JUN 20 1996.
- [110] Kay Weiss and James M. Phillips. Calculated specific surface energy of molybdenite (*mos*₂). *Phys. Rev. B*, 14(12):5392–5395, Dec 1976.
- [111] Tsachi Livneh and Eran Sterer. Resonant raman scattering at exciton states tuned by pressure and temperature in $2h - mos_2$. *Phys. Rev. B*, 81(19):195209, May 2010.
- [112] J. M. Chen and C. S. Wang. Second order raman spectrum of mos₂. *Solid State Communications*, 14(9):857 – 860, 1974.

- [113] It is known that Born effective charge is a tensor. The reported experimental as well as calculated values are given for each atom in xy-plane. The calculated values for z-direction are $Z_B^*[\text{Mo}] = 0.58$ and $Z_B^*[\text{S}] = -0.31$ electrons for 2H-MoS₂ and very small values for 1H-MoS₂.
- [114] Owing to the precision of the calculation, the fourth acoustic mode (twisting mode) in Fig.1 appears slightly above $\Omega(k=0) = 0 \text{ cm}^{-1}$.
- [115] E Dobardzic, B Dakic, M Damnjanovic, and I Milosevic. Zero m phonons in MoS₂ nanotubes. *PHYSICAL REVIEW B*, 71(12):121405, MAR 2005.
- [116] Roland Gillen, Marcel Mohr, Christian Thomsen, and Janina Maultzsch. Vibrational properties of graphene nanoribbons by first-principles calculations. *PHYSICAL REVIEW B*, 80(15):155418, OCT 2009.
- [117] F. D. Murnaghan. The Compressibility of Media under Extreme Pressures. *Proceedings of the National Academy of Sciences of the United States of America*, 30(9):244–247, 1944.
- [118] S.S. Batsanov. *Effects of explosions on materials: modification and synthesis under high-pressure shock compression*. High pressure shock compression of condensed matter. Springer-Verlag, 1994.
- [119] BI Yakobson, CJ Brabec, and J Bernholc. Nanomechanics of carbon tubes: Instabilities beyond linear response. *PHYSICAL REVIEW LETTERS*, 76(14):2511–2514, APR 1 1996.
- [120] CD Reddy, S Rajendran, and KM Liew. Equilibrium configuration and continuum elastic properties of finite sized graphene. *NANOTECHNOLOGY*, 17(3):864–870, FEB 14 2006.
- [121] Changgu Lee, Xiaoding Wei, Jeffrey W. Kysar, and James Hone. Measurement of the elastic properties and intrinsic strength of monolayer graphene. *SCIENCE*, 321(5887):385–388, JUL 18 2008.
- [122] Zhen Hua Ni, Ting Yu, Yun Hao Lu, Ying Ying Wang, Yuan Ping Feng, and Ze Xiang Shen. Uniaxial Strain on Graphene: Raman Spectroscopy Study and Band-Gap Opening. *ACS NANO*, 2(11):2301–2305, NOV 2008.

- [123] Vitor M. Pereira and A. H. Castro Neto. Strain Engineering of Graphene's Electronic Structure. *PHYSICAL REVIEW LETTERS*, 103(4):046801, JUL 24 2009.
- [124] F. Guinea, M. I. Katsnelson, and A. K. Geim. Energy gaps and a zero-field quantum Hall effect in graphene by strain engineering. *NATURE PHYSICS*, 6(1):30–33, JAN 2010.
- [125] Hongjun Xiang, Erjun Kan, Su-Huai Wei, Myung-Hwan Whangbo, and Jinlong Yang. “Narrow” Graphene Nanoribbons Made Easier by Partial Hydrogenation. *NANO LETTERS*, 9(12):4025–4030, DEC 2009.
- [126] Chuanhong Jin, Fang Lin, Kazu Suenaga, and Sumio Iijima. Fabrication of a Freestanding Boron Nitride Single Layer and Its Defect Assignments. *PHYSICAL REVIEW LETTERS*, 102(19):195505, MAY 15 2009.
- [127] M. Topsakal and S. Ciraci. Elastic and plastic deformation of graphene, silicene, and boron nitride honeycomb nanoribbons under uniaxial tension: A first-principles density-functional theory study. *PHYSICAL REVIEW B*, 81(2):024107, JAN 2010.
- [128] R. S. Mulliken. Electronic population analysis on lcao[single bond]molecular wave functions. ii. overlap populations, bond orders, and covalent bond energies. *The Journal of Chemical Physics*, 23(10):1841–1846, 1955.
- [129] It should be kept in mind that there are ambiguities in calculating charge transfer. In fact, different methods result in different values of charge transfer.
- [130] Tianshu Li and Giulia Galli. Electronic properties of mos2 nanoparticles. *The Journal of Physical Chemistry C*, 111(44):16192–16196, 2007.
- [131] KK KAM and BA PARKINSON. DETAILED PHOTOCURRENT SPECTROSCOPY OF THE SEMICONDUCTING GROUP-VI TRANSITION-METAL DICHALCOGENIDES. *JOURNAL OF PHYSICAL CHEMISTRY*, 86(4):463–467, 1982.

- [132] F. Fuchs, J. Furthmüller, F. Bechstedt, M. Shishkin, and G. Kresse. Quasi-particle band structure based on a generalized kohn-sham scheme. *Phys. Rev. B*, 76(11):115109, Sep 2007.
- [133] Jochen Heyd, Gustavo E. Scuseria, and Matthias Ernzerhof. Hybrid functionals based on a screened coulomb potential. *The Journal of Chemical Physics*, 118(18):8207–8215, 2003.
- [134] Andrea Splendiani, Liang Sun, Yuanbo Zhang, Tianshu Li, Jonghwan Kim, Chi-Yung Chim, Giulia Galli, and Feng Wang. Emerging photoluminescence in monolayer mos₂. *Nano Letters*, 10(4):1271–1275, 2010. PMID: 20229981.
- [135] Young-Woo Son, Marvin L. Cohen, and Steven G. Louie. Energy gaps in graphene nanoribbons. *PHYSICAL REVIEW LETTERS*, 97(21):216803, Nov 2006.
- [136] C. Ataca and S. Ciraci. Functionalization of BN honeycomb structure by adsorption and substitution of foreign atoms. *PHYSICAL REVIEW B*, 82(16):165402, OCT 1 2010.
- [137] C. Ataca, E. Akturk, H. Sahin, and S. Ciraci. Adsorption of carbon adatoms to graphene and its nanoribbons. *JOURNAL OF APPLIED PHYSICS*, 109(1):013704, 2011.
- [138] E. Akturk, C. Ataca, and S. Ciraci. Effects of silicon and germanium adsorbed on graphene. *APPLIED PHYSICS LETTERS*, 96(12):123112, MAR 22 2010.
- [139] E. Durgun, N. Akman, C. Ataca, and S. Ciraci. Atomic and electronic structures of doped silicon nanowires: A first-principles study. *PHYSICAL REVIEW B*, 76(24):245323, DEC 2007.
- [140] KS Novoselov, AK Geim, SV Morozov, D Jiang, Y Zhang, SV Dubonos, IV Grigorieva, and AA Firsov. Electric field effect in atomically thin carbon films. *SCIENCE*, 306(5696):666–669, OCT 22 2004.

- [141] H. Sahin, S. Cahangirov, M. Topsakal, E. Bekaroglu, E. Akturk, R. T. Senger, and S. Ciraci. Monolayer honeycomb structures of group-IV elements and III-V binary compounds: First-principles calculations. *PHYSICAL REVIEW B*, 80(15):155453, OCT 2009.
- [142] C. Ataca and S. Ciraci. Perpendicular growth of carbon chains on graphene from first-principles. *Phys. Rev. B*, 83:235417, Jun 2011.
- [143] P. Esquinazi, D. Spemann, R. Höhne, A. Setzer, K.-H. Han, and T. Butz. Induced magnetic ordering by proton irradiation in graphite. *PHYSICAL REVIEW LETTERS*, 91(22):227201, Nov 2003.
- [144] A Hashimoto, K Suenaga, A Gloter, K Urita, and S Iijima. Direct evidence for atomic defects in graphene layers. *NATURE*, 430(7002):870–873, AUG 19 2004.
- [145] Oleg V. Yazyev and Lothar Helm. Defect-induced magnetism in graphene. *PHYSICAL REVIEW B*, 75(12):125408, Mar 2007.
- [146] M. A. H. Vozmediano, M. P. López-Sancho, T. Stauber, and F. Guinea. Local defects and ferromagnetism in graphene layers. *PHYSICAL REVIEW B*, 72(15):155121, Oct 2005.
- [147] L. Brey, H. A. Fertig, and S. Das Sarma. Diluted graphene antiferromagnet. *PHYSICAL REVIEW LETTERS*, 99(11):116802, Sep 2007.
- [148] J. J. Palacios, J. Fernández-Rossier, and L. Brey. Vacancy-induced magnetism in graphene and graphene ribbons. *PHYSICAL REVIEW B*, 77(19):195428, May 2008.
- [149] M. Topsakal, E. Aktürk, H. Sevinçli, and S. Ciraci. First-principles approach to monitoring the band gap and magnetic state of a graphene nanoribbon via its vacancies. *PHYSICAL REVIEW B*, 78(23):235435, Dec 2008.
- [150] H. Sahin, C. Ataca, and S. Ciraci. Magnetization of graphene by dehydrogenation. *APPLIED PHYSICS LETTERS*, 95(22):222510, NOV 30 2009.

- [151] H. Sahin, C. Ataca, and S. Ciraci. Electronic and magnetic properties of graphane nanoribbons. *PHYSICAL REVIEW B*, 81(20):205417, MAY 15 2010.
- [152] EH LIEB. 2 THEOREMS ON THE HUBBARD-MODEL. *PHYSICAL REVIEW LETTERS*, 62(10):1201–1204, MAR 6 1989.
- [153] Jingwei Bai, Xing Zhong, Shan Jiang, Yu Huang, and Xiangfeng Duan. Graphene nanomesh. *NATURE NANOTECHNOLOGY*, 5(3):190–194, MAR 2010.
- [154] Jayeeta Lahiri, You Lin, Pinar Bozkurt, Ivan I. Oleynik, and Matthias Batzill. An extended defect in graphene as a metallic wire. *NATURE NANOTECHNOLOGY*, 5(5):326–329, MAY 2010.
- [155] Richard Balog, Bjarke Jorgensen, Louis Nilsson, Mie Andersen, Emile Rienks, Marco Bianchi, Mattia Fanetti, Erik Laegsgaard, Alessandro Baraldi, Silvano Lizzit, Zeljko Sljivancanin, Flemming Besenbacher, Bjork Hammer, Thomas G. Pedersen, Philip Hofmann, and Liv Hornekaer. Bandgap opening in graphene induced by patterned hydrogen adsorption. *NATURE MATERIALS*, 9(4):315–319, APR 2010.
- [156] S. Cahangirov, M. Topsakal, E. Akturk, H. Sahin, and S. Ciraci. Two- and One-Dimensional Honeycomb Structures of Silicon and Germanium. *PHYSICAL REVIEW LETTERS*, 102(23):236804, JUN 12 2009.
- [157] H. Sahin, S. Cahangirov, M. Topsakal, E. Bekaroglu, E. Akturk, R. T. Senger, and S. Ciraci. Monolayer honeycomb structures of group-IV elements and III-V binary compounds: First-principles calculations. *PHYSICAL REVIEW B*, 80(15):155453, OCT 2009.
- [158] KS Novoselov, D Jiang, F Schedin, TJ Booth, VV Khotkevich, SV Morozov, and AK Geim. Two-dimensional atomic crystals. *PROCEEDINGS OF THE NATIONAL ACADEMY OF SCIENCES OF THE UNITED STATES OF AMERICA*, 102(30):10451–10453, JUL 26 2005.

- [159] K Takada, H Sakurai, E Takayama-Muromachi, F Izumi, RA Dilanian, and T Sasaki. Superconductivity in two-dimensional CoO₂ layers. *NATURE*, 422(6927):53–55, MAR 6 2003.
- [160] T Shishidou, AJ Freeman, and R Asahi. Effect of GGA on the half-metallicity of the itinerant ferromagnet CoS₂. *PHYSICAL REVIEW B*, 64(18):180401, NOV 1 2001.
- [161] C A Reed and S K Cheung. On the bonding of feo₂ in hemoglobin and related dioxygen complexes. *Proceedings of the National Academy of Sciences*, 74(5):1780–1784, 1977.
- [162] James Puthussery, Sean Seefeld, Nicholas Berry, Markelle Gibbs, and Matt Law. Colloidal Iron Pyrite (FeS(2)) Nanocrystal Inks for Thin-Film Photovoltaics. *JOURNAL OF THE AMERICAN CHEMICAL SOCIETY*, 133(4):716–719, FEB 2 2011.
- [163] NV Podberezskaya, SA Magarill, NV Pervukhina, and SV Borisov. Crystal chemistry of dichalcogenides MX₂. *JOURNAL OF STRUCTURAL CHEMISTRY*, 42(4):654–681, JUL-AUG 2001.
- [164] HY Hwang and SW Cheong. Enhanced intergrain tunneling magnetoresistance in half-metallic CrO₂ films. *SCIENCE*, 278(5343):1607–1609, NOV 28 1997.
- [165] H. Sims, S. J. Oset, W. H. Butler, James M. MacLaren, and Martijn Marsman. Determining the anisotropic exchange coupling of CrO(2) via first-principles density functional theory calculations. *PHYSICAL REVIEW B*, 81(22):224436, JUN 29 2010.
- [166] Manjit Pathak, Hunter Sims, Krishna B. Chetry, Dipanjan Mazumdar, Patrick R. LeClair, Gary J. Mankey, William H. Butler, and Arunava Gupta. Robust room-temperature magnetism of (110) CrO(2) thin films. *PHYSICAL REVIEW B*, 80(21):212405, DEC 2009.
- [167] Tomas Lofwander, Roland Grein, and Matthias Eschrig. Is CrO(2) Fully Spin Polarized? Analysis of Andreev Spectra and Excess Current. *PHYSICAL REVIEW LETTERS*, 105(20):207001, NOV 10 2010.

- [168] YJ Jin and JI Lee. Surface half-metallicity and magnetism of CoS₂(001): A first-principles study. *PHYSICAL REVIEW B*, 73(6):064405, FEB 2006.
- [169] V. N. Antonov, O. V. Andryushchenko, A. P. Shpak, A. N. Yaresko, and O. Jepsen. Electronic structure, optical spectra, and x-ray magnetic circular dichroism in CoS(2). *PHYSICAL REVIEW B*, 78(9):094409, SEP 2008.
- [170] Swarup Saha, Molly De Raychaudhury, and T. Saha-Dasgupta. Ab initio study of optical properties and magneto-optical Kerr effect in the pyrite compound CoS(2). *PHYSICAL REVIEW B*, 77(15):155428, APR 2008.
- [171] M. Otero-Leal, F. Rivadulla, M. Garcia-Hernandez, A. Pineiro, V. Pardo, D. Baldomir, and J. Rivas. Effect of spin fluctuations on the thermodynamic and transport properties of the itinerant ferromagnet CoS(2). *PHYSICAL REVIEW B*, 78(18):180415, NOV 2008.
- [172] XF Qian, XM Zhang, C Wang, Y Xie, and YT Qian. The preparation and phase transformation of nanocrystalline cobalt sulfides via a toluene thermal process. *INORGANIC CHEMISTRY*, 38(11):2621–2623, MAY 31 1999.
- [173] M. Y. C. Teo, S. A. Kulinich, O. A. Plaksin, and A. L. Zhu. Photoinduced Structural Conversions of Transition Metal Chalcogenide Materials. *JOURNAL OF PHYSICAL CHEMISTRY A*, 114(12):4173–4180, APR 1 2010.
- [174] M. M. Qazilbash, M. Brehm, Byung-Gyu Chae, P. C. Ho, G. O. Andreev, Bong-Jun Kim, Sun Jin Yun, A. V. Balatsky, M. B. Maple, F. Keilmann, Hyun-Tak Kim, and D. N. Basov. Mott transition in VO₂ revealed by infrared spectroscopy and nano-imaging. *SCIENCE*, 318(5857):1750–1753, DEC 14 2007.
- [175] M Takahashi, K Tsukigi, E Dorjpalam, Y Tokuda, and T Yoko. Effective photogeneration in TiO₂/VO₂/TiO₂ multilayer film electrodes prepared by a sputtering method. *JOURNAL OF PHYSICAL CHEMISTRY B*, 107(48):13455–13458, DEC 4 2003.

- [176] Zongtao Zhang, Yanfeng Gao, Litao Kang, Jing Du, and Hongjie Luo. Effects of a TiO(2) Buffer Layer on Solution-Deposited VO(2) Films: Enhanced Oxidization Durability. *JOURNAL OF PHYSICAL CHEMISTRY C*, 114(50):22214–22220, DEC 23 2010.
- [177] Zongtao Zhang, Yanfeng Gao, Zhang Chen, Jing Du, Chuanxiang Cao, Litao Kang, and Hongjie Luo. Thermo-chromic VO(2) Thin Films: Solution-Based Processing, Improved Optical Properties, and Lowered Phase Transformation Temperature. *LANGMUIR*, 26(13):10738–10744, JUL 6 2010.
- [178] Litao Kang, Yanfeng Gao, Hongjie Luo, Zhang Chen, Jin Du, and Zongtao Zhang. Nanoporous Thermo-chromic VO(2) Films with Low Optical Constants, Enhanced Luminous Transmittance and Thermo-chromic Properties. *ACS APPLIED MATERIALS & INTERFACES*, 3(2):135–138, FEB 2011.
- [179] Ngoc T. Nguyen, Brandon Howe, Juliana R. Hash, Nicholas Liebrecht, Paul Zschack, and David C. Johnson. Synthesis of a family of $\{[(VSe_2)_n](1.06)(TaSe_2)_m\}_z$ compounds. *CHEMISTRY OF MATERIALS*, 19(8):1923–1930, APR 17 2007.
- [180] GV Kamarchuk, AV Khotkevich, VM Bagatsky, VG Ivanov, P Molinie, A Leblanc, and E Faulques. Direct determination of Debye temperature and electron-phonon interaction in 1T-VSe₂. *PHYSICAL REVIEW B*, 63(7):073107, FEB 15 2001.
- [181] Dominic R. Alfonso. Computational Investigation of FeS(2) Surfaces and Prediction of Effects of Sulfur Environment on Stabilities. *JOURNAL OF PHYSICAL CHEMISTRY C*, 114(19):8971–8980, MAY 20 2010.
- [182] M Blanchard, M Alfredsson, J Brodholt, GD Price, K Wright, and CRA Catlow. Electronic structure study of the high-pressure vibrational spectrum of FeS(2) pyrite. *JOURNAL OF PHYSICAL CHEMISTRY B*, 109(46):22067–22073, NOV 24 2005.
- [183] V Eyert, KH Hock, S Fiechter, and H Tributsch. Electronic structure of FeS₂: The crucial role of electron-lattice interaction. *PHYSICAL REVIEW B*, 57(11):6350–6359, MAR 15 1998.

- [184] BC Bostick, S Fendorf, BT Bowie, and PR Griffiths. Influence of cadmium sorption on FeS₂ oxidation. *ENVIRONMENTAL SCIENCE & TECHNOLOGY*, 34(8):1494–1499, APR 15 2000.
- [185] C. Bruggeman and N. Maes. Uptake of Uranium(VI) by Pyrite under Boom Clay Conditions: Influence of Dissolved Organic Carbon. *ENVIRONMENTAL SCIENCE & TECHNOLOGY*, 44(11):4210–4216, JUN 1 2010.
- [186] P Gao, Y Xie, LN Ye, Y Chen, and QX Guo. From 2D nanoflats to 2D nanowire networks: A novel hyposulfite self-decomposition route to semiconductor FeS₂ nanowires. *CRYSTAL GROWTH & DESIGN*, 6(2):583–587, FEB 2006.
- [187] A. S. Barnard and S. P. Russo. Shape and thermodynamic stability of pyrite FeS₂ nanocrystals and nanorods. *JOURNAL OF PHYSICAL CHEMISTRY C*, 111(31):11742–11746, AUG 9 2007.
- [188] Yan Hu, Zhi Zheng, Huimin Jia, Yiwen Tang, and Lizhi Zhang. Selective synthesis of FeS and FeS₂ nanosheet films on iron substrates as novel photocathodes for tandem dye-sensitized solar cells. *JOURNAL OF PHYSICAL CHEMISTRY C*, 112(33):13037–13042, AUG 21 2008.
- [189] Yi Ding, Yanli Wang, Jun Ni, Lin Shi, Siqi Shi, and Weihua Tang. First principles study of structural, vibrational and electronic properties of graphene-like MX₂ (M=Mo, Nb, W, Ta; X=S, Se, Te) monolayers. *PHYSICA B-CONDENSED MATTER*, 406(11):2254–2260, MAY 15 2011.
- [190] H Imai, Y Shimakawa, and Y Kubo. Large thermoelectric power factor in TiS₂ crystal with nearly stoichiometric composition. *PHYSICAL REVIEW B*, 64(24):241104, DEC 15 2001.
- [191] S. S. Jaswal. Lattice dynamics of TiSe₂. *Phys. Rev. B*, 20:5297–5300, Dec 1979.
- [192] V. N. Strocov, E. E. Krasovskii, W. Schattke, N. Barrett, H. Berger, D. Schrupp, and R. Claessen. Three-dimensional band structure of layered TiTe₂: Photoemission final-state effects. *PHYSICAL REVIEW B*, 74(19):195125, NOV 2006.

- [193] Y Oka, S Sato, T Yao, and N Yamamoto. Crystal structures and transition mechanism of VO₂(A). *JOURNAL OF SOLID STATE CHEMISTRY*, 141(2):594–598, DEC 1998.
- [194] M. Mulazzi, A. Chainani, N. Katayama, R. Eguchi, M. Matsunami, H. Ohashi, Y. Senba, M. Nohara, M. Uchida, H. Takagi, and S. Shin. Absence of nesting in the charge-density-wave system 1T-VS(2) as seen by photoelectron spectroscopy. *PHYSICAL REVIEW B*, 82(7):075130, AUG 18 2010.
- [195] J. van Landuyt, G. A. Wiegers, and S. Amelinckx. A new type of deformation modulated superstructure in 1t-vse2 and its relation with other superstructures in transition metal dichalcogenides. *physica status solidi (a)*, 46(2):479–492, 1978.
- [196] A M Woolley and G Wexler. Band structures and fermi surfaces for 1t-tas 2 , 1t-tase 2 and 1t-vse 2. *Journal of Physics C: Solid State Physics*, 10(14):2601, 1977.
- [197] A. A. Vinokurov, A. V. Tyurin, A. L. Emelina, K. S. Gavrichev, and V. P. Zlomanov. Thermodynamic properties of VTe(2). *INORGANIC MATERIALS*, 45(5):480–485, MAY 2009.
- [198] E KULATOV and II MAZIN. EXTENDED STONER FACTOR CALCULATIONS FOR THE HALF-METALLIC FERROMAGNETS NIMNSB AND CRO₂. *JOURNAL OF PHYSICS-CONDENSED MATTER*, 2(2):343–350, JAN 15 1990.
- [199] CM Fang, CF vanBruggen, RA deGroot, GA Wiegers, and C Haas. The electronic structure of the metastable layer compound 1T-CrSe₂. *JOURNAL OF PHYSICS-CONDENSED MATTER*, 9(46):10173–10184, NOV 17 1997.
- [200] S. Devaraj and N. Munichandraiah. Effect of crystallographic structure of MnO₂ on its electrochemical capacitance properties. *JOURNAL OF PHYSICAL CHEMISTRY C*, 112(11):4406–4417, MAR 20 2008.

- [201] R Tappero, I Baraille, and A Lichanot. Electronic structure of pyrite-type manganese disulphide (pMnS(2)): An ab initio study. *PHYSICAL REVIEW B*, 58(3):1236–1242, JUL 15 1998.
- [202] H VOGT, T CHATTOPADHYAY, and HJ STOLZ. COMPLETE 1ST-ORDER RAMAN-SPECTRA OF THE PYRITE STRUCTURE COMPOUNDS FES₂, MNS₂ AND SIP₂. *JOURNAL OF PHYSICS AND CHEMISTRY OF SOLIDS*, 44(9):869–873, 1983.
- [203] T CHATTOPADHYAY, HG VONSCHNERING, RFD STANSFIELD, and GJ MCINTYRE. X-RAY AND NEUTRON-DIFFRACTION STUDY OF THE CRYSTAL-STRUCTURE OF MNS₂. *ZEITSCHRIFT FUR KRISTALLOGRAPHIE*, 199(1-2):13–24, 1992.
- [204] J. M. Hastings, N. Elliott, and L. M. Corliss. Antiferromagnetic structures of mns₂, mnse₂, and mnte₂. *Phys. Rev.*, 115:13–17, Jul 1959.
- [205] Q Peng, YJ Dong, ZX Deng, HH Kou, S Gao, and YD Li. Selective synthesis and magnetic properties of alpha-MnSe and MnSe₂ uniform microcrystals. *JOURNAL OF PHYSICAL CHEMISTRY B*, 106(36):9261–9265, SEP 12 2002.
- [206] P Vulliet, JP Sanchez, D Braithwaite, M Amanowicz, and B Malaman. Pressure-induced metallization and collapse of the antiferromagnetic state of MnTe₂. *PHYSICAL REVIEW B*, 63(18):184403, MAY 1 2001.
- [207] B Ouertani, J Ouerfelli, M Saadoun, B Bessais, H Ezzaouia, and JC Bernede. Transformation of amorphous iron oxide thin films predeposited by spray pyrolysis into a single FeSe₂-phase by selenisation. *SOLAR ENERGY MATERIALS AND SOLAR CELLS*, 87(1-4, SI):501–511, MAY 2005. International Conference on Physics, Chemistry and Engineering of Solar Cells, Univ Extremadura, Sch Ind Engn, Badajoz, SPAIN, MAY 13-15, 2004.
- [208] A. Kjekshus, T. Rakke, and Andresen A. F. *Acta Chemica Scandinavica*, 28a:996–1000, 1974.

- [209] F. Pertlik. *Anz. Osterr. Akad. Wiss., Math.-Naturwiss. Kl.*, 123:123, 1986.
- [210] G. Brostigen and A. Kjekshus. *Acta Chemica Scandinavica*, 24:1925–1940, 1970.
- [211] L Seguin, G Amatucci, M Anne, Y Chabre, P Strobel, JM Tarascon, and G Vaughan. Structural study of NiO₂ and CoO₂ as end members of the lithiated compounds by in situ high resolution X-ray powder diffraction. *JOURNAL OF POWER SOURCES*, 81:604–606, SEP 1999. 9th International Meeting on Lithium Batteries, EDINBURGH, SCOTLAND, JUL 12-17, 1998.
- [212] XH Chen and R Fan. Low-temperature hydrothermal synthesis of transition metal dichalcogenides. *CHEMISTRY OF MATERIALS*, 13(3):802–805, MAR 2001.
- [213] CJ Carmalt, TD Manning, IP Parkin, ES Peters, and AL Hector. Formation of a new (1T) trigonal NbS(2) polytype via atmospheric pressure chemical vapour deposition. *JOURNAL OF MATERIALS CHEMISTRY*, 14(3):290–291, 2004.
- [214] I. Guillamon, H. Suderow, S. Vieira, L. Cario, P. Diener, and P. Rodiere. Superconducting Density of States and Vortex Cores of 2H-NbS(2). *PHYSICAL REVIEW LETTERS*, 101(16):166407, OCT 17 2008.
- [215] T Yokoya, T Kiss, A Chainani, S Shin, M Nohara, and H Takagi. Fermi surface sheet-dependent superconductivity in 2H-NbSe₂. *SCIENCE*, 294(5551):2518–2520, DEC 21 2001.
- [216] G Campagnoli, A Gustinetti, and A Stella. Thermorefectance of 4h-nbse 2. *Journal of Physics C: Solid State Physics*, 7(11):L223, 1974.
- [217] C Battaglia, H Cercellier, F Clerc, L Despont, MG Garnier, C Koitzsch, P Aebi, H Berger, L Forro, and C Ambrosch-Draxl. Fermi-surface-induced lattice distortion in NbTe₂. *PHYSICAL REVIEW B*, 72(19):195114, NOV 2005.

- [218] Judith Moosburger-Will, Joerg Kuendel, Matthias Klemm, Siegfried Horn, Philip Hofmann, Udo Schwingenschloegl, and Volker Eyert. Fermi surface of MoO(2) studied by angle-resolved photoemission spectroscopy, de Haas-van Alphen measurements, and electronic structure calculations. *PHYSICAL REVIEW B*, 79(11):115113, MAR 2009.
- [219] David O. Scanlon, Graeme W. Watson, D. J. Payne, G. R. Atkinson, R. G. Egdell, and D. S. L. Law. Theoretical and Experimental Study of the Electronic Structures of MoO(3) and MoO(2). *JOURNAL OF PHYSICAL CHEMISTRY C*, 114(10):4636–4645, MAR 18 2010.
- [220] Guodong Du, Zaiping Guo, Shiquan Wang, Rong Zeng, Zhixin Chen, and Huakun Liu. Superior stability and high capacity of restacked molybdenum disulfide as anode material for lithium ion batteries. *CHEMICAL COMMUNICATIONS*, 46(7):1106–1108, 2010.
- [221] KE Dungey, MD Curtis, and JE Penner-Hahn. Structural characterization and thermal stability of MoS₂ intercalation compounds. *CHEMISTRY OF MATERIALS*, 10(8):2152–2161, AUG 1998.
- [222] J Morales, J Santos, and JL Tirado. Electrochemical studies of lithium and sodium intercalation in MoSe₂. *SOLID STATE IONICS*, 83(1-2):57–64, JAN 1996.
- [223] Laird C. Towle, Verne Oberbeck, Bruce E. Brown, and Ralph E. Stajdohar. Molybdenum diselenide: Rhombohedral high pressure-high temperature polymorph. *Science*, 154(3751):895–896, 1966.
- [224] FH Jones, RG Egdell, A Brown, and FR Wondre. Surface structure and spectroscopy of WO₂(012). *SURFACE SCIENCE*, 374(1-3):80–94, MAR 10 1997.
- [225] J Heising and MG Kanatzidis. Structure of restacked MoS₂ and WS₂ elucidated by electron crystallography. *JOURNAL OF THE AMERICAN CHEMICAL SOCIETY*, 121(4):638–643, FEB 3 1999.

- [226] Y Feldman, GL Frey, M Homyonfer, V Lyakhovitskaya, L Margulis, H Cohen, G Hodes, JL Hutchison, and R Tenne. Bulk synthesis of inorganic fullerene-like MS(2) (M=Mo, W) from the respective trioxides and the reaction mechanism. *JOURNAL OF THE AMERICAN CHEMICAL SOCIETY*, 118(23):5362–5367, JUN 12 1996.
- [227] T Straub, K Fauth, T Finteis, M Hengsberger, R Claessen, P Steiner, S Hufner, and P Blaha. Valence-band maximum in the layered semiconductor WSe₂: Application of constant-energy contour mapping by photoemission. *PHYSICAL REVIEW B*, 53(24):16152–16155, JUN 15 1996.
- [228] A MAR, S JOBIC, and JA IBERS. METAL METAL VS TELLURIUM TELLURIUM BONDING IN WTe₂ AND ITS TERNARY VARIANTS TAIRTE₄ AND NBIRTE₄. *JOURNAL OF THE AMERICAN CHEMICAL SOCIETY*, 114(23):8963–8971, NOV 4 1992.
- [229] Before one decides that a given compound is not stable one has to make every effort to vary specific parameters of the calculations. First of all if a given compound is magnetic, spin-polarized calculations have to be carried out. In some cases distant neighbors have to be taken into account. Calculations with relatively smaller superlattice may end up with instability. In other cases, not to end up with fake instability using the correct FTT mesh may be essential. Briefly, even though phonon calculations provide a rigorous tests, one has to be sure that appropriate parameters are used.
- [230] Paola De Padova, Claudio Quaresima, Bruno Olivieri, Paolo Perfetti, and Guy Le Lay. sp²-like hybridization of silicon valence orbitals in silicene nanoribbons. 98(8):081909, 2011.
- [231] Bernard Aufray, Abdelkader Kara, Sebastien Vizzini, Hamid Oughaddou, Christel Leandri, Benedicte Ealet, and Guy Le Lay. Graphene-like silicon nanoribbons on ag(110): A possible formation of silicene. 96(18):183102, 2010.
- [232] M. Houssa, G. Pourtois, V. V. Afanas'ev, and A. Stesmans. Can silicon behave like graphene? a first-principles study. 97(11):112106, 2010.

- [233] Boubekeur Lalami, Hamid Oughaddou, Hanna Enriquez, Abdelkader Kara, Sebastien Vizzini, Benedicte Ealet, and Bernard Aufray. Epitaxial growth of a silicene sheet. *97(22):223109*, 2010.
- [234] Paola De Padova, Claudio Quaresima, Carlo Ottaviani, Polina M. Sheverdyeva, Paolo Moras, Carlo Carbone, Dinesh Topwal, Bruno Olivieri, Abdelkader Kara, Hamid Oughaddou, Bernard Aufray, and Guy Le Lay. Evidence of graphene-like electronic signature in silicene nanoribbons. *96(26):261905*, 2010.
- [235] Cheng-Cheng Liu, Wanxiang Feng, and Yugui Yao. Quantum spin hall effect in silicene and two-dimensional germanium. *Phys. Rev. Lett.*, 107:076802, Aug 2011.
- [236] Paola De Padova, Claudio Quaresima, Bruno Olivieri, Paolo Perfetti, and Guy Le Lay. Strong resistance of silicene nanoribbons towards oxidation. *Journal of Physics D: Applied Physics*, 44(31):312001, 2011.
- [237] John P. Perdew, Kieron Burke, and Matthias Ernzerhof. Generalized gradient approximation made simple. *Phys. Rev. Lett.*, 77:3865–3868, Oct 1996.
- [238] T. Yildirim and S. Ciraci. Titanium-decorated carbon nanotubes as a potential high-capacity hydrogen storage medium. *Physical Review Letters*, 94:175501, May 2005.
- [239] To be published else where.
- [240] MV Bollinger, KW Jacobsen, and JK Norskov. Atomic and electronic structure of MoS(2) nanoparticles. *PHYSICAL REVIEW B*, 67(8), FEB 15 2003.
- [241] Xu Zong, Guopeng Wu, Hongjian Yan, Guijun Ma, Jingying Shi, Fuyu Wen, Lu Wang, and Can Li. Photocatalytic H(2) Evolution on MoS(2)/CdS Catalysts under Visible Light Irradiation. *JOURNAL OF PHYSICAL CHEMISTRY C*, 114(4):1963–1968, FEB 4 2010.
- [242] Jacob Bonde, Poul G. Moses, Thomas F. Jaramillo, Jens K. Norskov, and Ib Chorkendorff. Hydrogen evolution on nano-particulate transition metal sulfides. *FARADAY DISCUSSIONS*, 140:219–231, 2008. Conference on

- Electrocatalysis Theory and Experiment at the Interface, Univ Southampton, Southampton, ENGLAND, JUL 07-09, 2008.
- [243] Daniel Merki, Stephane Fierro, Heron Vrubel, and Xile Hu. Amorphous molybdenum sulfide films as catalysts for electrochemical hydrogen production in water. *CHEMICAL SCIENCE*, 2(7):1262–1267, 2011.
- [244] Poul Georg Moses, Berit Hinnemann, Henrik Topsoe, and Jens K. Nørskov. The hydrogenation and direct desulfurization reaction pathway in thiophene hydrodesulfurization over MoS(2) catalysts at realistic conditions: A density functional study. *JOURNAL OF CATALYSIS*, 248(2):188–203, JUN 10 2007.
- [245] Jeff Greeley, Thomas F. Jaramillo, Jacob Bonde, I. B. Chorkendorff, and Jens K. Nørskov. Computational high-throughput screening of electrocatalytic materials for hydrogen evolution. *NATURE MATERIALS*, 5(11):909–913, NOV 2006.
- [246] JK Nørskov, T Bligaard, A Logadottir, JR Kitchin, JG Chen, S Pandalov, and JK Nørskov. Trends in the exchange current for hydrogen evolution. *JOURNAL OF THE ELECTROCHEMICAL SOCIETY*, 152(3):J23–J26, 2005.
- [247] J. K. Nørskov, T. Bligaard, J. Rossmeisl, and C. H. Christensen. Towards the computational design of solid catalysts. *NATURE CHEMISTRY*, 1(1):37–46, APR 2009.
- [248] Yanguang Li, Hailiang Wang, Liming Xie, Yongye Liang, Guosong Hong, and Hongjie Dai. MoS(2) Nanoparticles Grown on Graphene: An Advanced Catalyst for the Hydrogen Evolution Reaction. *JOURNAL OF THE AMERICAN CHEMICAL SOCIETY*, 133(19):7296–7299, MAY 18 2011.
- [249] K Maeda, K Teramura, DL Lu, T Takata, N Saito, Y Inoue, and K Domen. Photocatalyst releasing hydrogen from water - Enhancing catalytic performance holds promise for hydrogen production by water splitting in sunlight. *NATURE*, 440(7082):295, MAR 16 2006.

- [250] Akihiko Kudo, Hideki Kato, and Seira Nakagawa. Water splitting into H_2 and O_2 on new $\text{Sr}_2\text{M}_2\text{O}_7$ ($\text{M} = \text{Nb}$ and Ta) photocatalysts with layered perovskite structures: Factors affecting the photocatalytic activity. *The Journal of Physical Chemistry B*, 104(3):571–575, 2000.
- [251] Yasuyoshi Sasaki, Hiroaki Nemoto, Kenji Saito, and Akihiko Kudo. Solar water splitting using powdered photocatalysts driven by z-schematic interparticle electron transfer without an electron mediator. *The Journal of Physical Chemistry C*, 113(40):17536–17542, 2009.
- [252] Akihiko Iwase, Yun Hau Ng, Yoshimi Ishiguro, Akihiko Kudo, and Rose Amal. Reduced graphene oxide as a solid-state electron mediator in z-scheme photocatalytic water splitting under visible light. *Journal of the American Chemical Society*, 133(29):11054–11057, 2011.
- [253] Wei-Min Sun, Xiang-Song Chen, Xiao-Fu Lü, and Fan Wang. Gauge-invariant hydrogen-atom hamiltonian. *Phys. Rev. A*, 82:012107, Jul 2010.
- [254] Robert Coontz and Brooks Hanson. Not so simple. *Science*, 305(5686):957, 2004.
- [255] Metal Dihydrogen and Bond Complexes-Structure, Theory and Reactivity, edited by G. J. Kubas (Kluwer Academics/Plenum, New York, 2001).
- [256] Yufeng Zhao, Yong-Hyun Kim, A. C. Dillon, M. J. Heben, and S. B. Zhang. Hydrogen storage in novel organometallic buckyballs. *Phys. Rev. Lett.*, 94:155504, Apr 2005.
- [257] A. Fasolino, J. H. Los, and M. I. Katsnelson. Intrinsic ripples in graphene. *NATURE MATERIALS*, 6(11):858–861, NOV 2007.
- [258] A. B. Phillips and B. S. Shivaram. High capacity hydrogen absorption in transition metal-ethylene complexes observed via nanogravimetry. *Phys. Rev. Lett.*, 100:105505, Mar 2008.
- [259] S Dag and S Ciraci. Atomic scale study of superlow friction between hydrogenated diamond surfaces. *PHYSICAL REVIEW B*, 70(24):241401, DEC 2004.

- [260] Mina Yoon, Shenyuan Yang, Christian Hicke, Enge Wang, David Geohegan, and Zhenyu Zhang. Calcium as the superior coating metal in functionalization of carbon fullerenes for high-capacity hydrogen storage. *Phys. Rev. Lett.*, 100:206806, May 2008.
- [261] H. Sevinçli, M. Topsakal, E. Durgun, and S. Ciraci. Electronic and magnetic properties of 3d transition-metal atom adsorbed graphene and graphene nanoribbons. *Phys. Rev. B*, 77:195434, May 2008.